AFRL-AFOSR-UK-TR-2010-0007

Studies of the Electrohydrodynamic Force Produced in a Dielectric Barrier Discharge for Flow Control

Jean-Pierre Boeuf
Universite Paul Sabatier
118 Route de Narbonne
Toulouse, France 31062

EOARD SPC 06-4004

February 2010

Final Report for 01 September 2006 to 01 September 2009

Air Force Research Laboratory
Air Force Office of Scientific Research
European Office of Aerospace Research and Development
Unit 4515 Box 14, APO AE 09421

REPORT DOCUMENTATION PAGE	Form Approved OMB No. 0704-0188

1. REPORT DATE ***(DD-MM-YYYY)*** 01-02-2010	**2. REPORT TYPE** Final Report	**3. DATES COVERED** *(From – To)* 01 September 2006 - 01 September 2009

4. TITLE AND SUBTITLE Studies of the Electrohydrodynamic Force Produced in a Dielectric Barrier Discharge for Flow Control	**5a. CONTRACT NUMBER** FA8655-06-C-4004 **5b. GRANT NUMBER** **5c. PROGRAM ELEMENT NUMBER**
6. AUTHOR(S) Professor Jean-Pierre Boeuf	**5d. PROJECT NUMBER** **5d. TASK NUMBER** **5e. WORK UNIT NUMBER**

7. PERFORMING ORGANIZATION NAME(S) AND ADDRESS(ES) Universite Paul Sabatier 118 Route de Narbonne Toulouse 31062 France	**8. PERFORMING ORGANIZATION REPORT NUMBER** SPC 06-4004
9. SPONSORING/MONITORING AGENCY NAME(S) AND ADDRESS(ES) EOARD Unit 4515 BOX 14 APO AE 09421	**10. SPONSOR/MONITOR'S ACRONYM(S)** **11. SPONSOR/MONITOR'S REPORT NUMBER(S)** **AFRL-AFOSR-UK-TR-2010-0007**

12. DISTRIBUTION/AVAILABILITY STATEMENT

Approved for public release; distribution is unlimited. (approval given by local Public Affairs Office)

13. SUPPLEMENTARY NOTES

14. ABSTRACT

The mechanisms of ion wind generation in surface dielectric barrier discharges (SDBDs) is identical to the one in corona discharges. The electrohydrodynamic force (EHD) generated in SDBDs for moderate increase rates of the applied voltage is, as in corona discharges, due to the development of a unipolar region above the dielectric surface, where ion space charge is dominant and ions transfer momentum to the neutral gas. For very fast rise (few ns) of the applied voltage, ion wind is no longer important and the action of the discharge on the flow is different. SDBDs are more interesting for applications than DC corona because high current breakdown and transition to the arc regime are prevented by the use of a dielectric layer. There is no evidence that SDBDs can generate larger ion wind than DC corona discharges. For a given power dissipated in the discharge, the EHD force decreases when the frequency increases. This trend is also valid for other voltage waveforms. The nanosecond discharge regime has been simulated and its possible aerodynamic effects have been studied by coupling the discharge model with Navier Stokes equations. The results confirm that the EHD force generated in the nanosecond regime is negligible and show that the fast heating of the gas in the vicinity of the exposed electrode can lead to a large temperature increase in a short time, giving rise to the development of micro shockwaves. These pressure waves may be responsible for the observed aerodynamic effects.

15. SUBJECT TERMS

EOARD, Transition, Boundary Layer, Separated Flows, Plasma Aerodynamics

16. SECURITY CLASSIFICATION OF:			**17. LIMITATION OF ABSTRACT**	**18, NUMBER OF PAGES**	**19a. NAME OF RESPONSIBLE PERSON**
a. REPORT UNCLAS	**b. ABSTRACT** UNCLAS	**c. THIS PAGE** UNCLAS	UL	52	Brad Thompson **19b. TELEPHONE NUMBER** *(Include area code)* +44 (0)1895 616163

Grant FA8655-06-C-4004

STUDIES OF THE ELECTROHYDRODYNAMIC FORCE PRODUCED IN A DIELECTRIC BARRIER DISCHARGE FOR FLOW CONTROL

J.P. Boeuf, T. Unfer, and L. Pitchford
ADPA, LAPLACE, Université Paul Sabatier, 31062 Toulouse, France

2nd report phase 3 – January 2010

ABSTRACT

This report is the last of our contract Grant FA8655-06-C-4004. The report is divided in three parts. The first part presents a parametric study of surface dielectric barrier discharges driven by nanosecond pulses. The second discusses the accuracy of the simulation by comparing two different numerical methods used in this work. The third is a summary of the results and conclusions drawn from the work performed in the frame of this contract.
Attached to this report are the papers related to this work and published during the course of the contract.

I. SURFACE DIELECTRIC BARRIER DISCHARGES (SDBD) DRIVEN BY NANOSECOND PULSES : A PARAMETRIC STUDY

The purpose of this study is to perform a parametric study of the gas dynamics induced by a nanosecond surface dielectric barrier discharge. The geometry is based on some recent experiments of Starikovskii and coworkers, [1] (see Fig. 1) and which were also used in our previous report and in Ref. [2]. Starikovskii et al. introduced a new type of surface dielectric barrier discharge using a nanosecond voltage pulse generator. The voltage pulse can be several 10s of kV with rise and decay times on the order or less than 10 ns. Under these conditions, the corona regime that is responsible for the ion wind in sinusoidal regimes is no longer present and the main discharge regime is a streamer regime. This was confirmed by the quasi-zero ion wind measuredin [1]. The authors showed that this kind of discharge was able to affect the aerodynamic properties of a flow along the surface in spite of the quasi-zero ion wind, and that a detached flow could be reattached when a nanosecond voltage pulse was applied between the electrodes at a repetition rate of a few kHz (for spanwise as well as streamwise configurations of the DBD actuators with respect to the flow direction). The computation domain is recalled in Fig. 1.

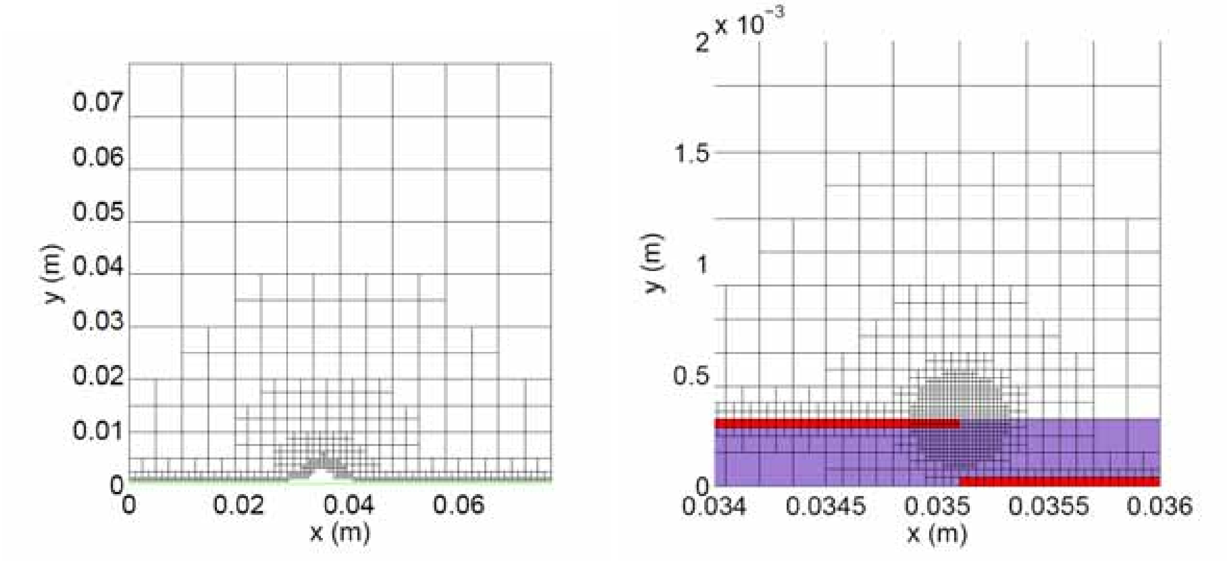

Figure 1 : Computational domain. The electrodes are embedded in a 300 µm wide PMMA layer (ε_r=5). The electrodes are 5 mm long and 37 µm wide.

Both the Navier-Stokes equations and plasma equations are solved on a few centimeters large domain using the new numerical technique called Asynchronous Adaptive Mesh Refinement [4], [5]. The sensitivity to different parameters such as maximum voltage, pulse duration, seed electron density, secondary emission are presented in the following pages. Some prospective results on the influence of an external airflow on the discharge are also given to point out tendencies.

I.1 SENSITIVITY TO THE MAXIMUM VOLTAGE OF THE NANOSECOND PULSES

The most natural question that arises when trying to optimize the effect on the neutral gas is certainly : does the effect increase with voltage ?

This has been investigated by performing simulations with the same voltage slope during the rise and fall phases of the pulse, i.e. 2000 V/ns in the rise phase and -933 V/ns, but with different values of the voltage maximum. The voltage values in the plateau phases are equal to 14, 21, 28, 35 and 42 kV respectively (see Fig. 2).

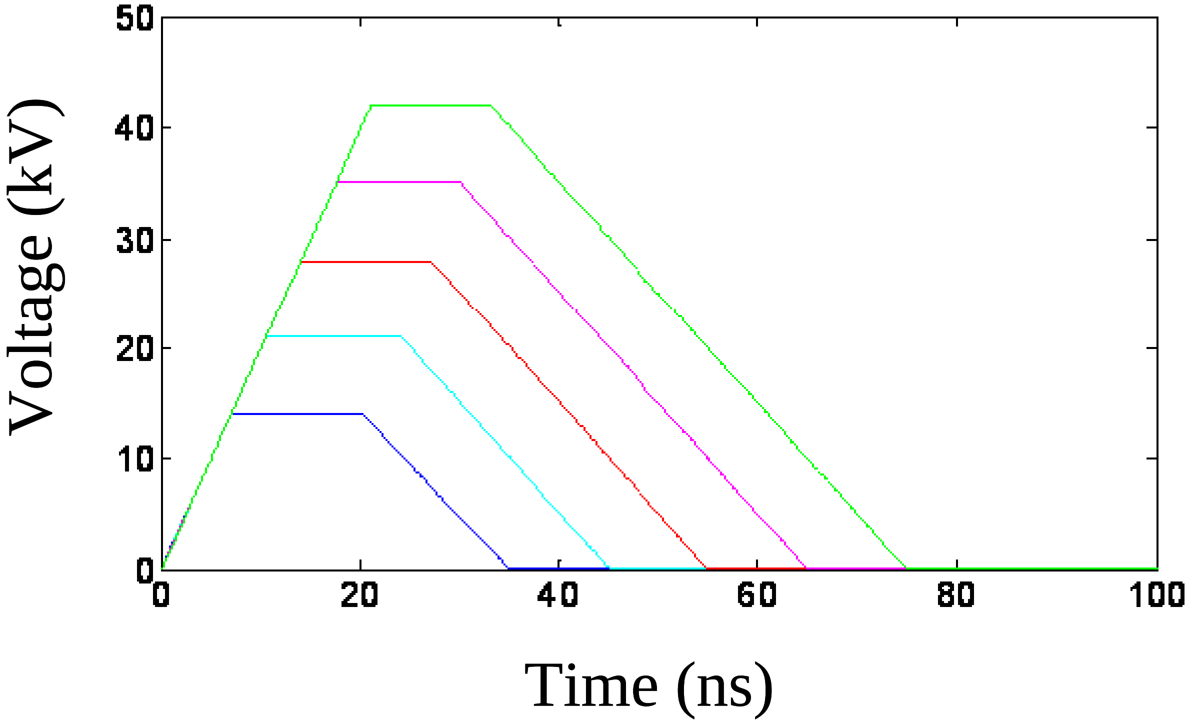

Figure 2 : Shape of the applied voltage pulses in the simulations, with maxima (plateau) at 14, 21, 28, 35 and 42 kV

The calculated discharge currents for the voltage pulses of Fig. 2 are shown in Fig. 3. We see that the current response of the discharge follows the same curve during the potential rise phase, as expected. For 28kV and higher the maximum value of the current saturates around 1800 A/m, due to the fact that the streamer head has reached the maximum extension of the lower electrode (5 mm). After that point there is still some heating as shown in Figs. 4a and 5 below. Nevertheless this late heating could be optimized by using a longer lower electrode. The same phenomenon occurs during the second (negative) pulse, for 28 kV and higher voltages, the maximum current value appears to be limited by the extension of the lower electrode. Figure 5 shows the total energy deposition in the neutral gas by the discharge. This deposition seems to vary quite linearly with the voltage amplitude. However the maximum temperature reached is saturating around 35 kV. This can be explained if one takes into account that :

- the maximum temperature is reached at the very tip of the upper electrode

- the maximum heating occurs during the negative current pulse, when the positive ions are collected by the electrode tip

- the negative current pulse occurs around 60 ns and the smallest mesh size is about 20 µm which correspond roughly to the distance covered by an acoustic wave during 60 ns. This means that some energy has already be dissipated by the shock wave.

The maximum temperature could be further increased with voltage higher than 35 kV however this is only possible if the potential variation rate dV/dt is larger.

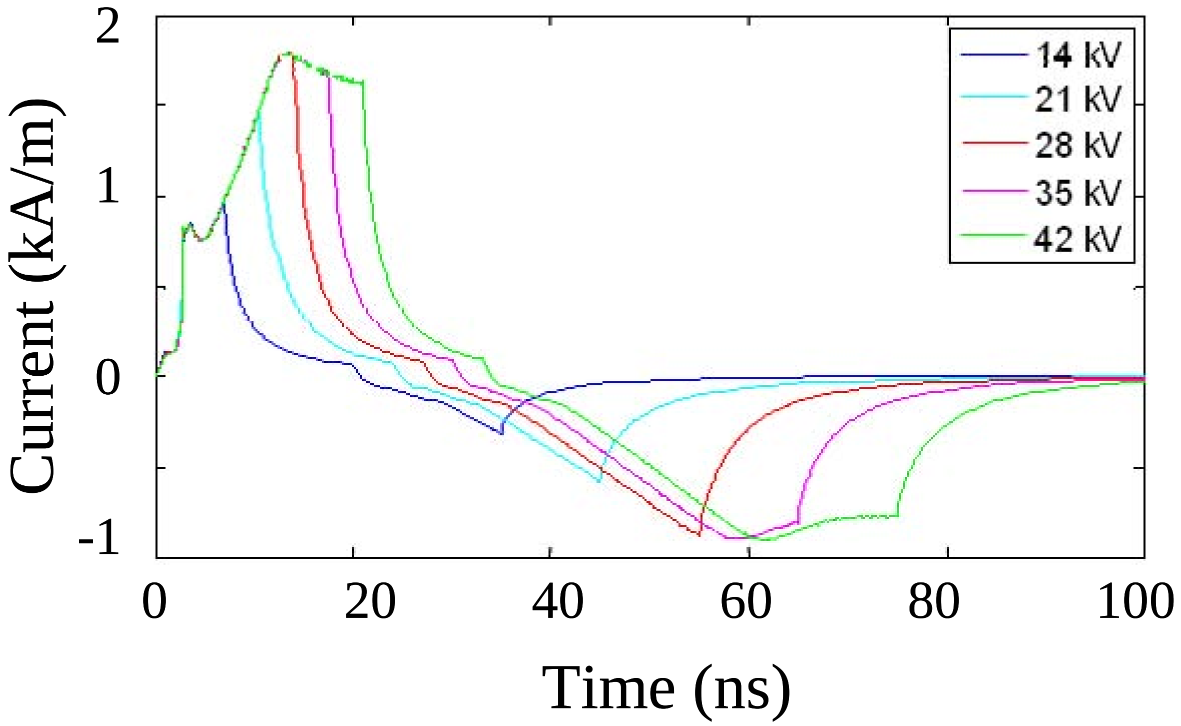

Figure 3: Calculated discharge currents for the voltage pulses of Fig. 2 (the maximum voltage is indicated on the figure).

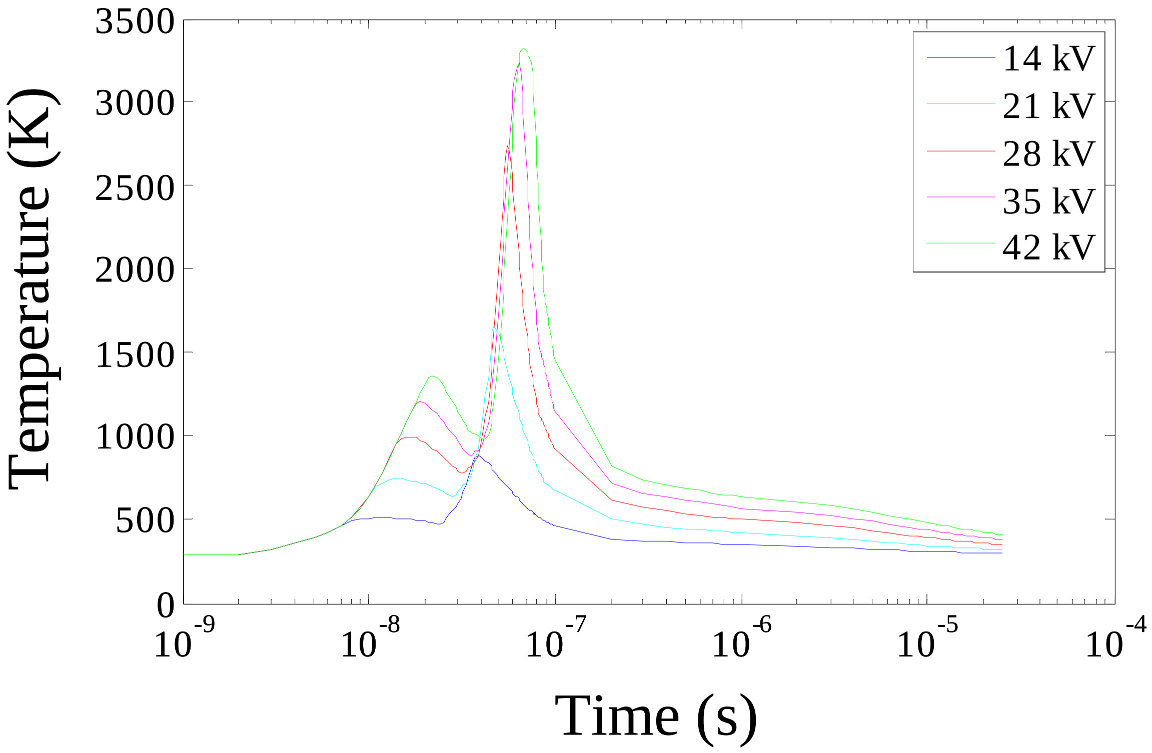

Figure 4a: Maximum air temperature calculated in the conditions of Figs. 2, 3. The maximum value is reached in a very small volume (and is much smaller when averaged over a finite volume element, e.g. 20 μm x 20 μm or more, see Fig. 4b)

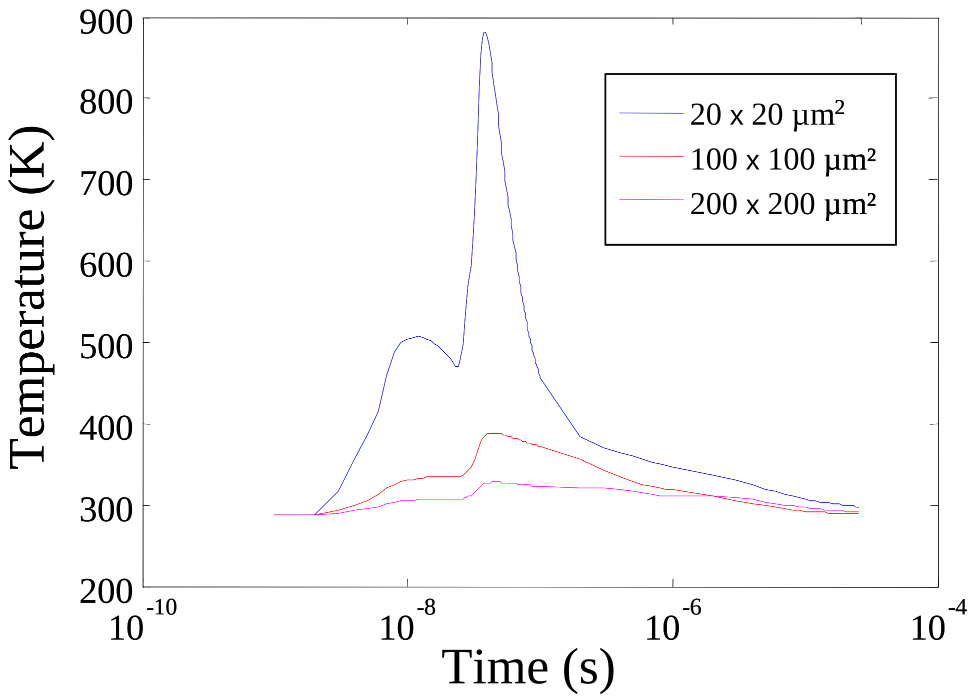

Figure 4b: Maximum air temperature in the reference case (14 kV) with different integration volumes

The temperature reached by the hottest cell of the mesh (about 20 µm²) as shown on Fig. 4a is almost 900 K for a few ns. However this data is difficult to obtain experimentally because it needs very high resolution measurements in space and time. The reason why the temperature is so hot in the calculation is because the maximum is located at the very tip of the electrode. When the temperature is averaged over a greater volume (100 or 200 µm² see Fig. 4b) the temperature increase is on the order of 100 K which is comparable to the measurements of Starikovskii and al.

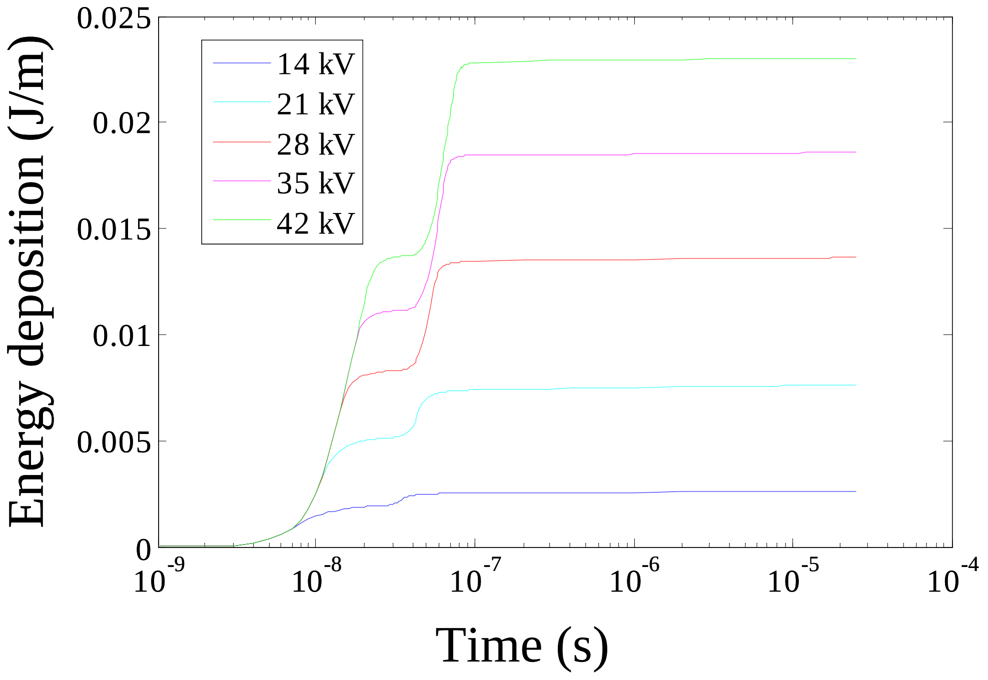

Figure 5: Total energy deposition in the neutral gas

The voltage amplitude seems to be a good design parameter to obtain some specific heating effect on the flow. The dV/dt is also an important parameter that needs to be studied.

I.2 SENSITIVITY TO THE DURATION OF THE NANOSECOND PULSES

In the reference case (14 kV in the previous section, see Fig. 3), the discharge current is not zero when it changes sign abruptly shortly after the voltage starts to decrease, after the plateau (t=20 ns). We looked at the effect of the duration of the voltage plateau on the energy transfer. Pulse durations from 35 to 55 ns were tested as shown in Fig. 6. Indeed it is possible to extract more current during the positive pulse (see Fig. 7) which leads to a higher heating of the gas (see Fig. 8). Because the positive pulse has transferred more charge to the surface for longer pulses, the following negative current pulse is a little stronger. This explain the higher temperature obtained (see Fig. 9). However if the pulse duration is too long the maximum temperature decreases because the acoustic wave has started to dissipate energy.

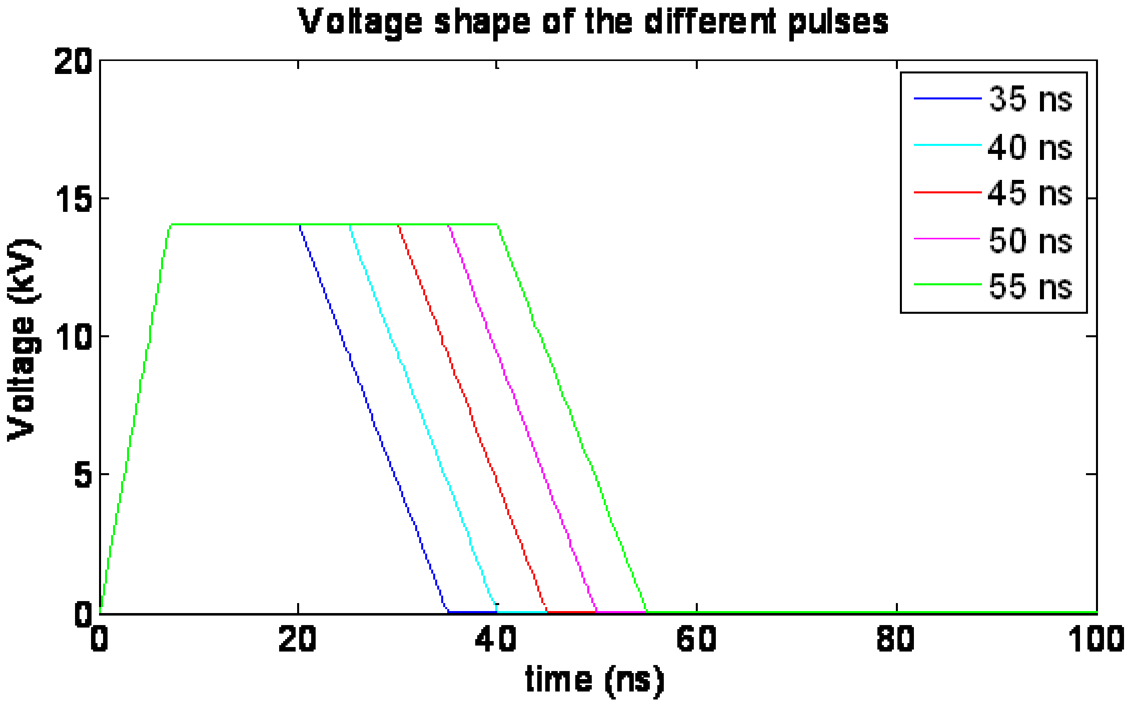

Figure 6: Shape of the applied pulses

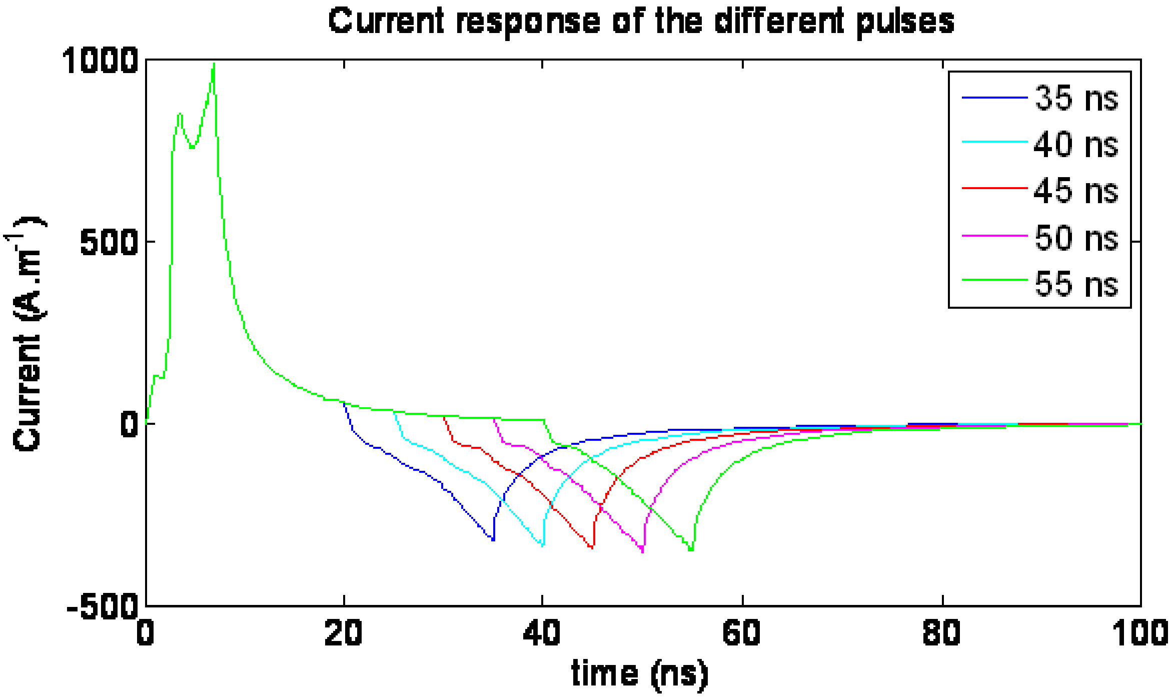

Figure 7: Current on the lower electrode for different voltage plateau durations (Fig. 6)

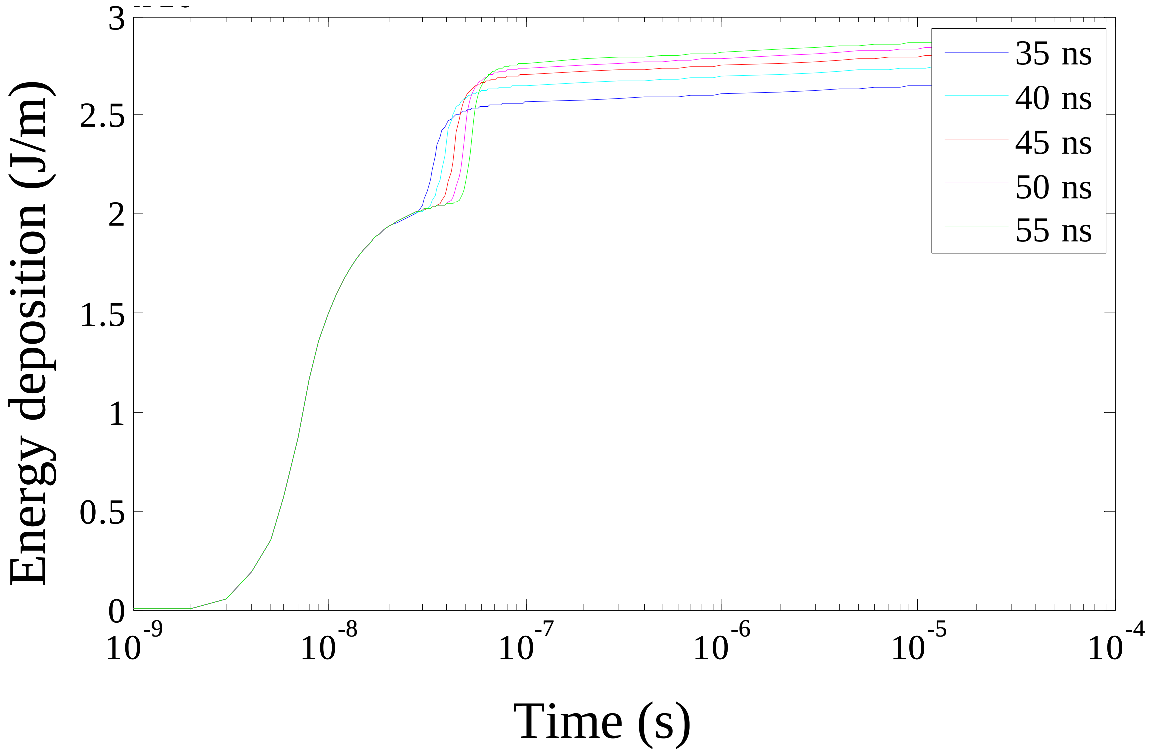

Figure 8: Total energy deposition in the neutral gas for different voltage plateau durations (Fig. 6)

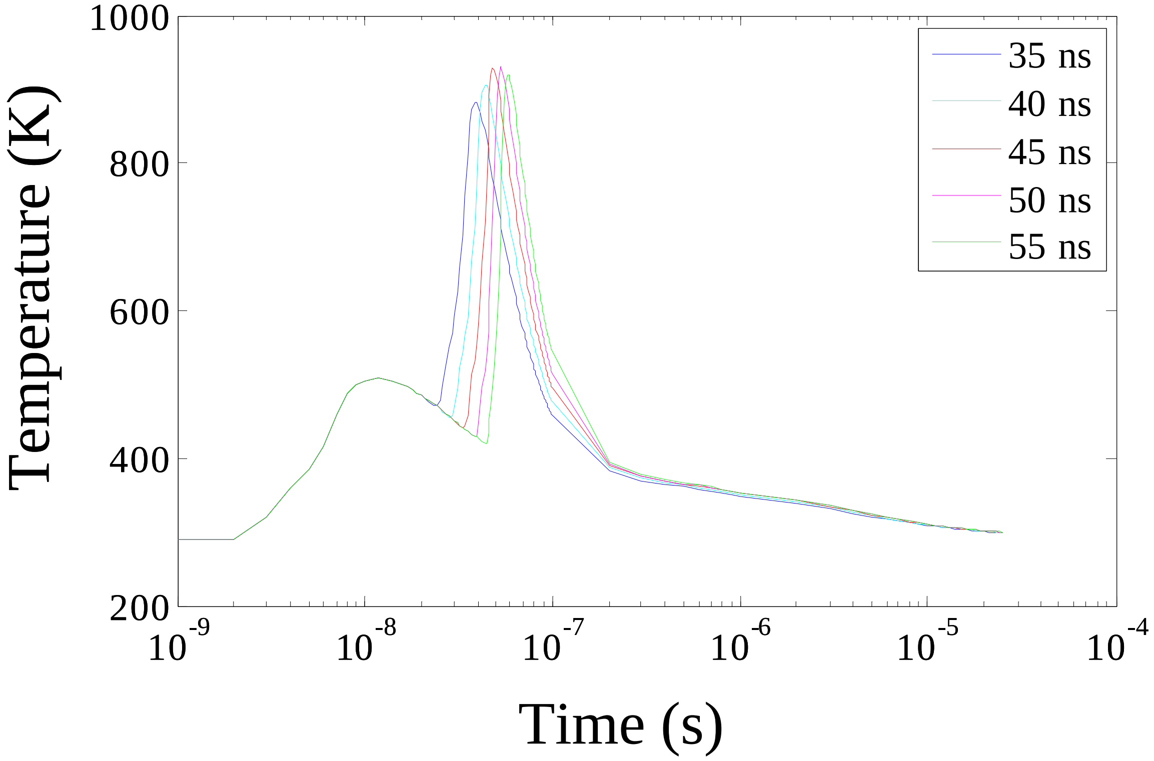

Figure 9: maximum air temperature reached for different voltage plateau durations (Fig. 6)

I.3 SENSITIVITY TO THE SEED ELECTRON DENSITY

Our plasma model describes the charged particles with fluid equations. The discharge is initiated by assuming a given, small and uniform density of electrons and ions in the simulation domain at t=0. The effect of this initial density is similar to photoionization since it provides the seeds electrons necessary to ensure the cathode streamer propagation if the contribution of secondary emission from the surface is not sufficient or not fast enough. We find that the calculations are not very sensitive to the seed electron density level. In any case the impact is limited to the first half of the positive current pulse (see Figs. 10a & b) and leads to no significant variation in the total energy deposition (see Fig. 11). We also performed calculations with a non uniform initial density of seed electrons (10^{10} m^{-3} in the near vicinity of the exposed electrode and zero everywhere else, see Fig. 10a). The current is not very different even in that case. We also looked at a possible effect of secondary electron emission (next section).

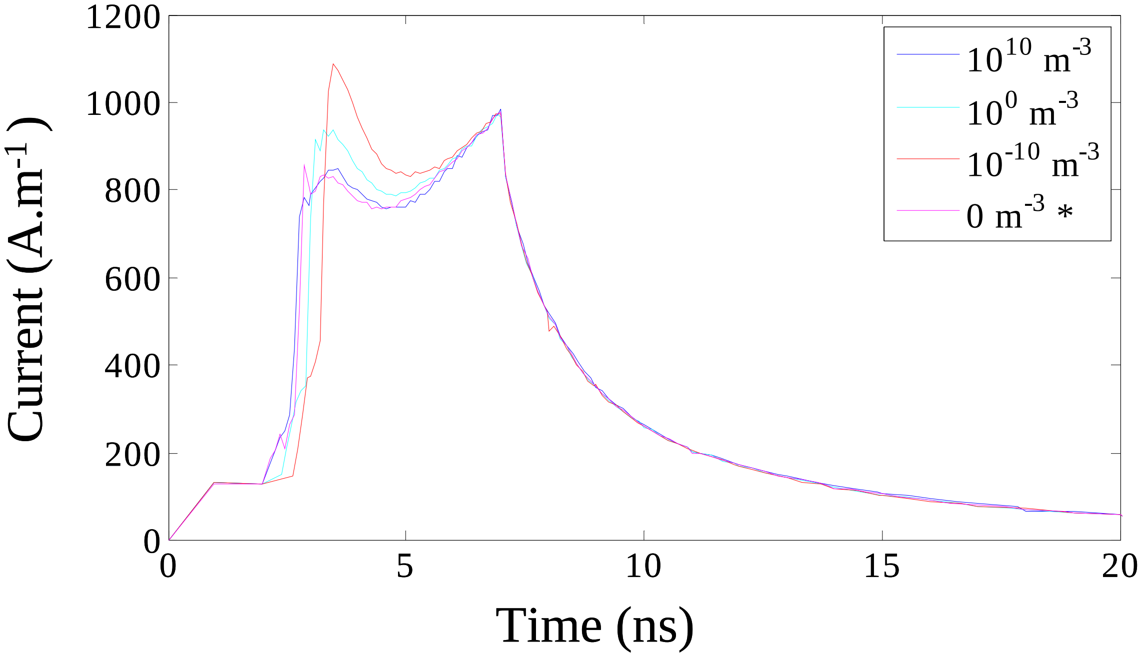

*: zero seed density means 10^{10} m^{-3} in the near vicinity of the exposed electrode and zero otherwise

Figure 10a: Current on the lower electrode for different seed electron density

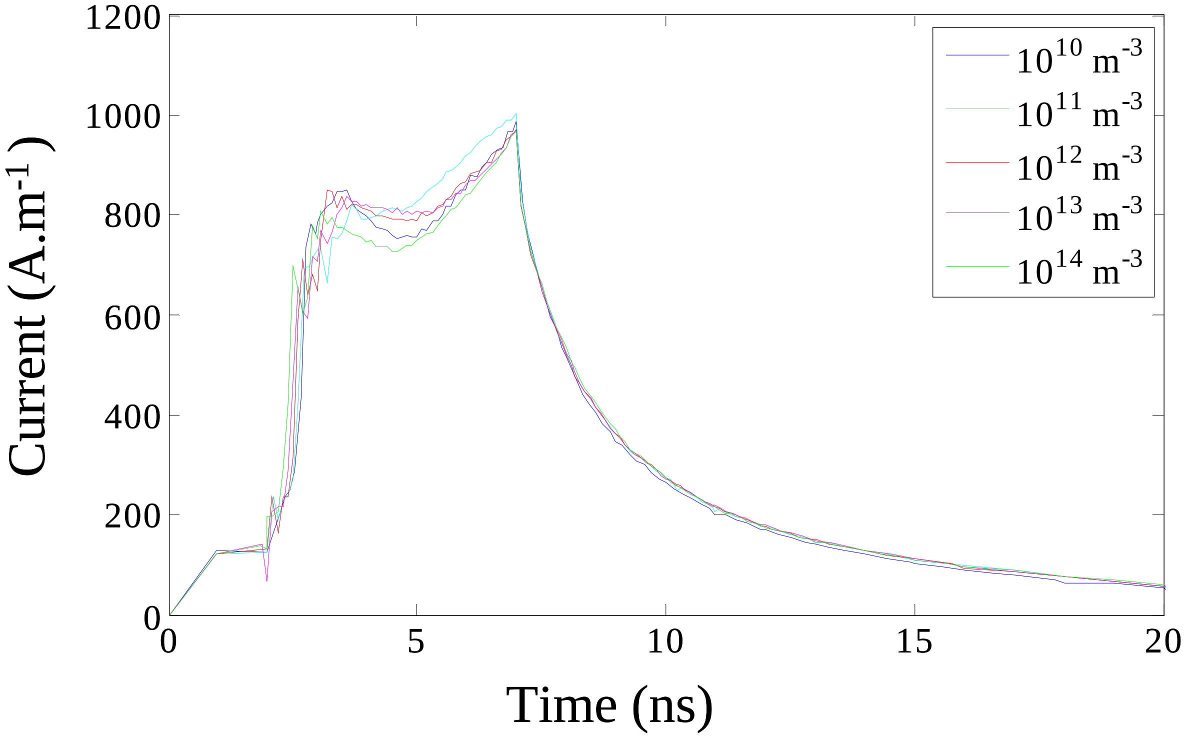

Figure 10b: Current on the lower electrode for different seed electron density

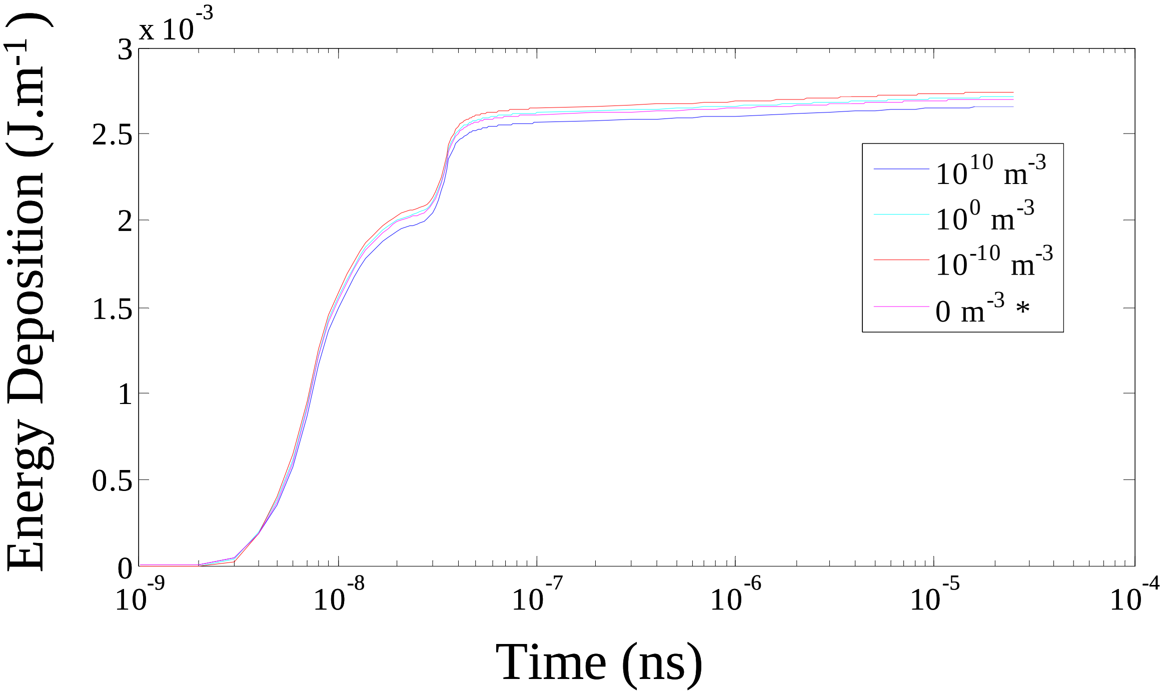

Figure 11: Total energy deposition in the neutral gas for different seed electron density

I.4 SENSITIVITY TO THE ELECTRON SECONDARY EMISSION

The secondary electron emission from the surface due to ion impact is another key parameter that could play a role in the propagation of the discharge. However as shown on Fig. 12 the discharge current and consequently the heating properties of the discharge are not altered by the secondary emission coefficient.

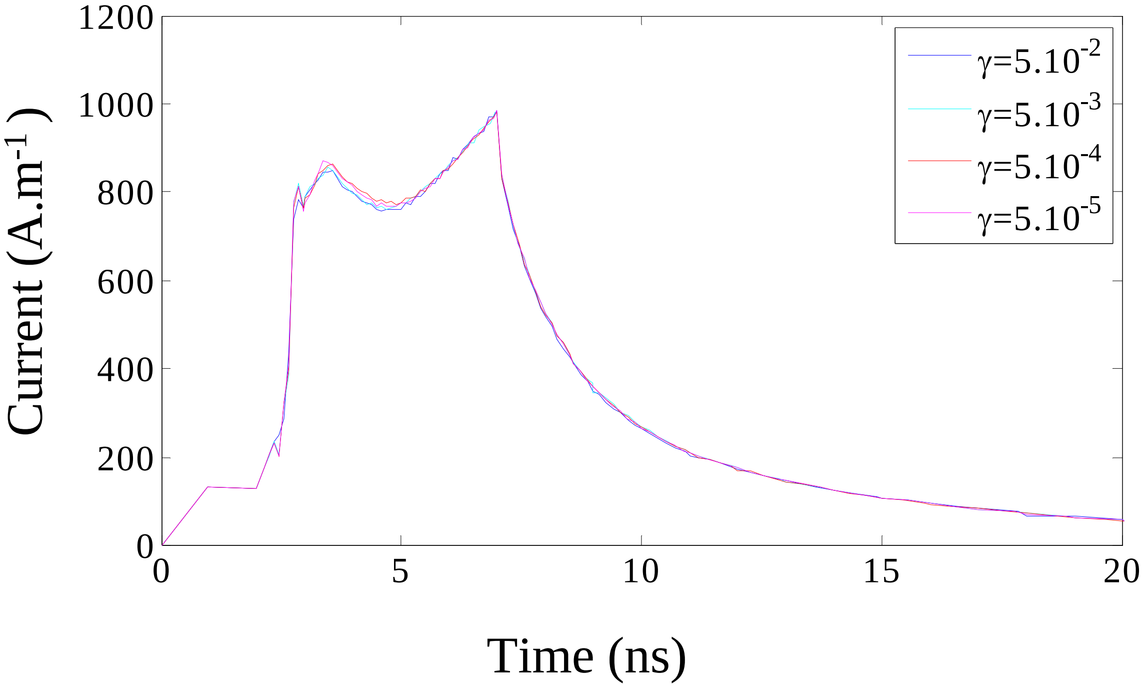

Figure 12: Current on the lower electrode for different values of the secondary electron emission coefficient on the dielectric barrier surface

The results above (only slight dependence of the results on the initial seed electron density or on the secondary electron emission) are very intriguing and pose the question of the possible effects of numerical diffusion (a cathode streamer should not propagate without seed electrons or when the secondary emission coefficient is zero). In these conditions of large overvoltage and fast rise time numerical diffusion is possible in spite of the use of a second order MUSCL scheme in the model and this point needs further investigations.

I.5 SENSITIVITY TO THE AIR FLOW VELOCITY

The purpose of this section is to give some qualitative preliminary ideas about how the discharge and its effects are affected by an external airflow. In order to achieve this, new boundary conditions of the characteristic type have been implemented for subsonic inflow and non reflective outflow for the Navier-Stokes equations. The accuracy of the external airflow computation is relatively crude because the cell number has to be limited in order to be able to compute the discharge in a reasonable time. Furthermore there is no turbulence model added to the Navier-Stokes equations, so we expect the results to be less precise as the velocity increases. However the aim of this parametric study is only to draw trends. Figure 13 shows the external airflow obtained for 50 m/s incoming velocity. Because the electrodes are located at 3.5 cm from the leading edge of the plate and because the discharge occurs very close to the surface, the plasma formation is not so much influenced by the airflow. Still there is some effect as shown on Fig. 14, an increase in the external airflow velocity leads to a lower discharge current and corresponding heating (see Fig. 15) and maximum temperature (see Fig. 16). Additional investigation are required, but this effect is believed to be higher if the electrodes are placed closer to the leading edge.

Figure 17 shows how the pressure wave generated near the electrodes interacts with the external airflow. Due to the position of the discharge deep into the boundary layer, the interaction is low at the first few microseconds, but once the wave has gained some altitude, it encounters the stronger flow and begins to be distorted.

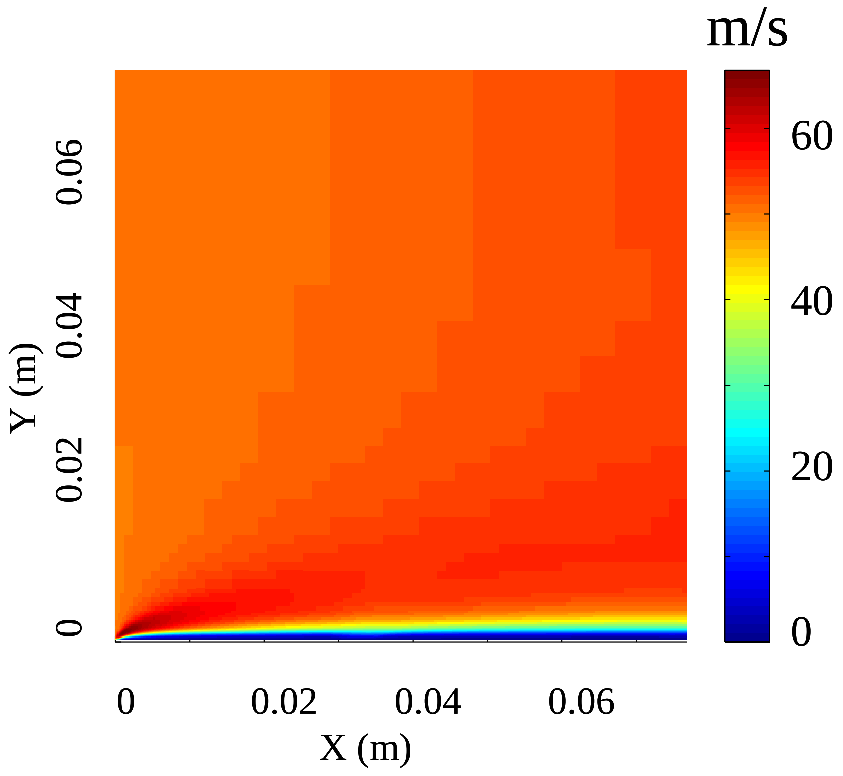

Figure 13:external airflow

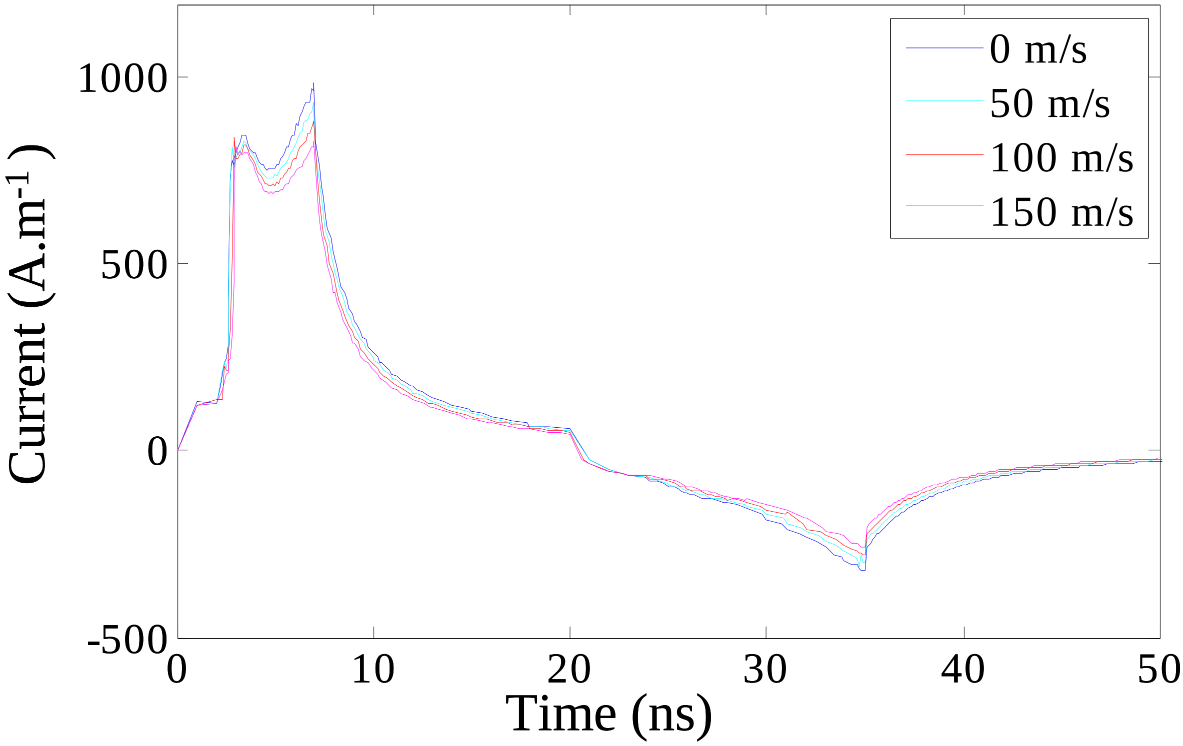

Figure 14: Current on the lower electrode vs time for different velocities of the external flow

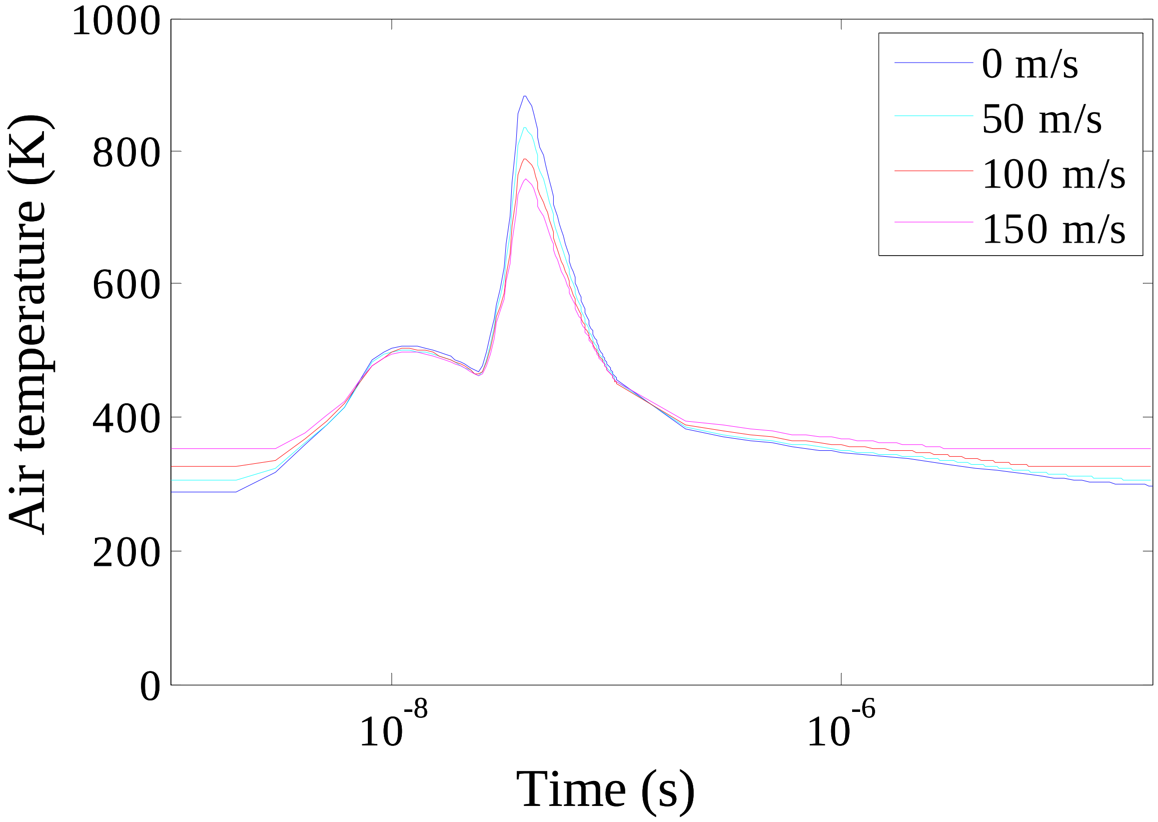

Figure 15: maximum air temperature reached

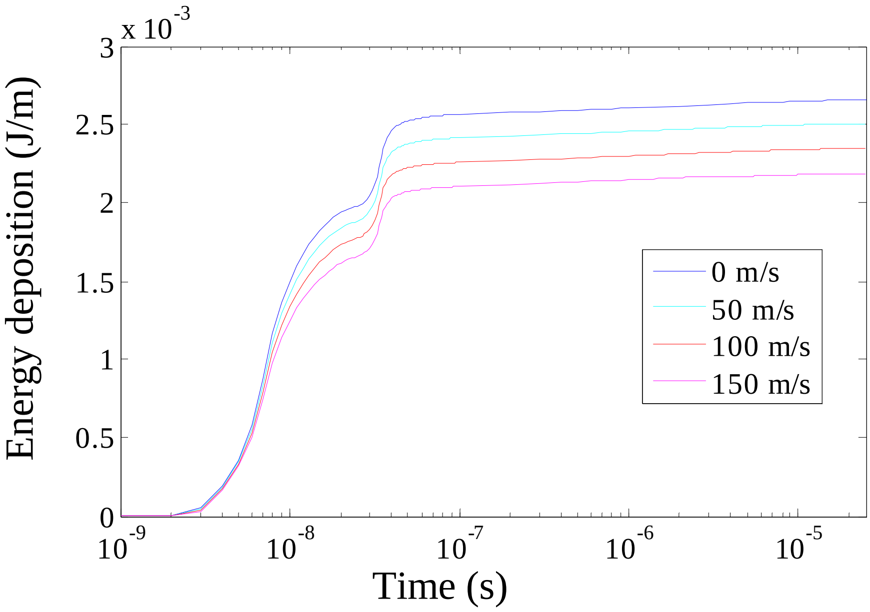

Figure 16: Total energy deposition in the neutral gas

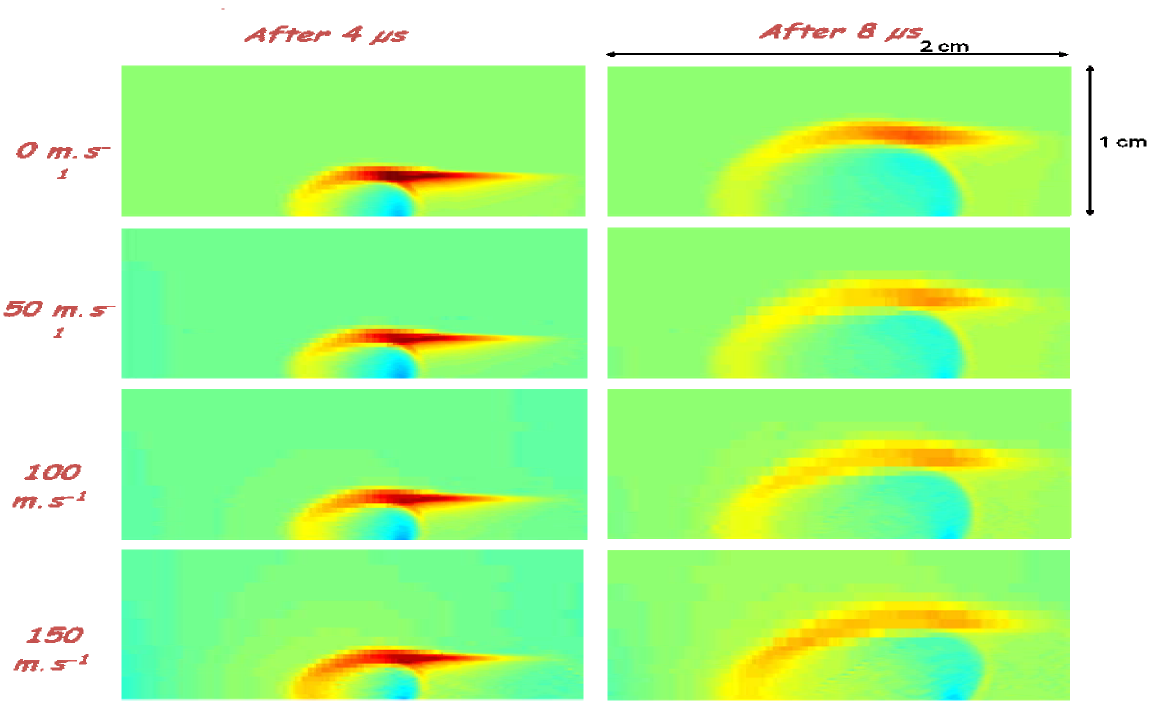

Figure 17: Pressure wave interaction with the external airflow showing the modification of the pressure wave (see previous report and Ref. [2]) at two different times (indicated on top of the figures) , and for external flows from 0 to 150 m/s (indicated on the left of the figures)

I.6 CONCLUSION

The sensitivity of the thermal effects created by a nanosecond pulsed SDBD on the neutral gas has been investigated. The amplitude of the voltage pulse seems to be a natural and efficient driving parameter of the effect. The duration of the pulse can be optimized as well. The rise time is also an important parameter that must be investigated. Some trends of the behavior of the device operating in an external airflow have been identified.

II. ACCURACY OF THE RESULTS: A MODEL COMPARISON

The purpose of this section is to assess the sensitivity of the results to the numerical schemes used for solving the charged particles transport equations. Two numerical methods are considered. The first one is based on the exponential scheme of Scharfetter and Gummel, semi-implicitely coupled with Poisson's equation. This method first order in time and space. The second method is based on the MUSCL scheme which is asynchronously integrated in time with second order space accuracy and first order time accuracy.

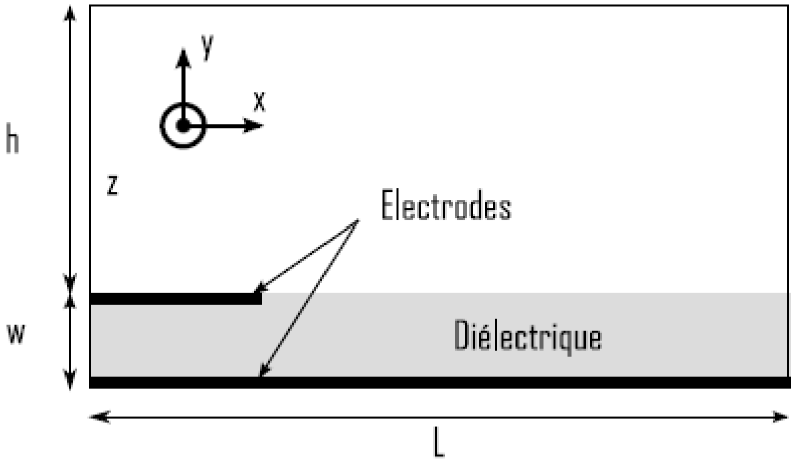

Figure 18: Simulation domain for model comparison

II.1 SINUSOIDAL VOLTAGE APPLIED ON THE SDBD

In this case the geometry is the following: L=2.8 mm, w=0.1 mm, ε_r=4 and the upper electrode length is 0.35 mm. The mesh is composed of a 400x140 grid of uniform square cells of 7 µm.

A 8kV/8kHz sinus is imposed on the upper electrode for two periods. Figure 19 & 20 shows the current response of each simulation. In the potential rise phase, the semi-implicit scheme solution consists in less numerous current pulses than the asynchronous scheme with higher peak values. During the potential drop phase, the situation is inverted. These data are difficult to compare with experiments because in real life the problem is not homogenous in the spanwise direction. However the real question is how the numerical scheme affects the computation of the averaged EHD force. The total time-averaged horizontal EHD force, which is the useful parameter if ones intends to study wall jet airflow generation, is quite of the same order of magnitude for both schemes. The semi-implicit scheme gives 0.0212 N/m whereas the asynchronous scheme gives 0.0236 N/m. Some differences are present in the space distribution of the force as shown on Figs. 21. The force seems to be more concentrated in the electrode tip vicinity for the asynchronous scheme.

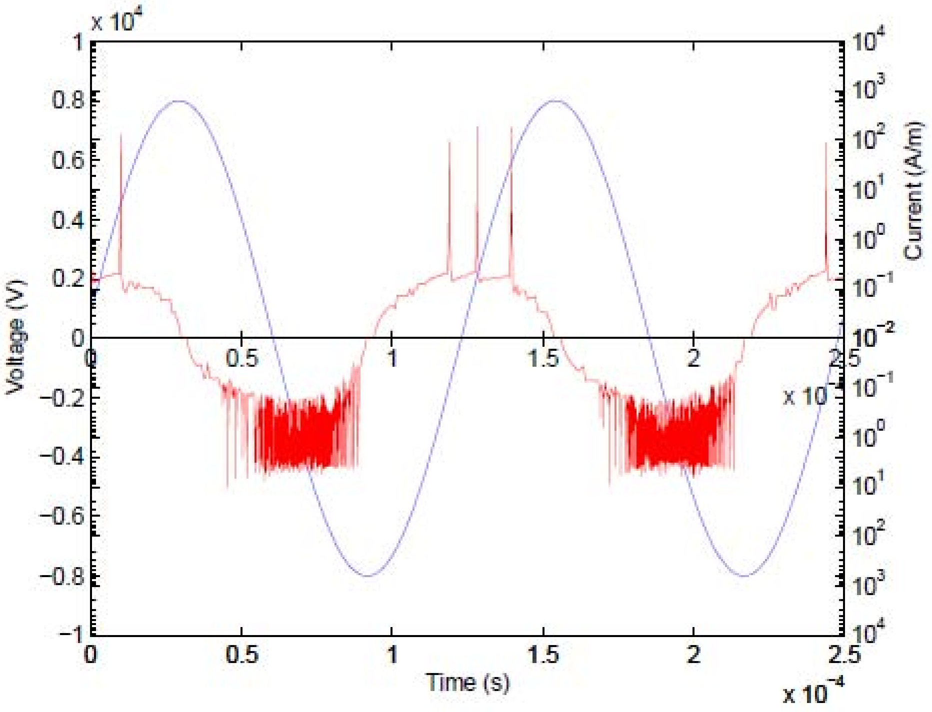

Figure 19: Current vs voltage for the semi-implicite scheme

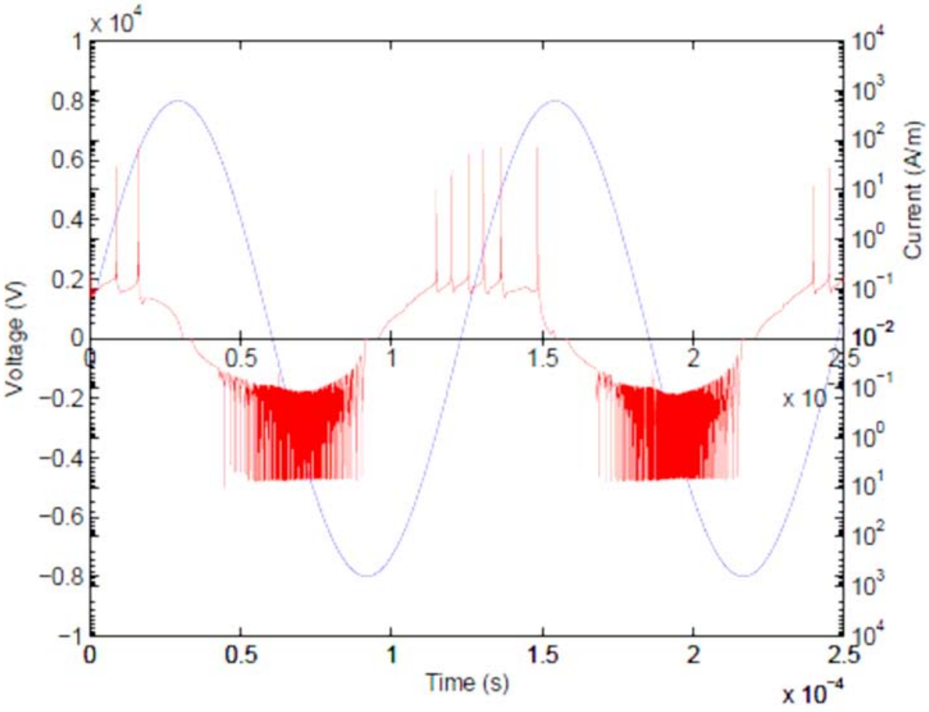

Figure 20:Current vs voltage for the asynchronous scheme

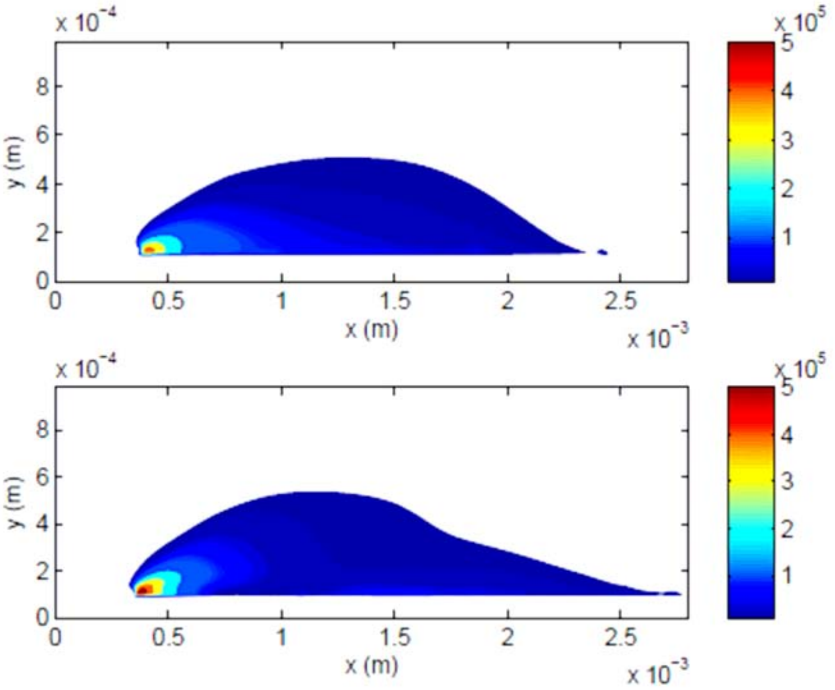

Figure 21: Horizontal time-averaged EHD force for semi-implicit (top) and asynchronous(bottom) schemes

II.2 CONCLUSION

Two numerical schemes have been compared in terms of EHD force computation. Although the calculated currents are not identical (number of pulses per cycle and values of the peak currents are different), the trends are very similar. The integrated EHD forces are equal within 10% and the space distributions of the forces are similar.

II SUMMARY AND CONLUSIONS OF THIS WORK ON "STUDIES OF THE ELECTROHYDRODYNAMIC FORCE PRODUCED IN A DIELECTRIC BARRIER DISCHARGE FOR FLOW CONTROL"

III.1 ION WIND

The mechanisms of ion wind generation in surface dielectric barrier discharges (SDBDs) is identical to the one in corona discharges. The electrohydrodynamic force (EHD) generated in SDBDs for moderate increase rates of the applied voltage is, as in corona discharges, due to the development of a unipolar region above the dielectric surface, where ion space charge is dominant and ions transfer momentum to the neutral gas. For very fast rise (few ns) of the applied voltage, ion wind is no longer important and the action of the discharge on the flow is different (see second part of this conclusion). SDBDs are more interesting for applications than DC corona because high current breakdown and transition to the arc regime are prevented by the use of a dielectric layer. There is no evidence that SDBDs can generate larger ion wind than DC corona discharges.

Due to the presence of a dielectric layer, SDBDs must be operated with a time varying voltage. For a sinusoidal regime and in the usual electrode configuration of SDBDs for flow control applications, transient ion clouds develop above the dielectric surface at each half cycle. During the part of the cycle when the exposed electrode is an anode (positive part of the cycle), a positive ion cloud forms and transfers momentum to the neutral molecules. A negative ion space charge forms when the top electrode is a cathode (negative part of the cycle) and the EHD force is due to negative ions in that case. The contribution of positive ions or negative ions to the overall EHD force depends on the voltage and frequency of the applied voltage. In the positive regime, the formation of ion clouds is continuously interrupted by high current pulses (surface streamers) that are not efficient for ion wind production. In the negative regime the discharge consists of high frequency, low amplitude current pulses during which the negative ion cloud grows continuously. In the negative regime a large force per unit volume also exists in the opposite direction; this force is however limited to a very small volume corresponding the positive ion sheath around the exposed electrode (cathode in that case)

The maximum total (space and time integrated) EHD force per unit length of the electrode that we have obtained in the simulations is on the order of **100 mN/m** (see Fig. 22). This force is distributed along the surface over a length that increases with the amplitude of the applied voltage.

The best discharge efficiency for the generation of the EHD force is obtained in the simulations at low frequencies and high voltages as seen in Fig. 22. This figure shows the calculated force per unit length as a function of dissipated power, obtained by varying the amplitude and frequency of the applied voltage. Figure 22 shows that the force increases as a function of power for all frequencies, but with larger slopes at low frequencies. At "high frequencies" (eg 10 kHz), the force tends to saturate at lower values when the dissipated power increases. The relative importance of the contribution of the positive and negative ions is also shown on Fig. 22 (see caption to Fig. 22). For a given frequency, the relative contribution of negative ions is dominant at higher voltages. The transition between dominant contribution of positive and negative ions occurs at lower power for higher frequencies.

The model results show excellent qualitative and good quantitative agreement with experiments. Systematic calculations of the velocity fields corresponding to the EHD force distributions deduced from this plasma model would be useful. The model results can also be used to provide scaling laws for the space distribution of the EHD force as a function of voltage amplitude and frequency. This would provide a good alternative to the model of Susen (eg Susen and Huang, 44th AIAA Aerospace Sciences Meeting and Exhibit, 9 - 12 January 2006, Reno, Nevada, paper AIAA 2006-877), which is used by several groups in the US but is lacking of solid physical basis.

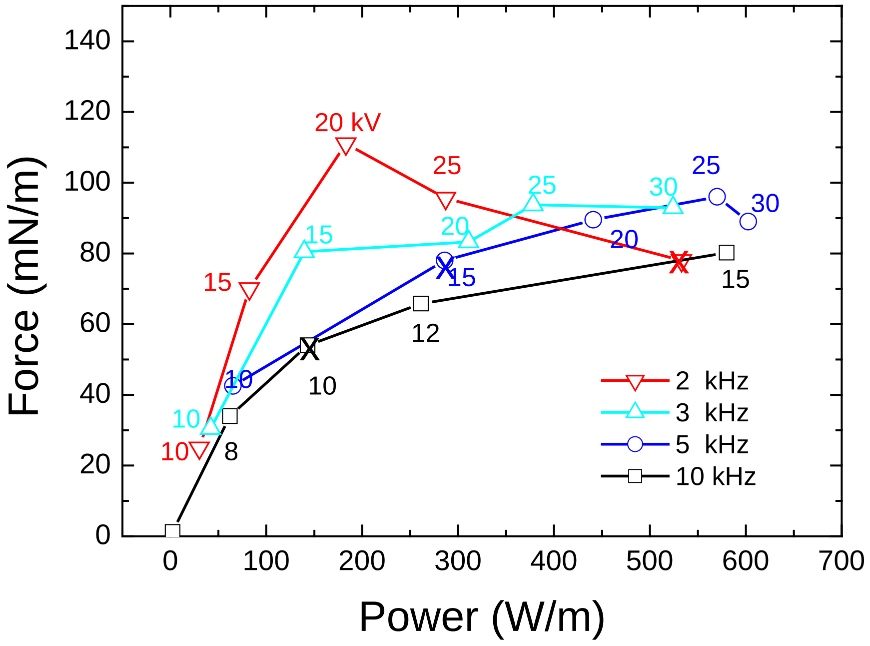

Figure 22: Calculated EHD force parallel to the surface, per unit length of the electrode, as a function of the power per unit length, for different voltage amplitudes and frequencies of the sinusoidal voltage. The curves are plotted for constant frequencies. The value of the voltage amplitude is also indicated for each point. The X on the2, 5, and 10 kHz curves shows the limit, along the curves, where the contributions of positive and negative ions to the overall force are equal. On the right of these points (larger power) the contribution of negative ions is dominant, while the contribution of positive ions is dominant on the left of the points marked with an X. The dielectric layer thickness is 1 mm and the length and height of the simulation domain are 8 mm and 4 mm respectively (same data as Fig. 14 of previous report).

III.2 NANOSECOND DISCHARGES

For a given power dissipated in the discharge, Figure 22 shows that the EHD force decreases when the frequency increases. This trend is also valid for other voltage waveforms. When using voltage pulses, the EHD force decreases when the voltage rise becomes very fast. However it has been shown experimentally by Starikovskii et al. that high voltage pulses with very short rise times (“nanosecond voltage pulses” or “nanosecond regime”) can have an effect on the flow.

The nanosecond discharge regime has been simulated in this work, and its possible aerodynamic effects have been studied by coupling the discharge model with Navier Stokes equations. The results confirm that the EHD force generated in the nanosecond regime is negligible and show that the fast heating of the gas in the vicinity of the exposed electrode can lead to a large temperature increase in a short time, giving rise to the development of micro shockwaves. These pressure waves may be responsible for the observed aerodynamic effects. Further work is needed to fully understand the interaction of the pressure waved generated by the nanosecond discharges with the external flow.

REFERENCES

[1] A. Starikovskii , D. Roupassov, A. Nikipelov, and M. Nudnova , *SDBD plasma actuator with nanosecond pulse periodic discharge*, Plasma Sources Sci. Technol. **18** 034015 (2009)

[2] T. Unfer, and J.P. Boeuf , *Modeling of a nanosecond surface discharge actuator*, J. Phys. D: Appl. Phys. **42** 194017 (2009)

ATTACHED PAPERS PUBLISHED IN THE FRAME OF THIS CONTRACT

Y Lagmich, Th Callegari, L C Pitchford and J P Boeuf, *Model description of surface dielectric barrier discharges for flow control* , J. Phys. D: Appl. Phys. 41 095205 (2008)

J.P. Boeuf, Y. Lagmich, L. Pitchford, *Contribution of positive and negative ions to the electrohydrodynamic force in a dielectric barrier discharge plasma actuator operating in air*, J. Appl. Phys. 106 023115 (2009)

T. Unfer, and J.P. Boeuf , *Modeling of a nanosecond surface discharge actuator*, J. Phys. D: Appl. Phys. **42** 194017 (2009)

IOP Publishing Journal of Physics D: Applied Physics
J. Phys. D: Appl. Phys. **41** (2008) 095205 (10pp) doi:10.1088/0022-3727/41/9/095205

Model description of surface dielectric barrier discharges for flow control

Y Lagmich, Th Callegari, L C Pitchford and J P Boeuf

LAPLACE, Université de Toulouse, CNRS, 118 route de Narbonne, 31062 Toulouse, France

Received 29 January 2008, in final form 29 February 2008
Published 3 April 2008

Abstract
This paper presents a study of the development of a surface dielectric barrier discharge in air under conditions similar to those of plasma actuators for flow control. The study is based on results from a 2D fluid model of the discharge in air that provides the space and time evolution of the charged particle densities, electric field and surface charges. The electrohydrodynamic (EHD) force associated with the momentum transfer from charged particles to neutral molecules in the volume above the dielectric layer is also deduced from the model. Results show that the EHD force is important not only during the positive part of the sinusoidal voltage cycle (i.e. when the electrode on top of the dielectric layer plays the role of the anode) but also during the negative part of the cycle (cathode on top of the dielectric layer). During the positive part of the cycle, the EHD force is due to the formation of a positive ion cloud that is periodically interrupted by high current breakdown. The EHD force during the negative part of the cycle is due to the development of a negative ion cloud that continuously grows during the successive high frequency current pulses that form in this regime.

(Some figures in this article are in colour only in the electronic version)

1. Introduction

Surface dielectric barrier discharges (DBDs) at atmospheric pressure can generate a flow or modify the boundary layer of a flow and have been proposed as actuators for flow control [1–4]. The momentum transfer from charged particles to neutral molecules generates an electrohydrodynamic (EHD) force that can be used to modify the airflow profile within the boundary layer in order to control the laminar–turbulent transition, reduce the drag and reattach or stabilize the flow. The ion wind in corona discharges [5, 6] is a good example of flow generation due to the momentum transfer from charged particles to neutral molecules in a gas discharge.

In recent papers [7–9], we presented studies of surface DBDs in pure nitrogen and showed that the EHD force was due to the momentum transfer from positive ions to neutral molecules during the formation of a non-neutral positive ion cloud above the surface when the electrode above the dielectric layer plays the role of an anode. Once the size and density of the positive ion cloud reach critical values, a high current breakdown occurs, characterized by the development of a high density filamentary plasma along the dielectric surface. The discharge during the positive part of the cycle is composed of successive phases of ion cloud formation and high current breakdown. The frequency of the high current pulses increases when the slope of the voltage waveform increases. The spatial extension of the positive ion cloud (and of the EHD force) is limited by these breakdown events and increases when the slope of the applied voltage decreases or when the capacitance of the dielectric layer decreases.

In this paper we study a surface DBD in air. We show that the discharge development during the positive part of the cycle is the same as in pure nitrogen but that the negative half cycle is different because of the negative ion generation in air. The negative part of the cycle is also composed of current pulses, but with a frequency much larger than in the positive case and of much lower intensity. A negative ion cloud forms and continuously grows during the negative part of the cycle. This ion cloud can generate an EHD force as large or even larger than the force generated by positive ions during the positive phase.

In section 2 we recall the principles of the model and of the force generated by momentum transfer between charged particles and neutrals. Section 3 describes the discharge mechanisms for positive and negative ramp voltage waveforms. Conclusions are drawn in section 4.

2. EHD force per unit volume and discharge model

As discussed in previous publications [7–9], the EHD force per unit volume in electric discharges is due to momentum transfer from charged particles to neutral particles. Neglecting the mean velocity of the neutral particles with respect to the charged particle mean velocities, the EHD force can be written as (the indices 'e', 'i' and 'n' referring to electrons, positive ions and negative ions, respectively)

$$\boldsymbol{f}_{\mathrm{e,i,n}} = n_{\mathrm{e,i,n}} m_{\mathrm{e,i,n}} \nu_{\mathrm{me,i,n}} \boldsymbol{u}_{\mathrm{e,i,n}}, \tag{1}$$

where $n_{\mathrm{e,i,n}}$ are the charged particle densities, $m_{\mathrm{e,i,n}}$ their masses, $\nu_{\mathrm{me,i,n}}$ the momentum exchange frequencies for electron–neutral, positive ion–neutral and negative ion–neutral collisions and $\boldsymbol{u}_{\mathrm{e,i,n}}$ the charged particle mean velocities.

Writing the mobility of species 's', as $\mu_s = e/(m_s \nu_{\mathrm{m}s})$, the total force per unit volume $\boldsymbol{f}$ is

$$\boldsymbol{f} = \frac{\boldsymbol{j}_{\mathrm{i}}}{\mu_{\mathrm{i}}} - \frac{\boldsymbol{j}_{\mathrm{e}}}{\mu_{\mathrm{e}}} - \frac{\boldsymbol{j}_{\mathrm{n}}}{\mu_{\mathrm{n}}}. \tag{2}$$

In the conditions of atmospheric discharge plasma actuators, we have seen (see [7–9]) that the dominant contribution to the EHD force comes from the drift terms of the current densities of equation (2), i.e.

$$\boldsymbol{j}_s \approx e n_s \mu_s \boldsymbol{E}. \tag{3}$$

We can therefore write

$$\boldsymbol{f} = \frac{\boldsymbol{j}_{\mathrm{i}}}{\mu_{\mathrm{i}}} - \frac{\boldsymbol{j}_{\mathrm{e}}}{\mu_{\mathrm{e}}} - \frac{\boldsymbol{j}_{\mathrm{n}}}{\mu_{\mathrm{n}}} \approx e(n_{\mathrm{i}} - n_{\mathrm{e}} - n_{\mathrm{n}})\boldsymbol{E}. \tag{4}$$

The force per unit volume acting on the neutral molecules is therefore equal to the Coulomb force acting on the charged particles, which means that the momentum gained by the charged particles in the electric field is exactly and locally balanced by collisions, and entirely transmitted to neutral molecules. One consequence of equation (4) is that the EHD force is zero in a first approximation for a quasi-neutral plasma (see [7] for a more explicit discussion). Equation (4) indicates that the EHD force is large in regions of the discharge with a large electric field and where the space charge is non-zero (positive or negative). This is the case, for example, in the cathode sheath regions of glow discharges or in the drift region of corona discharges.

In this paper, the space and time variations of the EHD force are deduced from a numerical model of the discharge. The model is based on fluid equations for electrons and ions, coupled with Poisson's equation for the electric field. The time dependent electron and ion continuity equations with a drift–diffusion flux are coupled with Poissons's equation and integrated in time using the Scharfetter–Gummel scheme with a semi-implicit method (see [7–9] and references therein).

In this study, a very simple model of the plasma chemistry has been considered, with one type of positive ion and one type of negative ion species (for air) and no complex plasma chemistry is included. Negative ions in air are supposed to be formed in two-body and three-body reactions. Electron–ion and ion–ion recombination are taken into account but negative ion detachment is not considered.

The continuity equation for the charged particles of type s (s = e, i, or n) reads

$$\frac{\partial n_s}{\partial t} + \nabla \cdot \boldsymbol{\Gamma}_s = S_s, \tag{5}$$

where the charged particle flux $\boldsymbol{\Gamma}_s$ has a drift–diffusion form

$$\boldsymbol{\Gamma}_s = \pm n_s \mu_s \boldsymbol{E} - D_s \nabla n_s, \tag{6}$$

where the + sign applies to positive ions and the − sign is for electrons and negative ions. μ_s and D_s are the mobility and the diffusion coefficient of species s.

The source terms S_s of the continuity equations are defined by

$$\begin{aligned} S_{\mathrm{e}} &= (\alpha - \eta)|\boldsymbol{\Gamma}_{\mathrm{e}}| - r_{\mathrm{ei}} n_{\mathrm{e}} n_{\mathrm{i}}, \\ S_{\mathrm{i}} &= \alpha|\boldsymbol{\Gamma}_{\mathrm{e}}| - r_{\mathrm{ei}} n_{\mathrm{e}} n_{\mathrm{i}} - r_{\mathrm{in}} n_{\mathrm{i}} n_{\mathrm{n}}, \\ S_{\mathrm{n}} &= \eta|\boldsymbol{\Gamma}_{\mathrm{e}}| - r_{\mathrm{in}} n_{\mathrm{i}} n_{\mathrm{n}}, \end{aligned} \tag{7}$$

α and η are the ionization and attachment coefficient, respectively; r_{ei} and r_{in} are the electron–positive ion and positive ion–negative ion recombination coefficients.

The continuity equations (5) with the flux from the momentum equations (6) and the source terms from equation (7) are coupled with Poisson's equation:

$$\vec{\nabla} \cdot (\varepsilon \vec{E}) = \frac{e}{\varepsilon_0}(n_{\mathrm{i}} - n_{\mathrm{e}} - n_{\mathrm{n}}) + \frac{e}{\varepsilon_0}\sigma \delta_S \tag{8}$$

σ, in the last term of equation (8), is the surface charge density, which is non-zero only on the dielectric layer surface, as expressed by the Dirac function δ_S. The surface charge density is calculated self-consistently by integrating the electron and ion fluxes to the surface. Electrons and ions in each surface element are supposed to recombine instantly with oppositely charged particles on the surface if present.

The current calculated in the model and displayed in some of the figures below is the displacement current on the bottom electrode. Because of the boundary conditions (zero current out of the simulation domain), this current is also equal to the sum of the electron, ion and displacement currents on the electrode above the surface (the displacement current is calculated on both sides of the electrode).

When the electric field is directed towards the dielectric layer surface, secondary electron emission is taken into account by the boundary condition: $J_{\mathrm{e},\perp} = \gamma J_{\mathrm{i},\perp}$ where $J_{\mathrm{e},\perp}$ and $J_{\mathrm{i},\perp}$ are the components of the electron and ion current densities perpendicular to the dielectric surface and γ is the secondary electron emission coefficient due to ion impact. γ is set to 0.05 in the calculations below.

The simulation domain is shown in figure 1. The dielectric layer permittivity ε_r is set to 5, unless otherwise indicated. The applied voltage waveform between the electrodes is supposed to be linearly increasing with time (ramp voltage), with a slope η_V, on the order of 100 V μs^{-1} or so (this is consistent with typical experiments for sinusoidal voltage waveform of 5–20 kV amplitude and frequencies in the 1–10 kHz range).

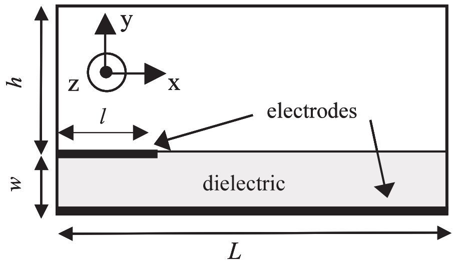

Figure 1. Simulation domain. The calculations below have been performed mainly for the two sets of conditions: (L = 4 mm, w = 0.5 mm, h = 1.5 mm, l = 0.25 mm) and (L = 8 mm, w = 1 mm, h = 3 mm l = 0.5 mm).

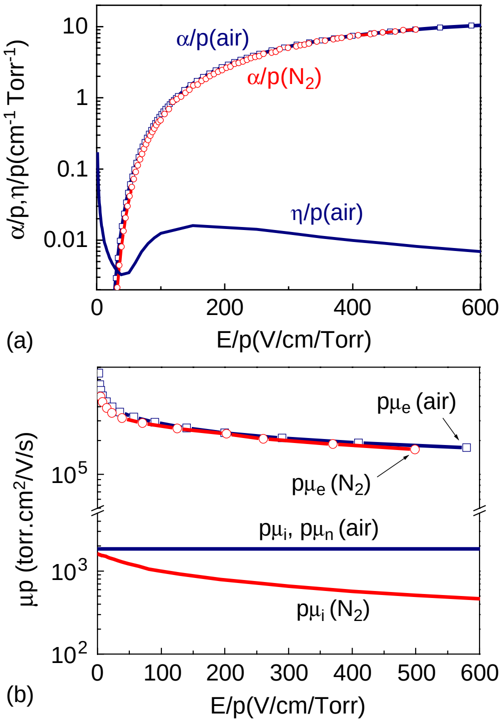

Figure 2. (*a*) Reduced ionization and attachment coefficients used in the model as a function of reduced electric field (at 300 K); (*b*) reduced electron and ion mobilities as a function of reduced electric field (at 300 K). The air data are used in the present model; the nitrogen data also shown for comparison in this figure were used in [7–9].

The ionization and attachment coefficients are supposed to depend on the local reduced electric field as in [7–9] and are obtained with the BOLSIG+ electron Boltzmann equation solver [10] (three-body attachment in oxygen is properly taken into account with a separate cross section). The electron–positive ion and positive ion–negative ion recombination coefficients r_{ei} and r_{in} are supposed to be equal to $2 \times 10^{-7}\,\mathrm{cm^3\,s^{-1}}$. The electron and ion diffusion coefficients are chosen so that $D_\mathrm{e}/\mu_\mathrm{e} = 1\,\mathrm{V}$ and $D_{\mathrm{i,n}}/\mu_{\mathrm{i,n}} = 0.01\,\mathrm{V}$. Ionization and attachment coefficients and mobilities used for nitrogen in [7–9] and in air in this study are shown in figure 2. A constant mobility has been used for positive and negative ions in air.

A similar physical model of surface DBD plasma actuators has been recently published by Likhanskii *et al* [11].

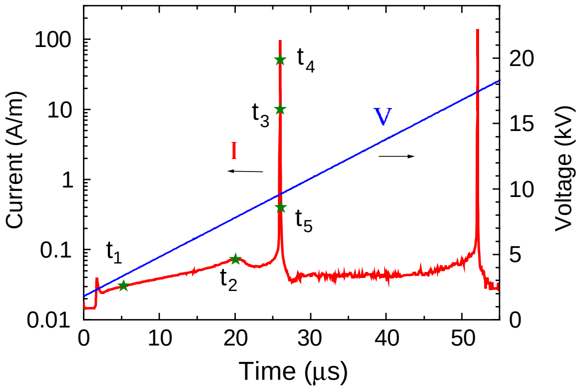

Figure 3. Calculated current waveform in air in the geometry of figure 1 and for a positive voltage slope (also shown) $\eta_V = +300\,\mathrm{V}\,\mu\mathrm{s}^{-1}$. The symbols indicate the times at which the charged particle densities and electric potential are shown in figure 4. The permittivity of the dielectric layer ε_r is equal to 5. The dimensions of the simulation domain (see figure 1) are (L = 4 mm, w = 0.5 mm, h = 1.5 mm, l = 0.25 mm). The simulation domain is 200 × 400, i.e. the grid spacing is 10 μm.

Finally note that the numerical method used in this paper to solve equations (5)–(8) is first order accurate. More accurate, 2nd order explicit methods are being developed [12] to validate the results obtained with this model.

3. Surface DBD in air in the plasma actuator geometry

The results presented here have been obtained in air with a simplified model taking into account only one type of positive ion and one type of negative ion (see above).

Results are presented for a positive ramp voltage ('positive discharge'), i.e. linearly increasing positive voltage applied to the electrode above the dielectric layer, the electrode below the dielectric layer being grounded (the electrode below the dielectric layer is the cathode), and for a negative ramp voltage ('negative discharge'), i.e. linearly increasing negative voltage applied to the electrode above the dielectric layer, the electrode below the dielectric layer being grounded (the electrode above the dielectric layer is the cathode).

We find that, for positive ramp voltage waveform (anode above the dielectric surface), most of the features described in previous papers [7–9] for nitrogen are qualitatively valid for air. For a negative ramp voltage waveform (cathode above the dielectric surface) a significant EHD force, directed away from the top electrode (as in the positive case), is present above the surface and is due to the formation of a negative ion cloud. Note that in pure nitrogen, we found in [8] that the EHD force for a negative ramp voltage was negligibly small.

We present results in air for positive and negative ramp voltage waveforms in the two subsections below.

3.1. Positive ramp voltage waveform

3.1.1. Time evolution of the positive surface DBD. The calculated current waveform in air shown in figure 3 for a positive ramp voltage (anode above the dielectric surface) consists of high intensity pulses separated by low current

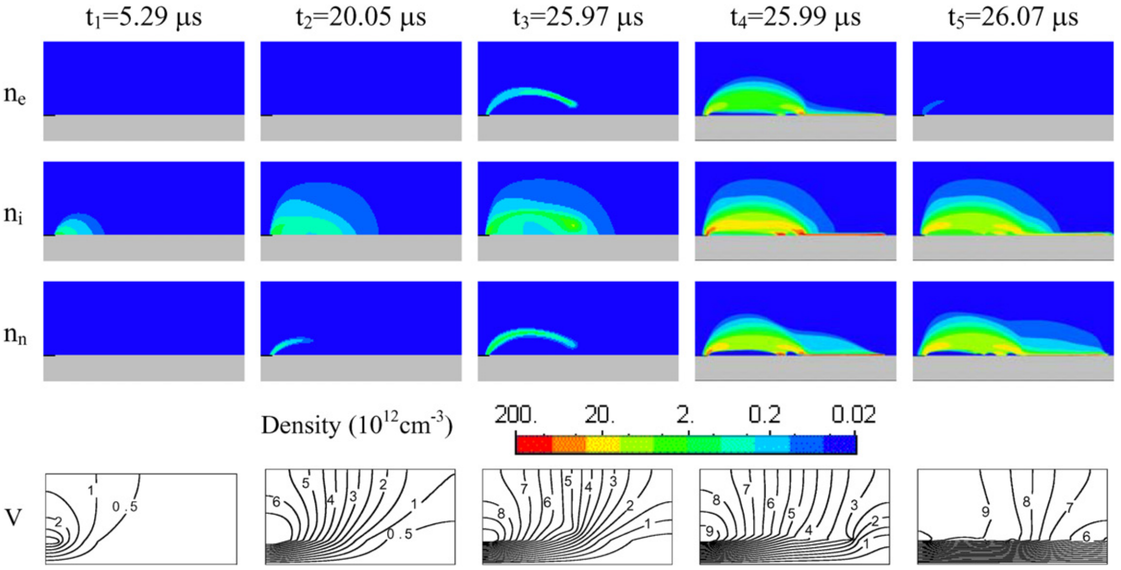

Figure 4. Distribution of charged particle densities and potential at different times for a discharge in air in the conditions of figure 3 for a ramp voltage $\eta_V = +300\,\mathrm{V}\,\mu\mathrm{s}^{-1}$. The colour/greytone scale for the charged particle densities is a log scale over four decades. The voltage contours are indicated in kilovolts. (Colour online only.)

phases, and is similar to the current waveform calculated in nitrogen (see [7–9]).

We see in figure 4 that the low current phase is associated with the formation of a positive ion cloud above the dielectric surface. This ion cloud forms and starts to grow as soon as the potential drop along the dielectric surface becomes sufficient for the discharge to become self-sustained. Under the assumptions of our model, electrons are generated at the dielectric surface by ion bombardment. They multiply in the large electric field above the surface. In the low current phase (e.g. times t_1 and t_2 in figure 4), the field distortion due to the ion space charge build up is not sufficient to lead to a significant growth of the electron density, and the electron density is small with respect to the positive ion density (no plasma). Due to the continuous increase in the applied voltage and to the dielectric nature of the surface, the ion cloud grows and expands along the surface. When the ion space charge reaches a critical value, around time $t_3 = 25.97\,\mu$s, the geometric field becomes significantly distorted. The reconfiguration of the electric field due to the plasma formation leads to a significant increase in the electron multiplication and of the discharge current (current peaks in figure 3). A quasi-neutral plasma thus forms and a filament propagates with a high velocity along the surface (times t_3, t_4 of figure 4). At the end of the current pulse (around time t_5) most of the electrons are attached and the post-discharge plasma is composed of mainly positive and negative ions. The dielectric layer surface is positively charged and the electric potential immediately above the surface is near the anode potential. After time t_5, the post-discharge plasma diffuses and recombines. Since the applied voltage is supposed to increase linearly, the same phenomena (formation and growth of a positive ion cloud, followed by high current breakdown) are repeated at a later time (around $t = 52\,\mu$s, see figure 3) and a periodic regime is reached in the simulation.

It is interesting to look more closely at the time evolution of the electric field above the dielectric surface. Figures 5(*a*) and (*b*) show the distribution of the total electric field immediately above the surface, as a function of position along the surface, before and after high current breakdown, respectively. At time $t = 1.66\,\mu$s (figure 5(*a*)) the electric field is not perturbed by the space charge and is only defined by the electrode and dielectric arrangement. The electric field distortion due to

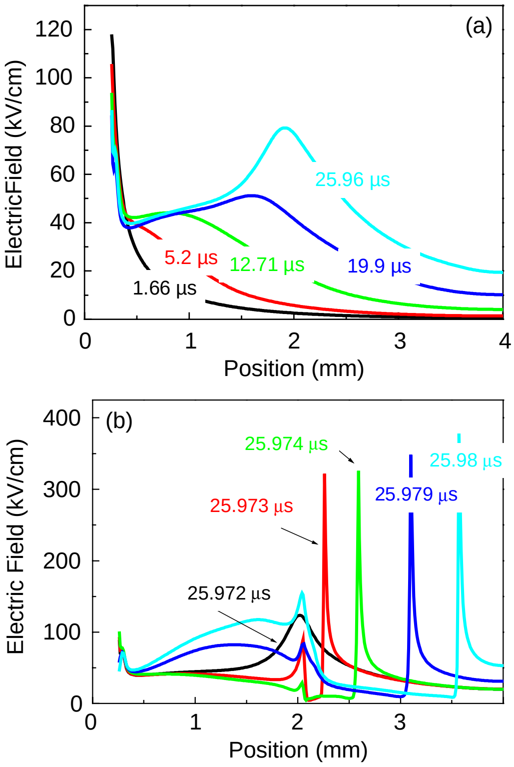

Figure 5. Distribution along the surface (x direction, see figure 1) of the electric field above the surface at different times (*a*) during the ion cloud expansion (low current phase) and (*b*) during the high current breakdown. Same conditions as figures 3 and 4.

the ion cloud appears quickly (see the field at $t = 5.2\,\mu$s in figure 5(*a*)). The field decreases in the vicinity of the electrode tip, and increases in the ion cloud, away from the electrode tip. The region of large electric field extends as the ion cloud grows, until breakdown occurs around time $t = 25.96$–$25.97\,\mu$s (see figures 5(*a*) and (*b*)).

The field evolution above the surface after $t = 25.97\,\mu$s in figure 5(*b*) is very similar to the electric field during streamer propagation. A plasma channel, characterized by a drop of the electric field, forms. This channel is surrounded by two large electric field regions on the cathode side and on the anode side, which can be qualified as cathode and anode streamers. The cathode streamers propagates at a high velocity (about 1.5 mm in 7 ns between $t = 25.973\,\mu$s and $t = 25.98\,\mu$s, i.e. 2×10^7 cm s^{-1}). Note that photoionization is not included in the model and that the cathode streamer propagation in the simulations is due to secondary emission from the dielectric surface and/or to charges remaining in the volume over the dielectric surface from previous current pulses. Since the discharge takes place very close to the surface it seems reasonable to assume that photoionization does not play an important role in these surface DBDs (even a very low electron emission from the surface can provide a fast propagation of the discharge along the surface). Nevertheless, the exact propagation velocity of the streamer along the surface and the time interval between successive pulses are very difficult to predict accurately. Moreover the numerical method being first order in space, this can have some influence of the propagation velocity and on the time interval between current pulses. Work is in progress to perform sensitivity analyses of the results to parameters such as the secondary emission coefficient, and to study the effect of the accuracy of the numerical method on the results, by using second order methods as described in [12]. Preliminary results show that the main conclusions of this paper are not altered when the secondary emission coefficient is varied or when a more accurate method [12] is used. These results will be discussed in forthcoming publications.

3.1.2. EHD force. As we found in the case of a positive ramp voltage in pure nitrogen in [8, 9], the EHD force in air is important only during the low current phases between high current pulses (see figure 5). Figure 6 shows the variations as a function of time *t*, of the space integrated EHD force parallel to the surface, averaged in the time interval [0,t] and defined as

$$\overline{\boldsymbol{F}_{||}}(t) = \frac{1}{t}\int_0^t \boldsymbol{F}_{||}(t')\,\mathrm{d}t' = \frac{1}{t}\int_0^t \mathrm{d}t' \int \boldsymbol{f}_{||}(x, y, t')\,\mathrm{d}x\,\mathrm{d}y, \tag{9}$$

where the instantaneous EHD force per unit volume, $\boldsymbol{f}$, is defined in equation (4). $\overline{\boldsymbol{F}_{||}}$ is a force per unit length of the electrode.

The EHD force $\overline{\boldsymbol{F}_{||}}$ in figure 6 is represented for different values of the ramp voltage slope and for different combinations of dielectric layer thickness and permittivity. The oscillations of the force in figure 6 are associated with the current pulses (the force increases only during the low current phase between the pulses). We see that the frequency of these oscillations increases with increasing voltage slope, and with the dielectric permittivity to thickness ratio (related to the capacitance of the dielectric layer), as was already found in pure nitrogen [8]. However, we note that the time averaged EHD force tends to reach, at steady state, a value on the order of 0.12 mN m^{-1}, which is not very sensitive to these parameters. We also find, as in [8, 9] for pure nitrogen, that although the space and time integrated force is not very dependent on the conditions, the space distribution of the force over the surface is very sensitive to the ramp voltage slope and to the dielectric capacitance.

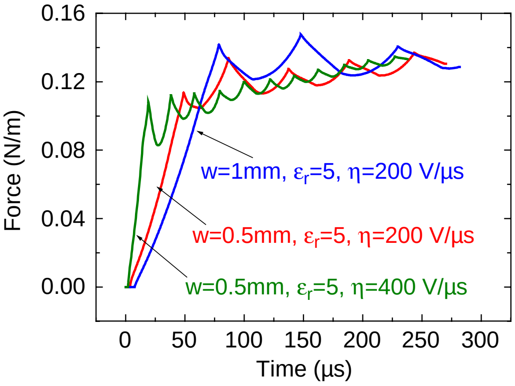

Figure 6. Variations as a function of time *t*, of the EHD force per unit length (averaged in time between 0 and *t*, see equation (9)) parallel to the surface, for different slopes of the positive ramp voltage and for different values of the dielectric thickness and permittivity. Air, simulation domain of dimensions $L = 8$ mm and $w + h = 4$ mm, $l = 0.5$ mm (see figure 1).

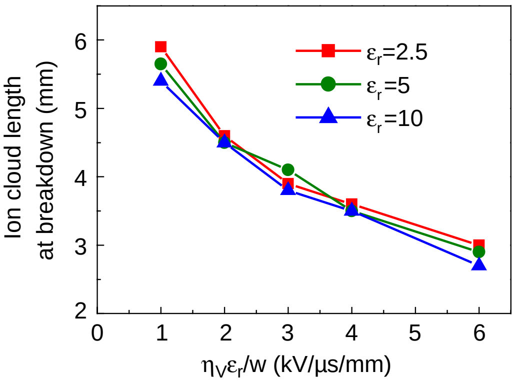

Figure 7. Extension of the positive ion cloud along the surface at breakdown for a positive voltage slope, as a function of the parameter $\eta_V \varepsilon_r / w$, for different values of the dielectric permittivity in air for simulation domain dimensions $L = 8$ mm, $w = 1$ mm and $h = 3$ mm, $l = 0.5$ mm.

The length of the ion cloud just before breakdown, i.e. the spatial extension of the EHD force, is represented in figure 7 as a function of $\eta_V \varepsilon_r / w$, which is proportional to the charging current density of the dielectric layer. We see in figure 7 that the spatial extension of the EHD force along the surface depends only on the scaling parameter $\eta_V \varepsilon_r / w$, as was already shown in the case of pure nitrogen in [9].

When the slope of the ramp voltage increases, or when the capacitance of the dielectric layer increases, the size of the ion cloud at breakdown, and thus the spatial extension of the EHD force, decreases.

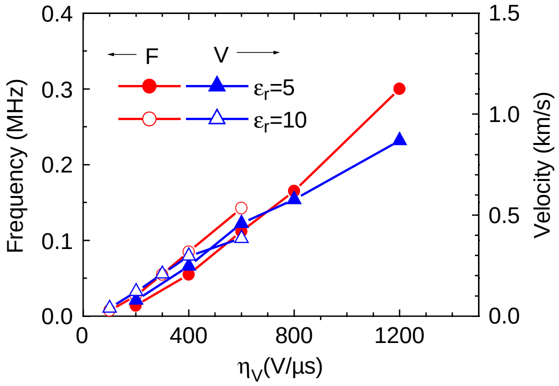

Figure 8. Frequency of the high current pulses and expansion velocity of the ion cloud as a function of the positive voltage slope for two values of the permittivity of the dielectric layer and for simulation domain dimensions $L = 8\,\mathrm{mm}$, $w = 1\,\mathrm{mm}$ and $h = 3\,\mathrm{mm}$, $l = 0.5\,\mathrm{mm}$.

It is interesting to look at the variations of the expansion velocity of the ion cloud as a function of the voltage slope η_V shown in figure 8. We see that this velocity increases practically linearly with η_V and is on the order of a few $100\,\mathrm{m\,s^{-1}}$ to $1\,\mathrm{km\,s^{-1}}$ under typical conditions. The scaling with $\eta_V \varepsilon_r / w$ is not as clear here, and we have plotted separately in figure 8 the results as a function of η_V for two different values of the permittivity. The ion cloud expansion velocity increases with η_V but with slightly different slopes for different values of the permittivity ε_r (for a given dielectric layer width). The same remark is valid for the current pulse frequency which is also represented in figure 8. Since the expansion length of the positive ion cloud is limited by breakdown, this length (shown in figure 7) is directly proportional to the ratio of the ion velocity to the pulse frequency shown in figure 8.

3.2. *Negative ramp voltage waveform*

3.2.1. Time evolution of the negative surface DBD. For negative ramp voltages (cathode above the dielectric layer), the current exhibits higher frequency pulses of smaller amplitudes, as shown in figure 9(*a*). The frequency of the oscillations is about 1 MHz in the conditions of figure 9, and the duration of the current pulse is on the order of 100 ns (see figure 9(*b*)). We found similar current oscillations in pure nitrogen (see [8]). Note that in air (figure 9) the minimum current in the oscillations increases slightly with time.

Figure 10 shows the space distribution of the electron density, positive and negation ion densities and electric potential at five different times of a single pulse, indicated in figure 9(*b*). We see that on the time scale of one current pulse the electron density is completely modulated while the ion densities slightly change in time but do not decay to zero. At time t_a before the current increase, the electron density is practically zero. We see then, at times t_b to t_d, an increase in the electron density leading to the formation of a quasi-neutral plasma in the vicinity of the electrode tip. The electron density extends beyond the plasma region (times t_c, t_d), in a region which is dominated by a negative space charge. The electron density then decays and goes to zero (time t_e) due to the charging of the dielectric surface by the electrons, leading to a potential drop along the dielectric surface and to a decrease in the electron multiplication below that of the self-sustaining condition. The decay of the electron density is also due to electron attachment, but the current oscillations are not due to attachment as it is in the Trichel regime of negative corona discharges. Note that we have shown that the current oscillations in the negative regime also exist in pure nitrogen where attachment is absent [8]. We note that at the end of the current pulse (time t_e) the densities of positive ions and negative ions at the extremity of the ion cloud away from the top electrode have increased, the negative ion density being however larger than the positive ion density. This is because of electron impact ionization and attachment during the electron transport above the surface (times t_b–t_d). We can therefore conclude that the ion space charge above the dielectric surface is negative on the average and that it expands at each current pulse due to electron attachment (and negative ion drift). We will see below that the EHD force during the negative voltage ramp is due to the negative ion space charge (negative ion cloud) that develops above the surface and expands at each current pulse.

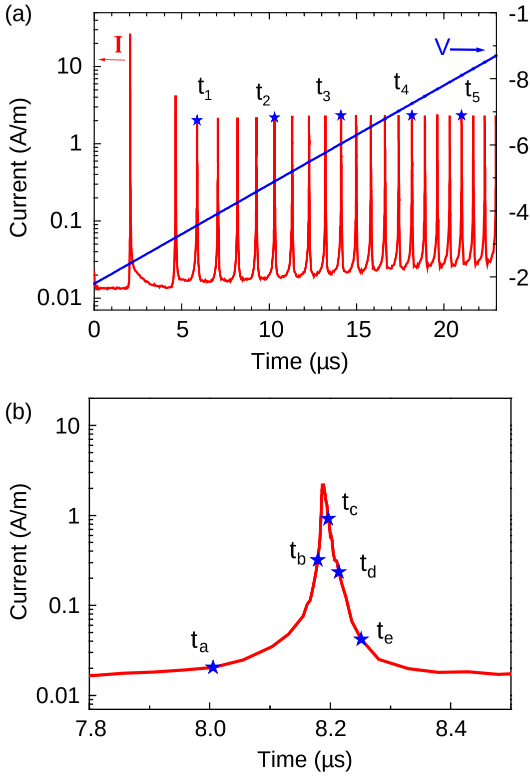

Figure 9. (*a*) Calculated current waveform in air in the geometry of figure 1 and for a negative voltage slope (also shown) $\eta_V = -300\,\mathrm{V}\,\mu\mathrm{s}^{-1}$. The symbols indicate the times at which the charged particle densities and electric potential are shown in figure 11. (*b*) Detailed view of a single current pulse. The symbols indicate the times at which the charged particle densities and electric potential are shown in figure 10. The dimensions of the simulation domain (see figure 1) are $L = 4\,\mathrm{mm}$, $w = 0.5\,\mathrm{mm}$, $h = 1.5\,\mathrm{mm}$ and $l = 0.25\,\mathrm{mm}$. The permittivity of the dielectric layer ε_r is equal to 5. The simulation domain is 200×400, i.e. the grid spacing is $10\,\mu\mathrm{m}$.

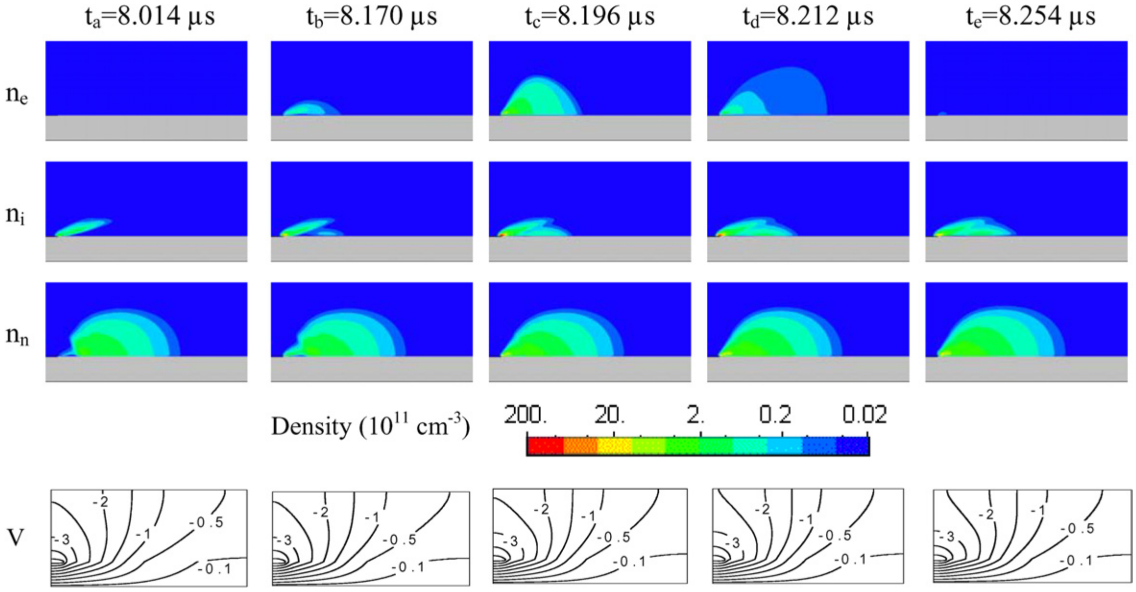

Figure 10. Distribution of charged particle densities and potential at different times for a discharge in air in the conditions of figure 9 for a ramp voltage $\eta_V = -300\,\mathrm{V}\,\mu\mathrm{s}^{-1}$, over one single current pulse (times are indicated on the current pulse of figure 9(*b*)). The colour/greytone scale for the charged particle densities is a log scale over four decades. The voltage contours are indicated in kilovolts. (Colour online only.)

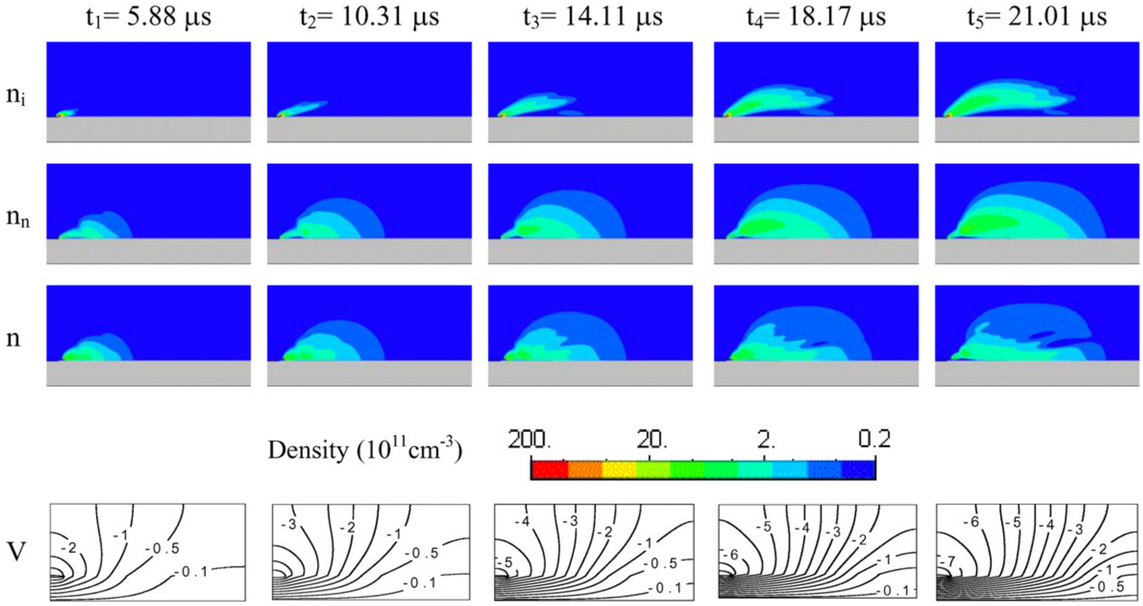

Figure 11. Distribution of the density of positive ions n_i, of negative ions n_n, of the net negative charged particle density $n = n_\mathrm{e} + n_\mathrm{n} - n_\mathrm{i}$, and of the electric potential at different times for a discharge in air in the conditions of figure 9, over several current pulses (times are indicated on the current plot in figure 9(*a*)). Only the positive values of n are represented (n is negative in the positive ion sheath near the electrode tip). Note that the colour/greytone scale for the charged particle densities is a log scale over three decades, and not on four decades, as in figure 10. The voltage contours are indicated in kilovolts. (Colour online only.)

Figure 11 shows the space distributions of the electron density, positive ion density, net density of charges and electric potential at different times, but on a longer time scale than in figure 10. The distributions are shown at the times indicated in figure 9(*a*), i.e. at the maxima of every fourth current pulse, starting at $t_1 = 5.88\,\mu\mathrm{s}$. We see clearly in this figure that the positive and negative ion clouds expand continuously during the successive pulses, and that, away from the electrode tip, the space charge is essentially negative. Due to the charging of the dielectric surface, the length of the electron paths above the electrode increases at each current pulse, and this is associated with the expansion of the positive and negative ion clouds above the surface. Note that the region in the vicinity of the electrode tip (which plays the role of the cathode) is similar to the cathode region of a glow discharge (with a strong field distortion due to the electrode geometry, as in a corona discharge).

It is interesting to look more closely at the time evolution of the surface charge and electric field above the surface.

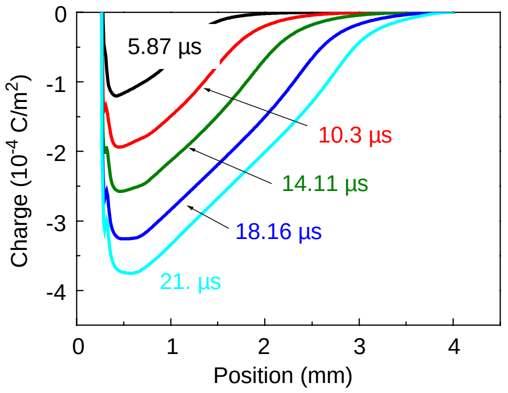

Figure 12. Space distribution of the surface charge in the x direction (see figure 1) along the surface at different times during the discharge of figures 9–11.

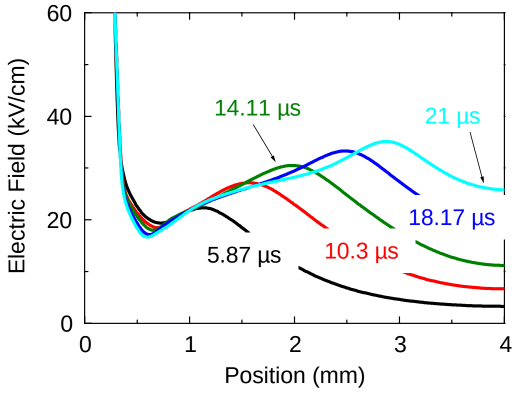

Figure 13. Space distribution of electric field above the surface at different times during the discharge of figures 9–11.

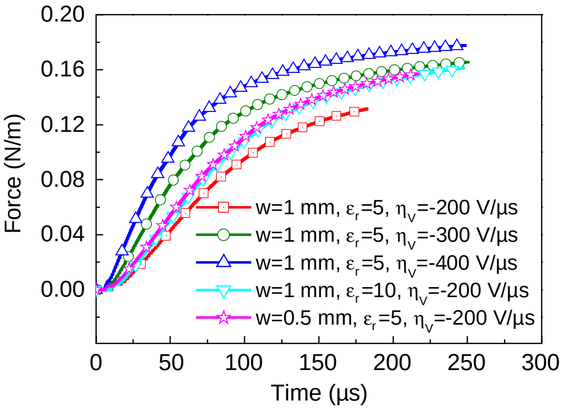

Figure 14. Time variations of the EHD force per unit length parallel to the surface for different slopes of the negative ramp voltage and for different values of the dielectric thickness and permittivity, in air and for simulation domain dimensions $L = 8$ mm and $w + h = 4$ mm, $l = 0.5$ mm (see figure 1).

Figure 12 shows the distribution of the charge along the surface (due to the charging by electrons and negative ions) at different times considered in figure 11 (and indicated in figure 9(a)). We see that the extension of the negative charges along the surface increases with time, pulse after pulse. This is consistent with the results of figure 11 above where it was shown that the electron density above the dielectric layer extends a little more at each current pulse, due to the charging of the surface. The maximum of the surface charge is located a few 100 μm away from the electrode tip and does not move significantly during the time interval considered (about 20 μs). This maximum of the surface charge and the charge along the surface within the ion clouds increase practically linearly with time, and at a constant rate along the surface. The gradient of the surface charge after the maximum is almost constant in space and time.

Figure 13 shows the distribution of the electric field immediately above the surface, at the same times as in figures 11 and 12. The electric field is large near the electrode tip, and decreases sharply away from it. We see that the electric field presents a relative maximum that moves away from the electrode tip. This maximum electric field is on the order of the breakdown field in air i.e. 30 kV cm^{-1} (the value for which ionization balances attachment). The evolution of the electric field above the surface is associated with the charging of the dielectric and the evolution of the space charge above the surface.

3.2.2. EHD force. As mentioned above, the EHD force for a negative voltage in air can be large, in contrast to the case of pure nitrogen (see [8]). The EHD force is due to the development of a negative space charge above the surface. Note that the expansion of the negative space above the surface is continuous and is not interrupted by high current breakdown, as in the case of the positive voltage (see section 3.1). Therefore, the length of the negative ion space charge above the dielectric surface is not limited by breakdown but rather by the duration of the negative phase, i.e. by the frequency of the applied voltage. One can therefore expect that the EHD force during the negative part of the cycle will play a more important role at lower voltage frequencies.

Figure 14 shows the time evolution of the space and time averaged EHD force per unit length parallel to the surface, $\overline{\boldsymbol{F}_{\|}}$ (see equation (9)), for a negative ramp voltage in different conditions (different dielectric layer permittivity and thickness, and slope of the applied voltage). We see that under these conditions, the force is only slightly dependent on the dielectric layer, tends to increase with the voltage slope and is on the same order or even higher than the force that was calculated in the case of a positive ramp voltage (see figure 6).

3.2.3. Expansion velocity of the negative space charge above the surface. The velocity of the expansion of the negative ion cloud above the surface can be defined as the velocity of the relative maximum of the electric field of figure 13. Figure 15 shows this velocity as a function of the slope of the ramp voltage, η_V. The frequency of the current pulse is also plotted as a function of η_V. We see that the ion cloud velocity expansion increases linearly with η_V and is on the order of a few 100 m s^{-1}. The increase in the ion cloud velocity with η_V is due to the fact that the charging rate of the surface increases with η_V which is consistent with the increase in the

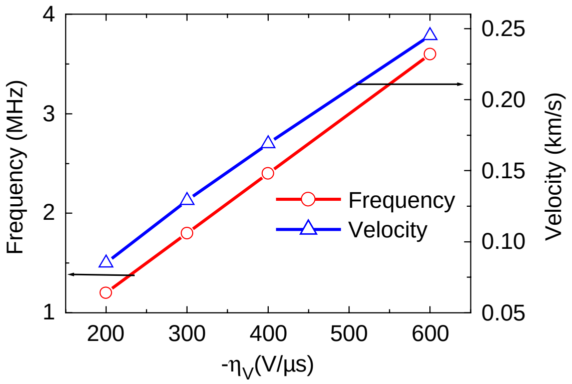

Figure 15. Frequency of the negative current pulses and expansion velocity of the ion cloud as a function of the negative voltage slope for two values of the permittivity of the dielectric layer and for simulation domain dimensions $L = 8$ mm, $w = 1$ mm, $h = 3$ mm, $l = 0.5$ mm.

current pulse frequency in figure 15. Electrons travel a larger distance above the surface for successive current pulses (see figure 11). They generate negative ions along this path, and this contributes to the expansion of the ion cloud above the surface. Note that they also generate positive ions along their path above the surface, but more negative ions are created at the extremity of the ion cloud where the field is below that for which ionization balances attachment.

The difference between the negative and the positive regime is that the expansion of the negative ion cloud is continuous during the negative regime, whereas the extent of the positive ion cloud is limited by high current breakdown in the positive regime (i.e. in the positive regime, the ion cloud expansion must restart from zero after each current pulse, which is not the case in the negative regime). We discussed in figure 7 how the expansion length of the positive ion cloud depends on the discharge parameter in the positive regime. In the negative voltage case, we can also study the expansion length of the negative ion cloud. Since this length is not limited by breakdown, we expect that the only limitation of the ion cloud expansion will be the finite duration of the sinusoidal voltage cycle. In the conditions of the discussion above, a ramp voltage was assumed, and we found (see figure 15) that the ion velocity V_{ion} increases linearly with η_V . From figure 15, we can write $V_{\text{ion}} = a\eta_V$, with $a \sim 0.4\,\text{mm}\,\text{kV}^{-1}$. We can extrapolate this result to the case of a sinusoidal voltage by writing that the average slope for a sinusoidal voltage is given by $\eta_V = 4FV$ where F and V are the voltage frequency and amplitude. Therefore the ion velocity expansion can be written as $V_{\text{ion}} = 4aFV$. Assuming that the negative discharge takes place during about 1/4 of the voltage cycle duration ($1/4F$), we find that the total expansion length L_{cloud} of the ion cloud over one cycle is actually independent of the frequency and is given by $L_{\text{cloud}} = aV$. With the numbers corresponding to figure 15 ($a \sim 0.4\,\text{mm}\,\text{kV}^{-1}$), this gives $L_{\text{cloud (mm)}} \approx 0.4V_{\text{kV}}$. Therefore we find that the maximum expansion length of the negative ion cloud for a sinusoidal voltage of amplitude e.g. 25 kV is on the order of 1 cm. These results are consistent with the optical measurements of the discharge extension as a function of voltage amplitude performed by Takizawa *et al* [13]. These measurements give an extension length of about 4 mm at 10 kV (as in the model) but the increase in the extension length with voltage in the experiments is faster than predicted by the model.

It is interesting to note that in the model, the negative ion cloud expansion length increases with applied voltage amplitude in the negative regime, while the positive ion cloud expansion in the positive regime decreases with applied voltage for a given frequency and dielectric layer properties as seen in figure 7. Note that in the optical measurements of Takizawa *et al* [13] the measured extension length is the same in the positive and negative phases. This is because the light detected in the positive phase corresponds to the filamentary discharge and not to the position of the ion cloud. During the negative phase, the measured light emission corresponds to electrons spreading along the surface. As shown in the model calculations the electrons drift across the space charge cloud at each pulse. Therefore, the measurement of the extension of the light emission in the negative phase provides an estimation of the ion cloud length.

4. Conclusion

We have studied the properties of a surface DBD in air in the conditions that are used in plasma actuators for flow control. In the plasma actuator geometry, one electrode is below the dielectric layer, while the other electrode is above. The discharge takes place in the volume above the surface, between the tip of the top electrode and the dielectric layer surface. Linearly increasing, positive and negative voltages (i.e. with anode or cathode above the dielectric layer, respectively) have been considered in order to simplify the interpretation of the results. The complex chemistry of air has not been considered since the aim of this paper was mainly to get a better insight in the physics of these surface discharges, and not to provide accurate predictions. The conclusions that can be drawn from this work are listed below.

(a) The current waveform in the positive discharge (anode above the surface) consists of high current peaks, associated with the development of a ‘streamer like’ discharges along the surface. Low current, ‘corona like’ discharges takes place between the current pulses. The current pulse frequency is on the order of a few 100 kHz under typical conditions. During this low current phase, a positive ion cloud forms and expands along the surface until breakdown occurs. The expansion length of the positive ion cloud above the surface is limited by breakdown and increases when the slope of the applied voltage increases. It varies from 1 mm to a few millimetres under typical conditions. The EHD force for a positive discharge is important only during the low current phase between the current pulses. The calculated space and time averaged EHD force parallel to the surface per unit length of the electrode is on the order of $0.1\,\text{mN}\,\text{m}^{-1}$ and is not very sensitive to the conditions (for a long enough duration of the discharge). The results in air for the positive discharge are similar to those obtained in pure nitrogen.

(b) The negative discharge (cathode above the surface) in air has different properties. The discharge current is composed of higher frequency (few megahertz) lower amplitude current pulses (amplitude about 10 ten times smaller than in the positive case). A negative space charge forms and expands continuously above the surface during the current pulses (and its expansion is not limited by breakdown). At each current pulse, a plasma forms in the vicinity of the electrode tip and an electron current flows above the surface across the ion cloud, creating more negative ions at the tip of the ion cloud, and charging the dielectric surface below and ahead of the ion cloud. This mechanism is responsible for the negative space charge expansion along the surface. Due to the presence of the negative ion space charge, an important EHD force is also present in the negative discharge above the surface, and is in the same direction as the EHD force generated by the positive discharge. The order of magnitude of the EHD force in the negative discharge can be larger than the force in the positive regime, depending on the conditions. The velocity of the negative cloud expansion above the surface increases linearly with the slope of the applied voltage (like in the positive case), and its value is on the order of a few 100 m s^{-1} (several times smaller than in the positive case for the same conditions). In contrast with the positive case the expansion of the ion cloud is only limited by the duration of the negative phase. For a sinusoidal applied voltage, the maximum expansion length of the negative cloud increases linearly with the voltage amplitude (independently of frequency) and is on the order of 1 cm for a voltage amplitude of 25 kV.

Work is in progress in the following directions:

- systematic parametric study of the EHD force for a sinusoidal voltage waveform,
- sensitivity analysis of the results to different parameters (secondary emission coefficient, ion mobilities, air chemistry),
- systematic study of the accuracy of the numerical scheme,
- coupling of the plasma model with a Navier–Stokes solver to describe the boundary layer modification and
- experimental measurement to confirm the conclusions of the model.

Acknowledgments

The material in this paper is based upon the work supported by the EOARD (European Office of Aerospace Research and Development), under contract no FA8655-06-C-4004.

References

[1] Roth J R 2003 Aerodynamic flow acceleration using paraelectric and peristaltic electrohydrodynamic effects of a one atmosphere uniform glow Discharge *Phys. Plasmas* **10** 2117–26
[2] Moreau E 2007 Airflow control by non-thermal plasma actuators *J. Phys. D: Appl. Phys.* **40** 605–36
[3] Enloe C L, McLaughlin T E, VanDyken R D, Kachner K D, Jumper E J, Corke T C, Post M and Haddad O 2004 Mechanisms and responses of a single dielectric barrier plasma actuator: geometric effects *AIAA J.* **42** 595–604
[4] Pons J, Moreau E and Touchard G 2005 Asymmetric surface dielectric barrier discharge in air at atmospheric pressure: electrical properties and induced airflow characteristics *J. Phys. D: Appl. Phys.* **38** 3635–42
[5] Loeb L B 1965 *Electrical Coronas: Their Basic Physical Mechanisms* (Berkeley, CA: University of California Press)
[6] El-Khabiry S and Colver G M 1997 Drag reduction by a dc corona discharge along an electrically conductive flat plate for small Reynolds number flow *Phys. Fluids* **9** 587–99
[7] Boeuf J P and Pitchford L C 2005 Electrohydrodynamic force and aerodynamic flow acceleration in surface dielectric barrier discharge *J. Appl. Phys.* **97** 103307
[8] Boeuf J P, Lagmich Y, Unfer T, Callegari T and Pitchford L C 2007 Electrohydrodynamic force in dielectric barrier discharge plasma actuators *J. Phys. D: Appl. Phys.* **40** 652–62
[9] Lagmich Y, Callegari T, Unfer T, Pitchford L C and Boeuf J P 2007 Electrohydrodynamic force and scaling laws in surface dielectric barrier discharges *Appl. Phys. Lett.* **90** 051502
[10] BOLSIG+ electron Boltzmann equation solver, http://www.laplace.univ-tlse.fr/spip.php?rubrique273&lang=en
[11] Likhanskii A V, Shneider M N, Macheret S O and Miles R B 2007 *Phys. Plasmas* **14** 073501
[12] Unfer T, Boeuf J P, Rogier F and Thivet F 2007 An asynchronous scheme with local time stepping for multi-scale transport problems: application to gas discharges *J. Comput. Phys.* **227** 898
[13] Takizawa Y, Matsuda A, Kikuchi K, Sasoh A and Abe A 2007 Optical observation of discharge plasma structure in DBD plasma actuator *38th AIAA Plasmadynamics and Lasers Conf. (Miami, FL, 25–28 June 2007)* paper AIAA 2007-4376

JOURNAL OF APPLIED PHYSICS **106**, 023115 (2009)

Contribution of positive and negative ions to the electrohydrodynamic force in a dielectric barrier discharge plasma actuator operating in air

J. P. Boeuf,[1,2,a)] Y. Lagmich,[1,2] and L. C. Pitchford[1,2]
[1]*UPS, INPT, LAPLACE (Laboratoire Plasma et Conversion d'Energie), Université de Toulouse, 118 route de Narbonne, F-31062 Toulouse Cedex 9, France*
[2]*LAPLACE, CNRS, F-31062 Toulouse, France*

(Received 21 April 2009; accepted 24 June 2009; published online 29 July 2009)

We present a parametric study of the electrohydrodynamic force generated by surface dielectric barrier discharge plasma actuators in air for sinusoidal voltage waveforms. The simulation results confirm that momentum is transferred from the charged particles to the neutral species in the same direction during both positive and negative parts of the cycle. The momentum transfer is due to positive ions during the positive part of the cycle (electrode above the dielectric layer is the anode), and to negative ions during the negative part of the cycle. The relative contribution of the positive and negative parts of the cycle depends on the voltage amplitude and frequency. The model predicts that the contribution of negative ions tends to be dominant at low voltage frequencies and high voltage amplitudes. © *2009 American Institute of Physics*. [DOI: 10.1063/1.3183960]

I. INTRODUCTION

Electric discharges along the surface of an airfoil can exert significant forces in the boundary layer of a flow (see, e.g., the review of Ref. 1). One of the possible mechanisms of action of a discharge plasma on a flow is through the electrohydrodynamic (EHD) force associated with the momentum transfer from charged particles to neutral molecules, leading to the well known "ion wind." In the context of boundary layer modification, ion wind can be generated in surface corona discharges or in surface dielectric barrier discharges (surface DBDs or SDBDs). Plasma actuators based on surface DBDs have been considered for aerodynamic applications since the pioneering work of Roth *et al.*[2,3] Surface discharges can generate airflow with velocities less than 10 m/s, while active airflow control with SDBDs has been demonstrated for low subsonic velocities (up to 30 m/s).[1]

Many papers have been devoted to the modeling of the EHD force generated by a SDBD (see, e.g., Refs. 4–9). A clear understanding of the conditions optimizing the force and of the maximum EHD force that can be obtained with surface DBDs is, however, still needed. Although it has been shown by time resolved measurements[10–12] and simulations that both positive and negative ions can contribute to the total EHD force in SDBDs in air and for an asymmetric electrode arrangement, there is no published parametric study of the relative contribution of each type of ions to the total force, as a function of voltage amplitude and frequency.

In previous papers[6,7,9] we considered the simplified case of linearly increasing voltage waveforms for positive and negative discharges. This approach was useful to better understand the physics and to simplify the interpretation of the results. This work has clearly confirmed that the EHD force in surface DBD conditions, such as those of most experiments,[1–3,10–18] is due to momentum transfer from ions to neutral molecules in unipolar regions of the discharge (i.e., regions where a positive or negative, non-neutral ion cloud develops above the dielectric surface). The momentum transfer takes place mainly during the low current phases between high current pulses and the streamers developing along the surface do not contribute significantly to the total EHD force.

In this paper we consider sinusoidal voltage waveforms and study the influence of the voltage amplitude and frequency on the discharge properties and on the generated EHD force.

II. SIMULATION OF SDBDS FOR SINUSOIDAL WAVEFORMS

In this section we briefly recall the principles of the model (Sec. II A), then we show the evolution of the current and charged particle densities in a typical sinusoidal SDBD (Sec. II B) of the EHD force (Sec. II C) and of the surface charge (Sec. II D).

A. Model

The discharge model has been described in previous papers, and we only recall here its main features. Electron and ion (positive and negative) fluid transport equations are solved together with Poisson's equation for the electric field in a two-dimensional (2D), Cartesian geometry.

We consider only one type of positive ion and one type of negative ion with a basic chemistry including ionization, attachment, and recombination.

The continuity equations for electrons, positive, and negative ions are written, respectively, as

$$\frac{\partial n_e}{\partial t} + \vec{\nabla} \cdot \vec{\Gamma}_e = (\alpha - \eta)\|\vec{\Gamma}_e\| - r_{ep} n_e n_p, \tag{1}$$

$$\frac{\partial n_p}{\partial t} + \vec{\nabla} \cdot \vec{\Gamma}_p = \alpha\|\vec{\Gamma}_e\| - r_{ep} n_e n_p - r_{np} n_n n_p, \tag{2}$$

[a)] Electronic mail: jpb@laplace.univ-tlse.fr.

0021-8979/2009/106(2)/023115/9/$25.00

$$\frac{\partial n_n}{\partial t} + \vec{\nabla}\cdot\vec{\Gamma}_n = \eta\|\vec{\Gamma}_e\| - r_{np}n_n n_p, \tag{3}$$

where n_e, n_p, n_n are the electron, positive ion, and negative ion densities, $\vec{\Gamma}_e, \vec{\Gamma}_p, \vec{\Gamma}_n$ the charged particle fluxes, α and η the ionization and attachment coefficients in air, and r_{ep} and r_{np} the electron-ion and ion-ion recombination coefficients.

In the drift-diffusion approximation, the charged particle momentum equations are equivalent to writing that the charged particle fluxes are the sum of a drift term and a diffusion term as in

$$\vec{\Gamma}_e = \mu_e\left(-n_e\vec{E} - \frac{k_BT_e}{e}\vec{\nabla}n_e\right), \tag{4}$$

$$\vec{\Gamma}_p = \mu_p\left(n_p\vec{E} - \frac{k_BT_p}{e}\vec{\nabla}n_p\right), \tag{5}$$

$$\vec{\Gamma}_n = \mu_n\left(-n_n\vec{E} - \frac{k_BT_n}{e}\vec{\nabla}n_n\right), \tag{6}$$

where (μ_e, μ_p, μ_n) and (T_e, T_p, T_n) are the charged particles' mobility and temperature, respectively, and k_B is the Boltzmann constant. The data for air (ionization, attachment, and mobility as a function of reduced electric field and recombination coefficients) are the same as those of Ref. 9. The charged particle temperatures in Eqs. (4)–(6) are supposed to be constant and equal to 1 eV for electrons and to ambient temperature for ions.

Equations (1)–(6) above must be coupled to Poisson's equation for the electric field,

$$\vec{\nabla}\cdot(\varepsilon_r\vec{E}) = \frac{e}{\varepsilon_0}(n_p - n_e - n_n) + \frac{\sigma}{\varepsilon_0}\delta_S, \tag{7}$$

where ε_0 is the vacuum permittivity, ε_r is the relative permittivity (equal to 1 in the discharge volume above the dielectric surface and supposed to be equal to 5 inside the dielectric layer), and $\sigma\delta_S$ represents the contribution of the charges deposited by the discharge on the dielectric surface. These charges are obtained by time integrating charged particle fluxes to the surface. Equation (7) is solved for the electric potential V $(\vec{E} = -\vec{\nabla}V)$. The boundary conditions for Poisson's equation are zero field perpendicular to the walls of the simulation domain and potential difference between the electrodes of the form $V = V_0\cos(\omega t)$.

The boundary condition for the charged particle densities on the walls of the simulation domain is zero density gradients, i.e., no flux (since the perpendicular field is zero), which is equivalent to a symmetry condition.

Finally, the dielectric surface is supposed to emit secondary electrons under ion bombardment, with a secondary emission coefficient γ equal to 0.05,

$$\vec{\Gamma}_e\cdot\vec{u}_\perp = -\gamma\vec{\Gamma}_p\cdot\vec{u}_\perp. \tag{8}$$

The physical model above is typical of atmospheric discharge models and is similar to the model of Likanskii *et al.*,[4] in the context of DBD actuators.

All the results presented in this paper have been obtained with a $(8\times 4\ \mathrm{mm}^2)$ simulation domain shown in Fig. 1. The grid spacing is 20 μm, i.e., a uniform mesh of 400 × 200 has been used. In these conditions the computation time on a personal computer (PC) workstation is on the order of 10 CPU hours for 100 μs (this is only an order of magnitude, and the CPU time actually depends on the voltage amplitude and frequency), i.e., it takes a few days of CPU time to simulate several cycles at a voltage frequency of 5 kHz, for example. This is relatively fast due to the semi-implicit time integration of the transport-Poisson equations and to the fact that the integration time step for the electron and ion transport equations can be larger than the Courant Friedrich Lewy time (first order accuracy in time). The question of the accuracy of the simulation has been discussed in Ref. 6, and results from the model presented here compare satisfactorily with results from a more accurate numerical model.[8,19] More systematic comparisons will be discussed in details in a forthcoming paper.

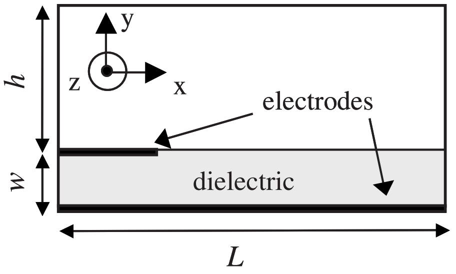

FIG. 1. Simulation domain: $L=8$ mm, $w=1$ mm, and $h=3$ mm.

Results are presented below for sinusoidal voltages across the electrodes, with amplitudes and frequencies in the ranges of 5–30 kV and 1–10 kHz, respectively. In the rest of the paper we call positive (or positive discharge) the part of the cycle when the electrode above the dielectric surface plays the role of an anode, and negative (or negative discharge) the part of the cycle when the top electrode is a cathode.

B. Evolution of a typical discharge

We present in this section the space and time evolution of a typical SDBD in air at atmospheric pressure. Since the time evolution of a SDBD can be quite complex, most of the results (time evolution of the charged particle densities and EHD force) will be shown as a function of time and position along the dielectric surface and integrated in the direction perpendicular to the dielectric surface. This allows a simpler visualization of the time variations of those quantities and provides a clearer understanding of the mechanisms. This more concise representation contains the important features and is sufficient for our purpose. The detailed time evolution of the 2D quantities was described in previous papers in the case of linearly increasing voltages (see, e.g., Refs. 6–9).

Figure 2 shows the time evolution of the calculated current for a voltage waveform of 15 kV amplitude and 10 kHz frequency. Figures 3–5 show the calculated time variations of the electron, positive ion, and negative ion number densities along the dielectric surface and integrated along the direction perpendicular to the surface (therefore given in units of cm^{-2}), as a function of time, in the same conditions.

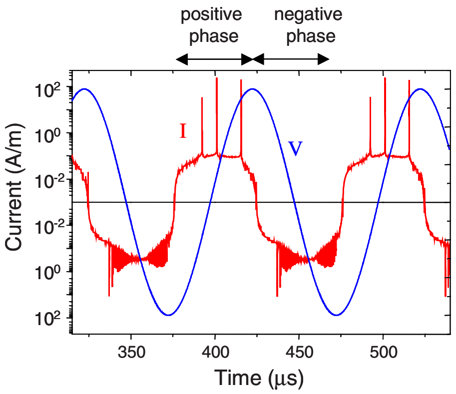

FIG. 2. (Color online) Time variations of the calculated current and applied voltage for a 15 kV amplitude, 10 kHz frequency voltage waveform. The electrode above the dielectric layer plays the role of an anode during the "positive phase" (or positive part of the cycle) and plays the role of a cathode during the " negative phase."

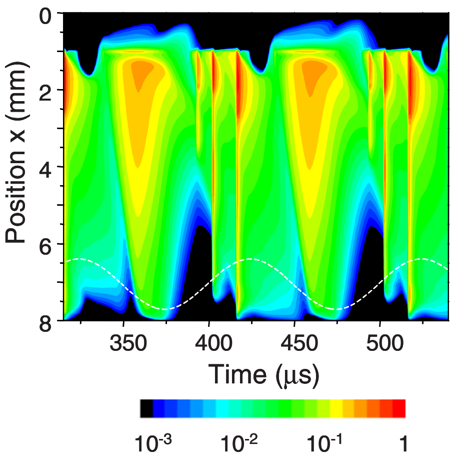

FIG. 4. (Color online) Time evolution of the positive ion density along the x direction and integrated in the y direction in units of 10^{10} cm^{-2} for the conditions of Fig. 2 (10 kHz, 15 kV). The dashed line indicates the time evolution of the applied voltage on the top electrode.

We see on the calculated current in Fig. 2 that the positive and negative parts of the cycle are quite different, in agreement with the calculations for positive and negative ramp voltages described in previous papers.[9] A few high current pulses separated by low current phases are apparent during the positive part of the cycle (Fig. 2). These current pulses are separated by several 10 s of microseconds. The negative part of the cycle is composed of a much larger number of current pulses (frequency in the megahertz range) of smaller amplitudes. The calculated current waveform and the asymmetry between positive and negative parts of the cycle predicted by the model are in excellent qualitative agreement with the experiments (see, e.g., Refs. 13–18).

The time variations of the charged particle densities along the surface and integrated in the direction perpendicular to the surface (Fig. 3–5) clearly show the streamer phases associated with the high current pulses in the positive regime and the glow corona phase during the negative part of the cycle. The high frequency oscillations in the negative phase are not apparent on Figs. 3–5 because the time resolution of the plotted densities is larger than the period of these oscillations (see Ref. 9 for more details). A non-neutral, negative ion cloud develops along the surface during the negative phase. The development of this ion cloud is consistent with the results obtained with linearly varying negative voltages. Positive ions are also formed above the dielectric surface during the negative phase, but the positive ion density is smaller than the negative ion density, especially in the front of the ion cloud (compare Figs. 4 and 5), and the space charge is negative. The existence of this negative space charge is possible because the ion densities in the cloud are small enough that charge separation by the applied field is possible in that region (the plasma is not quasineutral). The electric field in that region is, as mentioned in Ref. 9, slightly below the value for which ionization balances attachment. Note that the propagation velocity of the negative ion cloud along the surface can be estimated to be of a few 10^4 cm/s in these conditions.

During the positive phase a positive ion cloud develops over the surface, but its development is interrupted by streamer breakdown and restarts from zero after each

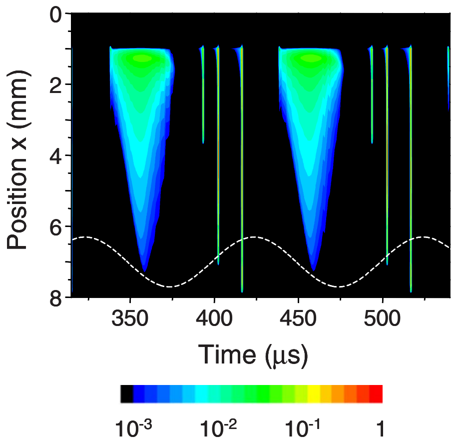

FIG. 3. (Color online) Time evolution of the electron density along the x direction and integrated in the y direction (see Fig. 1) and therefore given in units of 10^{10} cm^{-2} for the conditions of Fig. 2 (10 kHz, 15 kV). The dashed line indicates the time evolution of the applied voltage on the top electrode (the electrode below the dielectric layer being grounded).

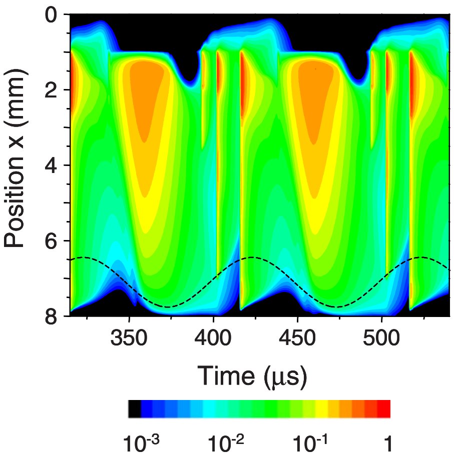

FIG. 5. (Color online) Time evolution of the negative ion density along the x direction and integrated in the y direction in units of 10^{10} cm^{-2} for the conditions of Fig. 2 (10 kHz, 15 kV). The dashed line indicates the time evolution of the applied voltage on the top electrode.

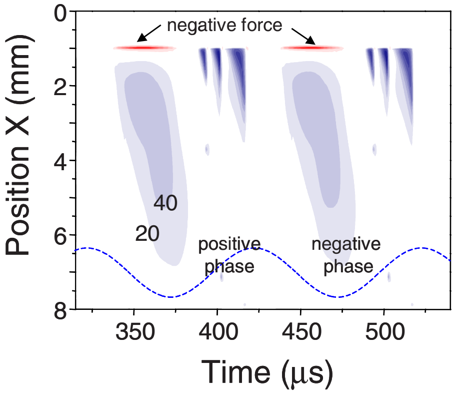

FIG. 6. (Color online) Time evolution of the EHD force per unit surface (in $\mathrm{N/m^2}$) parallel to the dielectric surface (force per unit volume integrated in the y direction) for the conditions of Fig. 2 (10 kHz, 15 kV). The force is mainly directed in the positive x direction (blue color, from 0 to 200 $\mathrm{N/m^2}$, contours separated by 20 $\mathrm{N/m^2}$), i.e., away from the top electrode, except near the tip of the top electrode where it is directed toward the electrode (red color, maximum of −500 $\mathrm{N/m^2}$). The dashed line indicates the time evolution of the applied voltage on the top electrode.

streamer pulse. This is very different from the negative phase where the negative ion space charge is continuous and is not strongly perturbed by the high frequency current oscillations.

It is interesting to note in Figs. 3–5 that the length of the streamer channel along the dielectric surface increases from the first to the third high current pulses in the positive regime. The first streamer extends about 3 mm along the dielectric surface, the second streamer length is about 6 mm, while the third one reaches the end of the simulation domain, i.e., a length of 7 mm or larger. This is qualitatively consistent with the experiments of Allegraud *et al.*[20] who measured the streamer extension as a function of time for a lower frequency (50 Hz) SDBD and showed that the streamer length increases with time during the voltage rise in the positive phase.

C. EHD force

The instantaneous EHD force per unit volume is obtained, at any time from the simulation by[5]

$$\overrightarrow{F_{\mathrm{EHD}}} = e(n_e - n_p - n_n)\vec{E} - k_B T_p \vec{\nabla} n_p - k_B T_e \vec{\nabla} n_e - k_B T_n \vec{\nabla} n_n. \tag{9}$$

The component of the EHD force parallel to the surface and integrated along the direction perpendicular to the surface is displayed in Fig. 6 for the conditions of Figs. 2–5. We see that (1) the EHD force along the surface has the same direction during the positive and negative phases of the sinusoidal cycle, i.e., away from the top electrode, (2) there is a large negative force (directed toward the top electrode) that is localized in a very small region next to the top electrode (positive ion sheath) during the negative part of the cycle, (3) the EHD force during the negative and positive phases of the cycle have very different spatial distributions: the force due to negative ions in the negative phase is distributed rather smoothly and uniformly, over a length of about 5 mm along the dielectric surface, while the force due to positive ions, in the positive phase of the cycle, is distributed nonuniformly, closer to the top electrode; also there is no force during the high current pulses since, as discussed in previous papers,[5,6,8] the EHD force is quasizero in a quasineutral plasma (the channel of the streamers). The force that can be seen during the positive phase (seen as three successive maxima on Fig. 6) corresponds to the development of the positive ion space charge before each streamer pulse (during which the force goes to zero).

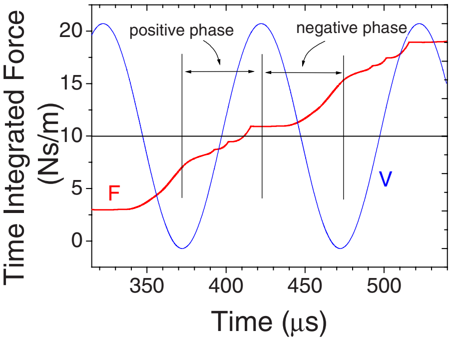

FIG. 7. (Color online) Time integrated total (integrated over the simulation domain) force parallel to the surface, in the conditions of Figs. 2–6 (10 kHz, 15 kV).

The EHD force of Fig. 6 can be integrated along x and up to time t and displayed as a function of time. This time integrated force is represented in Fig. 7 for the conditions of Figs. 2–6.

We see in Fig. 7 that, in these conditions (10 kHz, 15 kV), the increase in the EHD force during the negative part of the cycle is slightly larger than during the positive part of the cycle. We find that the relative contribution of the positive part of the cycle (positive ions) and the negative part (negative ions) to the total EHD force during a voltage cycle strongly depends on the voltage amplitude and frequency. At higher voltage frequencies and lower voltage amplitudes, the EHD force is larger during the positive part of the cycle (dominant contribution of positive ions), while at lower voltage frequencies and larger voltage amplitudes, the EHD force is larger during the negative part of the cycle (dominant contribution of negative ions). This is further discussed below.

The effect of voltage amplitude on the space and time distribution of the EHD force for a given voltage frequency is illustrated in Figs. 8(b) and 9(b). The corresponding voltage and current waveforms are shown in Figs. 8(a) and 9(a). The EHD force is integrated along the direction perpendicular to the surface and is displayed as a function of position along the surface and time.

Figure 8 shows the EHD force for a 5 kHz frequency and 10 kV voltage amplitude. We see that in that case, the force is relatively small during the negative part of the cycle. The spatial extension of the force is also limited to about 3 mm away from the top electrode. The EHD force during the positive part of the cycle is larger but its extension is also limited to about 3 mm. Note that under these conditions, because of the low voltage and relatively low frequency (i.e., low voltage increase rate), there is no streamer formation during the positive part of the cycle, and the current during

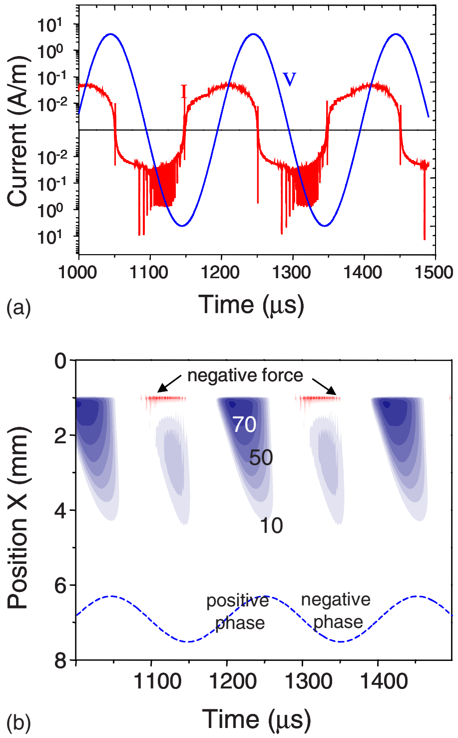

FIG. 8. (Color online) (a) Calculated current for a sinusoidal voltage of amplitude 10 kV at a frequency of 5 kHz (also plotted). (b) Time evolution of the EHD force per unit surface (in $\mathrm{N/m^2}$) parallel to the dielectric surface (force per unit volume integrated in the y direction) for the geometry of Fig. 1 with a sinusoidal voltage of amplitude of 10 kV at a frequency of 5 kHz (a). The force is mainly directed in the positive x direction (blue color, from 0 to 100 $\mathrm{N/m^2}$, contours separated by 10 $\mathrm{N/m^2}$), i.e., away from the top electrode, except near the tip of the top electrode where it is directed toward the electrode (red color, maximum of -100 $\mathrm{N/m^2}$). The dashed line indicates the time evolution of the applied voltage on the top electrode.

that phase is only a corona current leading to an ion cloud formation above the surface and to the corresponding EHD force.

Figure 9 displays the EHD force for the same voltage frequency, 5 kHz, but for a larger voltage amplitude, 25 kV. The EHD force is now much larger during the negative part of the cycle. We also see that four streamers form during the positive part of the cycle and that the force is more intense but distributed on a much smaller region in the positive part of the cycle. The development of the EHD force is clearly perturbed by the streamers, is equal to zero during streamer formation, and restarts from zero after each streamer development.

Note in Figs. 8 and 9 the large negative force (directed toward the top electrode) in a very small region next to the top electrode. This force is, as in Fig. 6 above, due to the positive ion sheath close to the top electrode in the negative regime.

D. Surface charge and potential

The time variations of the surface charge along the dielectric surface are shown in Fig. 10 for the conditions of Fig. 9 (5 kHz, 25 kV). The current waveforms are also shown on these figures for clarity.

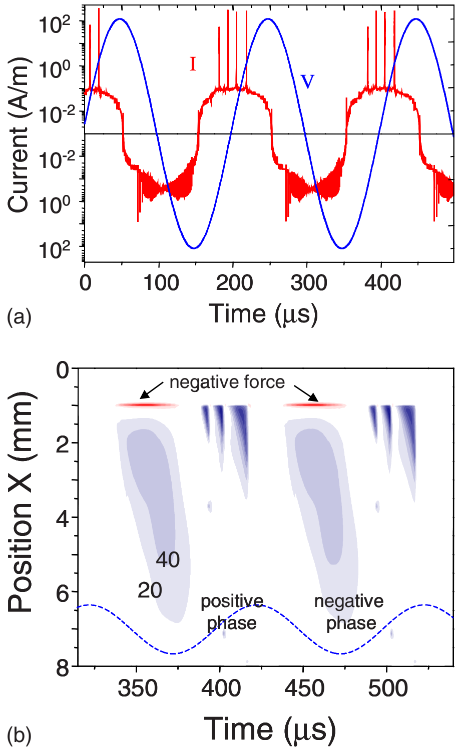

FIG. 9. (Color online) (a) Calculated current for a sinusoidal voltage of amplitude of 25 kV at a frequency of 5 kHz (also plotted). (b) Time evolution of the EHD force parallel to the dielectric surface and integrated in the y direction for the geometry of Fig. 1 with a sinusoidal voltage of amplitude 25 kV at a frequency of 5 kHz (a). The force is mainly directed in the positive x direction (blue color, from 0 to 200 $\mathrm{N/m^2}$, contours separated by 20 $\mathrm{N/m^2}$), i.e., away from the top electrode, except near the tip of the top electrode where it is directed toward the electrode (red color, maximum of -500 $\mathrm{N/m^2}$). The dashed line indicates the time evolution of the applied voltage on the top electrode.

We see that the charge increases smoothly during the negative phase. As we discussed in previous papers,[9] the charge during the negative phase is due mainly to electrons which extend further and further away from the top electrode at each high frequency pulse. The high frequency pulses are

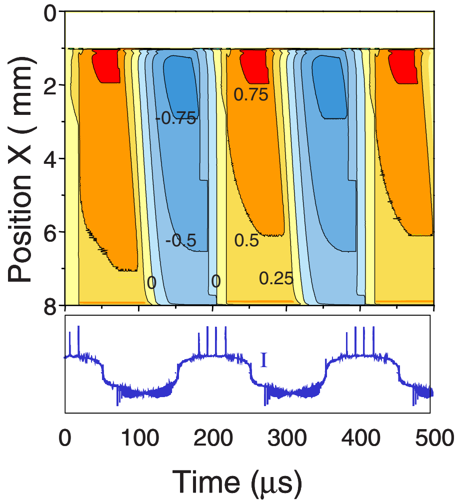

FIG. 10. (Color online) Contours of constant surface charge density (in units of 10^{-7} $\mathrm{C/m^2}$) on the dielectric surface as a function of time for the conditions of Fig. 9 (5 kHz, 25 kV). The current waveform is shown below the surface charge.

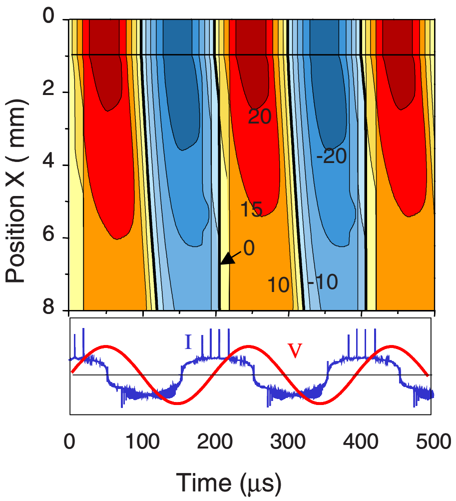

FIG. 11. (Color online) Contours of constant potential (kV) along the surface as a function of time for the conditions of Fig. 9 (5 kHz, 25 kV). The current and voltage waveforms are also shown below the surface potential.

not seen in the figure because the time resolution of the figure is 1 μs and the high frequency pulses of the negative regime are in the megahertz range. The charging during the positive part of the cycle is not as smooth, and we see on Fig. 10 that at each streamer pulse (see the current waveform below the surface charge plot), positive charges are abruptly deposited on the surface (discontinuity in the slope of the surface charge as a function of time).

We also see on this figure that the streamer length increases with time during a positive discharge.

Figure 11 shows the time variations of the potential distribution along the surface, together with the voltage and current waveforms. The streamers are also apparent on the potential distribution since the surface potential below the plasma filament generated by a streamer becomes almost instantaneously equal to the top electrode potential (the high current pulses are very short on the time scale of the figure, and the potential drop along the filament is relatively small).

III. PARAMETRIC STUDY

We have performed systematic calculations of the EHD force parallel to the surface, integrated in the simulation domain, and averaged in time, for voltage frequencies between 1 and 10 kHz, and voltage amplitudes between 4 and 30 kV.

A. EHD force

The contributions of the positive and negative parts of the cycle to the total EHD force parallel to the surface are represented in Fig. 12 as a function of voltage amplitude, and for different voltage frequencies. The force is integrated over the simulation domain, averaged in time, and given per unit length of electrode (since the model is 2D Cartesain). The total force parallel to the surface is represented in Fig. 13 as a function of voltage amplitude and frequency.

We see that, as mentioned above, the contribution of positive ions (positive phase) tends to be larger at higher

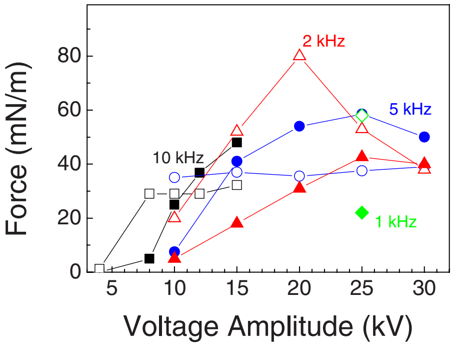

FIG. 12. (Color online) Calculated EHD force parallel to the surface, integrated over the simulation domain, and averaged in time, as a function of voltage amplitude, and for different voltage frequencies. The contributions of the positive (open symbols) and the negative (full symbols) part of the cycle (see Fig. 7) to the total force are represented separately. The EHD force is given per unit length of the electrode in the direction perpendicular to the simulation domain.

frequencies and lower voltage amplitudes while the contribution of negative ions is larger at lower frequencies and larger voltages.

Note, again, that the space distributions of the EHD forces are very different for positive and negative ions (see above), so that the same force magnitude, in Fig. 12, during positive or negative regimes may not have the same aerodynamic effect.

The maximum total force displayed in Fig. 13 is around 100 mN/m. Two measurements from Abe *et al.*[17] for 6 and 10 kV amplitude voltage sinusoidal waveforms at 5 kHz are also shown for comparisons (taken from Fig. 8 of Ref. 17, the force per unit length being deduced by dividing the measured total force by the electrode length). The calculated force is about twice larger than the measured force. The calculated EHD force is therefore on the same order as the measured force and this can be considered as a very encouraging result considering the complexity of the momentum transfer from the discharge to the neutral gas, the relative simplicity of the model, and the difficulty of the measurements. The papers by Enloe *et al.*[13] and by Baughn *et al.*[18] show measurements of the EHD force that are consistent with those of Abe *et al.*, i.e., on the order of 10–20 mN/m for voltage amplitudes around 10 kV and frequency around 10 kHz.

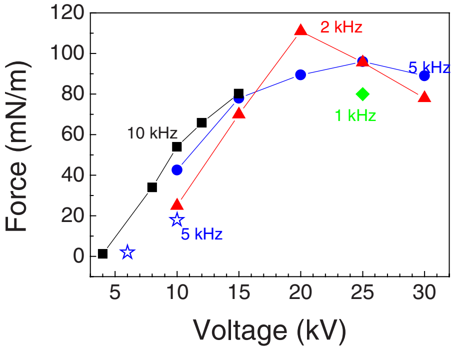

FIG. 13. (Color online) Calculated total EHD force parallel to the surface, integrated over the simulation domain, and averaged in time (sum of the positive and negative contributions of Fig. 12). The star symbols correspond to the measurements of Abe *et al.* (Ref. 17) at 5 kHz.

The model results of Fig. 13 also show that the force can increase significantly when the applied voltage amplitude is larger than 10 kV. We shall see in the subsection below that it is possible to increase the voltage to 20 or 30 kV while keeping the dissipated power in reasonable limits, if one operates at lower voltage frequencies.

We see on Fig. 13 a saturation and a decrease in the force for high enough applied voltages. This saturation is reached at higher voltages for lower frequencies. The limited length of the simulation domain may be partly responsible for this saturation. Note that the results of Figs. 12 and 13 at low frequencies (2 kHz) and high voltages should be regarded as preliminary since they were obtained by simulating no more than 2 cycles (about 4 days of CPU time on a PC workstation) and convergence to a harmonic steady state can take several cycles. Nevertheless, the trend predicted by the model is that although the EHD force clearly increases with frequency at low voltage amplitudes, this is no longer the case at higher voltage amplitudes. This is to be compared with the experimental results of Dai and Roth[21] (see Fig. 16c of Ref. 21), which show that the ion wind velocity increases with frequency for rms voltages below about 7 kV and decreases with frequency above this voltage.

B. Power dissipation

The averaged power dissipated for each case of Figs. 12 and 13 has been calculated and is displayed in Fig. 14(a) as a function of voltage amplitude and for different frequencies. Again, the results at high voltage and low frequency (2 kHz) need to be confirmed by calculations over a larger number of cycles.

The EHD force of Fig. 13 is replotted on Fig. 14(b) for comparison with the dissipated power. Finally, the force per unit power is plotted as a function of voltage amplitude and frequency in Fig. 14(c). The efficiency (force generated for a given electric power) is larger at lower voltages because there are less high current pulses (streamers) in these conditions, but the force is small at low voltages and increases with voltage. It seems from Fig. 14(c) that larger EHD force and better efficiency are obtained at lower frequency and high voltage amplitudes. This corresponds to regimes where the contribution of negative ions to the EHD force is dominant. The best way to obtain a large EHD force with a reasonable power consumption is therefore to operate at high voltage amplitude and low frequency. This is consistent with the experiments of Moreau (see, e.g., Ref. 1).

Finally, note that some of the curves presented in Figs. 12–14 are not perfectly smooth (in spite of the fact that the model is fluid and there is no statistical fluctuations). This is because the number of current pulses in this 2D simulation is small (especially in the positive regime). For example, when increasing the voltage at a constant frequency, the number of streamer pulses during the positive phase increases discretely. The dissipated power increases abruptly as a function a frequency at each increase in the number of streamers. However, the calculations of Fig. 14 were not performed with small voltage increments and the discontinuities due to the appearance of new streamers do not appear clearly. This explains the “unnatural” change in slope that can be observed, for example, on Fig. 14(a). This would not happen in a real experiment because of the statistical distribution of streamers along the electrode.

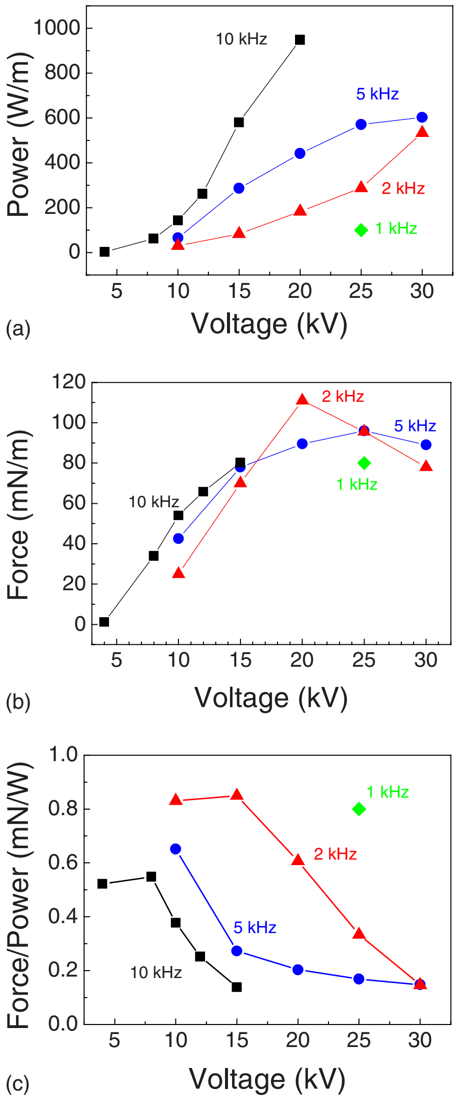

FIG. 14. (Color online) (a) Power dissipated per unit length of the electrode, (b) total EHD force, and (c) force per unit power as a function of voltage amplitudes and for different voltage frequencies.

IV. SUMMARY AND CONCLUSION

We have presented simulations of a SDBD plasma actuator for sinusoidal voltages of frequency and amplitude in the 1–10 kHz, and 4–30 kV ranges, respectively.

The results confirm previous calculations performed with linearly increasing positive or negative voltages.

The EHD force is directed away from the top electrode both in the positive and negative parts of the sinusoidal voltage. The momentum transfer leading to the EHD force is due to positive ions during the positive phase and to negative ions in the negative phase of the cycle. The relative contributions of the positive and negative ions to the total EHD force depend on the voltage amplitude and frequency. At high frequencies and low voltage amplitude, the contributions of positive ions are dominant, while the contribution of negative ions to the total EHD force is dominant at low frequencies and high voltage amplitudes.

The space distribution of the force is different for positive and negative ions. In the positive regime, the EHD force due to positive ions tends to be distributed closer to the top electrode. This is because a new positive ion cloud must start from the top electrode after each streamer. During the negative phase, the negative ion cloud develops continuously and its spatial extension tends to be larger. The EHD force during the negative phase is therefore more spread out along the dielectric surface. The extension of the force along the surface in the negative phase increases when the frequency decreases and the voltage amplitude increases. The differences in the space and time distributions of the EHD force during the positive and negative phases may lead to different aerodynamic effects even for the same total force (integrated in space). Finally, a large negative EHD force (i.e., directed toward the top electrode) distributed in a small region at the tip of the top electrode always exists during the negative phase. This force is associated with the positive ion sheath next to the top electrode in that regime. When spatially integrated, this negative force is negligible with respect to the total positive force in the negative ion cloud, but it may also have some effect on the flow.

The force obtained in the simulation is on the order of several 10 mN/m (with a maximum of 100 mN/m) for a simulation domain of 8 mm length, increases with voltage amplitude, and is more efficiently produced at lower frequencies.

The discharge efficiency to produce the EHD force is less than 1 mN/W. For a given frequency, the efficiency in the production of the EHD force strongly decreases with voltage amplitude above a given voltage (because more energy is spent in streamer discharges at higher voltage). The calculated efficiency at the maximum force is on the order of 0.2 mN/W, and this is consistent with the measurements.

From the results presented here and in previous papers, and from the understanding of the SDBD provided by the model, we can anticipate what could be the effect of voltage waveforms other than sinusoidal (i.e., positive or negative sawtooth,[13] etc.). For example, we can expect that negative sawtooth waveforms at low frequency and large voltage amplitudes could be efficient because they would tend to optimize the contribution of negative ions. We call negative sawtooth a voltage waveform where the top electrode voltage decreases on a long time scale while it goes back to zero on a short time scale. However, strong streamers will of course form when the voltage goes back to zero (positive discharge) after the negative ramp voltage, and this can affect the discharge efficiency in producing the EHD force.

The simulation results presented here are in excellent qualitative agreement with the experiments, i.e., many of the features and trends observed in the experiments can be reproduced by the model. This means that the model includes the essential physics, at least for the range of conditions considered in this paper. One of the important results is the confirmation that negative ions are responsible for the transfer of momentum to the neutral molecules during the negative part of the cycle, while positive ions transfer momentum during the positive part. The asymmetry between the space and time distributions of the EHD force due to positive and to negative ions, and the different relative contributions of positive and negative ions depending on the voltage amplitude and frequency are also new and important results from the model.

On a more quantitative point of view, the predicted EHD force per unit length and force per unit power are consistent with experiments although there is no published systematic measurements of these parameters as a function of voltage amplitude and frequency over a large range of conditions (such measurements would be extremely useful for model validation). More experimental study on the time modulation of the EHD force and ion wind velocity would also be extremely useful. Published experimental results[12,1] have shown the time modulation of the EHD force or of the generated ion wind, but no systematic parametric study with voltage and frequency has been reported. Another point that needs clarification is the apparent saturation of the EHD force with voltage for high enough voltage amplitudes, at a given frequency.

The mechanisms leading to momentum transfer from charged particles to neutral species in surface DBDs are now relatively well understood. Further work needs to do be done to better understand other possible effects of a surface discharge on a flow, i.e., effects that could be due to mechanisms other than momentum transfer and ion wind. Experiments showing that filamentary surface discharges generated by high voltage, nanosecond pulses can affect a flow although they do not generate any ion wind have been reported recently.[22] Simulations of the plasma-flow interaction under these conditions will be presented in a forthcoming paper.[23]

ACKOWLEDGEMENTS

The material in this article is based upon work supported by EOARD (European Office of Aerospace Research and Development), under Contract No. FA8655-06-C-4004.

[1] E. Moreau, J. Phys. D **40**, 605 (2007).
[2] J. R. Roth, D. M. Sherman, and S. P. Wilkinson, AIAA J. **38**, 1166 (2000).
[3] J. R. Roth, Phys. Plasmas **10**, 2117 (2003).
[4] A. V. Likhanskii, M. N. Shneider, S. O. Macheret, and R. B. Miles, Phys. Plasmas **14**, 073501 (2007); J. Appl. Phys. **103**, 053305 (2008).
[5] J. P. Boeuf and L. C. Pitchford, J. Appl. Phys. **97**, 103307 (2005).
[6] J. P. Boeuf, Y. Lagmich, Th. Unfer, Th. Callegari, and L. C. Pitchford, J. Phys. D: Appl. Phys. **40**, 652 (2007).
[7] Y. Lagmich, Th. Callegari, Th. Unfer, L. C. Pitchford, and J. P. Boeuf, Appl. Phys. Lett. **90**, 051502 (2007).
[8] T. Unfer, J. P. Boeuf, F. Rogier, and F. Thivet, J. Comput. Phys. **227**, 898 (2007).
[9] Y. Lagmich, T. Callegari, L. Pitchford, and J. P. Boeuf, J. Phys. D: Appl. Phys. **41**, 095205 (2008).
[10] M. Forte and J. Jolibois, J. Pons, E. Moreau, G. Touchard, and M. Cazalens, Exp. Fluids **43**, 917 (2007).
[11] N. Takeuchi, K. Yasuoka, and S. Ishii, IEEE Trans. Plasma Sci. **35**, 1704 (2007).
[12] C. L. Enloe, M. G. McHarg, and T. E. McLaughlin, J. Appl. Phys. **103**, 073302 (2008).
[13] C. L. Enloe, T. E. McLaughlin, D. R. VanDyken, and K. D. Kachner, AIAA J. **42**, 589 (2004).
[14] C. O. Porter, T. E. McLaughlin, C. L. Enloe, G. I. Font, J. Roney, and J. W. Baughn, 45th AIAA Aerospace Sciences Meeting and Exhibit, 8–11 January 2007, Reno Nevada (unpublished), AIAA Paper No. 2007–786.

[15] C. L. Enloe, T. E. McLaughlin, R. D. Van Dyken, K. D. Kachner, E. J. Jumper, and T. C. Corke, Proceedings of the 41st AIAA Aerospace Sciences Meeting and Exhibit, Reno, Nevada, 6–9 January 2003 (unpublished), AIAA Paper No. 2003–1021.
[16] J. Pons, E. Moreau, and G. Touchard, J. Phys. D: Appl. Phys. **38**, 3635 (2005).
[17] T. Abe, Y. Takizawa, and S. Sato, Proceedings of the 45th AIAA Aerospace Sciences Meeting and Exhibit, Reno, Nevada, 8–11 January 2007 (unpublished), AIAA Paper No. 2007–187.
[18] J. W. Baughn, C. O. Porter, B. L. Peterson, T. E. McLaughlin, C. L. Enloe, G. I. Font, and C. Baird, Proceedings of the 44th AIAA Aerospace Sciences Meeting and Exhibit, Reno, Nevada, 9–12 January 2006 (unpublished), AIAA Paper No. 2006–168.
[19] T. Unfer, J.-P. Boeuf, F. Rogier, and F. Thivet, Proceedings of the 46th AIAA Aerospace Sciences Meeting and Exhibit, Reno, Nevada, 7–10 January 2008 (unpublished), AIAA Paper No. 2008–1375.
[20] K. Allegraud, O. Guaitella, and A. Rousseau, J. Phys. D: Appl. Phys. **40**, 7698 (2007).
[21] J. R. Roth and X. Dai, Proceedings of the 44th AIAA Aerospace Sciences Meeting and Exhibit, Reno, Nevada, 9–12 January 2006 (unpublished), AIAA paper 2006–1203.
[22] A. Starikovskii, D. Roupassov, A. Nikipelov and M. Nudnova, Plasma Source Sci. Technol. **18**, 034015 (2009).
[23] T. Unfer and J.P. Boeuf, J. Phys D: Appl. Phys. (submitted).

IOP Publishing | Journal of Physics D: Applied Physics
J. Phys. D: Appl. Phys. **42** (2009) 194017 (12pp) | doi:10.1088/0022-3727/42/19/194017

Modelling of a nanosecond surface discharge actuator

T Unfer and J P Boeuf

Université de Toulouse; UPS, INPT; LAPLACE (Laboratoire Plasma et Conversion d'Energie);
118 route de Narbonne, F-31062 Toulouse cedex 9, France
and
CNRS; LAPLACE; F-31062 Toulouse, France

Received 24 May 2009, in final form 5 July 2009
Published 18 September 2009
Online at stacks.iop.org/JPhysD/42/194017

Abstract
Surface dielectric barrier discharges (SDBDs) can modify the boundary layer of a flow and are studied as a possible means to control the flow over an airfoil. In SDBDs driven by sinusoidal voltages in the 1–10 kHz range, momentum is transferred from ions to the neutral gas, as in a corona discharge (ion wind), and the resulting electrohydrodynamic force can generate a flow of several $\mathrm{m\,s^{-1}}$ in the boundary layer along the surface. In this paper we are interested in a different regime of SDBDs where nanosecond voltage pulses are applied between the electrodes. Recent experiments by the group of Starikovskii have demonstrated that such discharges are able to modify a flow although no significant ion wind can be detected.

A two-dimensional self-consistent numerical model of the discharge and gas dynamics in conditions similar to those of these experiments has been developed. The model couples fluid discharge equations with compressible Navier–Stokes equations including momentum and thermal transfer from the plasma to the neutral gas. This is a difficult multi-scale problem and special care has been taken to accurately solve the equations over a large simulation domain and at a relatively low computational cost. The results show that under the conditions of the simulated experiments, fast gas heating takes place in the boundary layer, leading to the generation of a 'micro' shock wave, in agreement with the experiments.

(Some figures in this article are in colour only in the electronic version)

1. Introduction

Significant research efforts have been devoted in recent years to demonstrating the possibility of using non-thermal plasmas as actuators for flow control. Surface corona discharges and surface dielectric barrier discharges (SDBDs) have been extensively studied for this application. In the case of surface corona discharges [1], two parallel wires are placed on a dielectric surface, a few centimetres apart. If a dc voltage of several tens of kilovolts is applied between the electrodes, the ion wind generated by the corona discharge can reattach a flow of a few $\mathrm{m\,s^{-1}}$ [1]. In a SDBD, one electrode ('top electrode', or 'exposed electrode') is placed above the dielectric surface while the other electrode is placed below the dielectric surface [2–5]. In this asymmetric configuration an ion wind is generated from the tip of the top electrode, along the dielectric surface above the other electrode. With sinusoidal voltage amplitudes from a few kV to 20 or 30 kV and frequencies in the 1–10 kHz range, SDBDs can also generate a flow of a few $\mathrm{m\,s^{-1}}$ (up to $10\,\mathrm{m\,s^{-1}}$). The advantage of SDBDs over surface corona discharges is that the dielectric layer between the electrodes in the dielectric barrier discharge configuration limits the current and prevents the transition to an arc (we are interested here in a well-controlled, low power, non-equilibrium discharge regime).

A recent review of surface discharges for flow control can be found in [6]. A large number of experimental [2–7] and modelling papers [8–15] describing the plasma/flow interaction in the sinusoidal regime have been published in the last few years.

The recent experiments of Starikovskii and co-workers [16–18] introduced a different type of SDBD using a nanosecond voltage pulse generator (the voltage pulse can be several tens of kilovolts with rise and decay time on the order of or less than 10 ns). Under these conditions, the corona regime that is responsible for the ion wind in sinusoidal regimes (see, e.g. [14, 15]) is no longer present and the main discharge regime is a streamer regime. This was confirmed by the quasi-zero ion wind measured by Starikovskii *et al*. However, the authors of [16–18] showed that this kind of discharge was able to affect the aerodynamic properties of a flow along the surface, and that a detached flow could be reattached when a nanosecond voltage pulse was applied between the electrodes at a repetition rate of a few kilohertz (for spanwise as well as streamwise configurations of the DBD actuators with respect to the flow direction). One important conclusion of the experiments of Starikovskii *et al* [16–18] is that a large part of the plasma energy is released into gas heating in a short time (less than 1 μs), leading to the formation of a micro shock wave.

The purpose of this work is to better understand and quantify the gas dynamics generated by a nanosecond surface discharge under conditions similar to Starikovskii *et al* using a self-consistent model of the discharge and generated gas dynamics. A 2D fluid model of the surface discharge has been coupled with a compressible Navier–Stokes description of the gas dynamics. This is a multi-scale problem in space and time since timescales from picoseconds to tens of microseconds and dimensions from a few micrometres to several centimetres must be resolved. A numerical method specially adapted to cope with the multi-scale nature of this problem has been developed. The method is based on asynchronous integration of the fluid transport equations [19] (fluid discharge equations and compressible Navier–Stokes equations) using an asynchronous adaptative mesh refinement (AAMR method) technique [20] and allows to make a good compromise between accuracy and computation time.

The physical model is described in section 2, section 3 presents a summary of the numerical approach (which has been described in details elsewhere) and the simulations results are discussed in section 4.

2. Physical model

In this section we describe the physical basis of the discharge model (section 2.1) and the gas flow model (section 2.2) and we discuss the coupling between plasma and flow (section 2.3).

2.1. Discharge model

The SDBD model is based on a fluid description of electron and ion transport in air in the classical drift-diffusion and local field approximations that are generally considered to be accurate enough for discharge models at atmospheric pressure.

Three types of charged particles are considered: electrons (index e in the equations below), one generic type of positive ions (index p) and one type of negative ions (index n). In this approach we are not interested in the detailed air chemistry and taking into account only one type of positive and negative ions is sufficient for our purpose.

The continuity equations for electrons, positive and negative ions are written, respectively, as

$$\frac{\partial n_e}{\partial t} + \vec{\nabla} \cdot \vec{\Gamma}_e = (\alpha - \eta) \left\| \vec{\Gamma}_e \right\| - r_{ep} n_e n_p, \tag{1}$$

$$\frac{\partial n_p}{\partial t} + \vec{\nabla} \cdot \vec{\Gamma}_p = \alpha \left\| \vec{\Gamma}_e \right\| - r_{ep} n_e n_p - r_{np} n_n n_p, \tag{2}$$

$$\frac{\partial n_n}{\partial t} + \vec{\nabla} \cdot \vec{\Gamma}_n = \eta \left\| \vec{\Gamma}_e \right\| - r_{np} n_n n_p, \tag{3}$$

where n_e, n_p, n_n are the charged particle densities, $\vec{\Gamma}_e, \vec{\Gamma}_p, \vec{\Gamma}_n$ the charged particle fluxes, α, η, and r_{ep} and r_{np} are, respectively, the ionization coefficient, attachment coefficient, and electron–ion and ion–ion recombination coefficients.

In the drift-diffusion approximation, the charged particles momentum equations are equivalent to writing that the charged particles fluxes are the sum of a drift term and a diffusion term, plus a term due to a drag from the gas flow if present:

$$\vec{\Gamma}_e = \mu_e \left(-n_e \vec{E} - \frac{k_B T_e}{e} \vec{\nabla} n_e \right) + n_e \vec{u}, \tag{4}$$

$$\vec{\Gamma}_p = \mu_p \left(n_p \vec{E} - \frac{k_B T_p}{e} \vec{\nabla} n_p \right) + n_p \vec{u}, \tag{5}$$

$$\vec{\Gamma}_n = \mu_n \left(-n_n \vec{E} - \frac{k_B T_n}{e} \vec{\nabla} n_n \right) + n_n \vec{u}, \tag{6}$$

where (μ_e, μ_p, μ_n) and (T_e, T_p, T_n) are the charged particle mobilities and temperatures, respectively and k_B is the Boltzmann constant; $\vec{u}$ is the velocity of the gas flow. The charged particle mobilities are supposed to depend on the local field as in [15] and are obtained with the BOLSIG+ simulation software [21]. The energy equation is replaced by the local field approximation, i.e. we assume that the energy gained by the charged particles from the electric field is locally balanced by the losses due to collisions with neutral molecules. This rough approximation is used in most of the atmospheric streamer models [22, 23] and is sufficient for our purpose. The ionization and attachment coefficients for air in equations (1)–(3) are therefore supposed to depend on the local reduced field (E/n, where n is the gas density). We used tabulated forms of α and η as a function of E/n, identical to those used in [15]. The charged particle temperatures in the diffusion terms of equations (4)–(6) are taken as constant (1 eV of the electrons and ambient temperature for the ions). Assuming an E/n dependence of the electron temperature may lead to un-physical results in some regions of the discharge (e.g. negative glow or wall sheath) and we prefer imposing a constant electron temperature in equation (4). The value of 1 eV provides a reasonable order of magnitude and we checked that the results presented in this paper are not very sensitive to this value.

Equations (1)–(6) above must be coupled to Poisson's equation for the electric field:

$$\vec{\nabla} \cdot \varepsilon \vec{E} = e(n_p - n_e - n_n) + \sigma \delta_S, \tag{7}$$

where ε is the permittivity (vacuum permittivity, ε_0, in the discharge above the dielectric surface, or dielectric permittivity, supposed to be equal to $5\varepsilon_0$, inside the dielectric layer). $\sigma\delta_S$ represents the contribution of the charges deposited by the discharge on the dielectric surface. These charges are obtained by time integrating charged particles fluxes to the surface.

Finally, the dielectric surface is supposed to emit secondary electrons under ion bombardment, with a secondary emission coefficient γ equal to 0.05:

$$\overrightarrow{\Gamma_e} \cdot \overrightarrow{u}_\perp = -\gamma \overrightarrow{\Gamma_p} \cdot \overrightarrow{u}_\perp,$$

where $\overrightarrow{u}_\perp$ is a unit vector perpendicular to the dielectric surface. Although we found that the results presented here are not very sensitive to the value of the secondary emission coefficient, a systematic study of the influence of the secondary emission coefficient and pre-ionization density is beyond the scope of this paper and is left for a future work.

2.2. Compressible Navier–Stokes equations for the neutral gas

The discharge and gas dynamics equations are coupled through different mechanisms. The gas dynamics is modified by the plasma because of (1) momentum transfer from charged particles to neutral species (the electrohydrodynamic (EHD) force, which is a source term in the Navier–Stokes equations) and (2) energy transfer from charged particles to neutral molecules (heating term in the neutral species energy equation). In turn, the discharge can be modified by the flow because of (1) the drag on the charged particles due to the neutral flow velocity and (2) the changes in gas density possibly associated with the gas heating and gas dynamics and that can modify the charged particle transport coefficients and ionization rate.

These effects are all included in the developed model. In the conditions of the simulations presented in this paper, the plasma generates some gas dynamics effects, but the gas dynamics do not affect the discharge because a very short discharge pulse is considered (i.e. the gas density does not change significantly during the discharge even though gas heating can be large). On the other hand, no external flow is taken into account in the results presented here. The coupling between the discharge model and the gas dynamics model is therefore mainly due to the EHD force per unit volume $\overrightarrow{F_{\mathrm{EHD}}}$, which can impart momentum to the neutral species and generate a gas flow, and to the power density P_{th} associated with gas heating by the charged particles, which can generate pressure gradients and thus gas flow. The forms of $\overrightarrow{F_{\mathrm{EHD}}}$ and P_{th} are discussed in section 2.3. We first write the compressible Navier–Stokes equations for the neutral gas including the EHD term and the heating term.

The continuity equation for the neutral species can be written as

$$\frac{\partial\rho}{\partial t} + \overrightarrow{\nabla}\cdot\left(\rho\overrightarrow{u}\right) = S = M\left[-(\alpha+\eta)\left\|\overrightarrow{\Gamma_e}\right\| + r_{\mathrm{ep}}n_e n_p + r_{\mathrm{np}}n_n n_p\right], \tag{8}$$

where ρ is the mass per unit volume of the neutral gas, M the mass of an air molecule ($\rho = Mn$, where n is the gas density) and $\overrightarrow{u}$ is the average velocity of the flow.

The momentum equation can be written as

$$\frac{\partial\left(\rho\overrightarrow{u}\right)}{\partial t} + \overrightarrow{\nabla}.\left(\rho\overrightarrow{u}\otimes\overrightarrow{u} + pI - \overline{\overline{\tau}}\right) = S\rho\overrightarrow{u} + \overrightarrow{F_{\mathrm{EHD}}}, \tag{9}$$

where $\overrightarrow{F_{\mathrm{EHD}}}$ is the EHD force due to the discharge (see section 2.3), p is the scalar gas pressure, I the unity tensor and $\overline{\overline{\tau}}$ the shear stress tensor, whose components have the classical form

$$\left(\overline{\overline{\tau}}\right)_{ij} = \mu\left[\left(\partial_j u_i + \partial_i u_j\right) - \frac{2}{3}\left(\overrightarrow{\nabla}\cdot\overrightarrow{u}\right)\delta_{ij}\right], \tag{10}$$

where μ is the viscosity and δ_{ij} the Kronecker symbol.

Finally, the energy equation for the neutral species is written as

$$\begin{aligned}\frac{\partial(\rho E)}{\partial t} &+ \overrightarrow{\nabla}\cdot\left[(\rho E + p)\overrightarrow{u} - \kappa\overrightarrow{\nabla}T - \overline{\overline{\tau}}\cdot\overrightarrow{u}\right]\\ &= S\rho E + \overrightarrow{F_{\mathrm{EHD}}}\cdot\overrightarrow{u} + P_{\mathrm{th}},\end{aligned} \tag{11}$$

where E is the total specific energy ($E = (1/(\gamma-1))k_B T + \frac{1}{2}u^2$), T the gas temperature, κ the thermal conductivity of air, γ the heat capacity ratio and P_{th} the power density associated with gas heating from the plasma (see section 2.3).

Finally, the system of equations above is closed with the equation of state of perfect gases:

$$p = \frac{\rho}{M}k_B T. \tag{12}$$

The different constant parameters (the temperature dependence of viscosity and thermal conductivity is not considered here) in the above equations are taken as $\mu = 1.79\times10^{-5}$ Pa s, $\kappa = 0.026\,\mathrm{W\,m^{-1}\,K^{-1}}$, $\gamma = 1.4$.

2.3. Plasma/flow coupling terms

As mentioned above, the fluid flow dynamics is perturbed by the plasma through the EHD force term $\overrightarrow{F_{\mathrm{EHD}}}$ and the heating power density P_{th}.

The EHD force term has been discussed in a previous paper [11] and is written as

$$\begin{aligned}\overrightarrow{F_{\mathrm{EHD}}} = e\left(n_e - n_p - n_n\right)\overrightarrow{E} - k_B T_p\overrightarrow{\nabla}n_p - k_B T_e\overrightarrow{\nabla}n_e\\ - k_B T_n\overrightarrow{\nabla}n_n.\end{aligned} \tag{13}$$

The energy transfer from the plasma to the neutral gas is due to collisions between charged particles and neutral species. We assume that the energy gain by ions from the electric field is totally and instantaneously transferred into gas heating. Therefore the contribution of ion–neutral molecule collisions to the gas heating term P_{th} is simply equal to $(\overrightarrow{j_p} + \overrightarrow{j_n})\cdot\overrightarrow{E}$.

The thermal energy transfer from electrons to neutral species is more complicated and this question has been discussed in recent papers [24–26]. The energy transferred by electrons per unit volume and per unit time to the gas molecules through elastic collisions and rotational excitation is instantaneously converted into gas heating and represents a small part (a few per cent at low electric fields [28]) of the total power density absorbed by the electrons $P_{\mathrm{elec}} = \sigma_e E^2$, where σ_e is the electron conductivity. The energy transferred by electrons into other degrees of freedom of the molecules (vibrational excitation or electronic excitation) is released into gas heating on different timescales [28]. In this paper we are interested in pressure waves that can be generated by fast energy deposition in the gas. Since a detailed model of air chemistry is outside the scope of this paper we used a simple, phenomenological model of energy transfer. It seems that there is an agreement between different authors [24–26] that a relatively large percentage of the energy spent by the electrons in electronic excitation of N_2 is transferred very quickly into gas heating due to the quenching of nitrogen excited states by oxygen molecules. We assume here that 30% of the electron energy spent in electronic excitation of air is instantaneously released into gas heating, which is consistent with [28]. The energy stored in vibrational excitation is released into gas heating through vibration–translation (V–T) collisions on a longer timescale. Since our model does not allow a detailed description of this process, we use the energy relaxation time for V–T collisions, τ_{VT}, as a parameter.

The power density spent in gas heating is therefore given by

$$P_{\mathrm{th}} = (P_{\mathrm{el-R}} + P_{\mathrm{E}} + P_{\mathrm{VT}}) + P_{\mathrm{ions}}. \tag{14}$$

The terms in parentheses on the rhs of equation (14) correspond to the contribution of electrons to gas heating while P_{ions} is the contribution of the ions. The electron contribution to gas heating is divided into $P_{\mathrm{el-R}}$ (elastic and rotational excitation collisions, supposed to be instantaneously released into gas heating), P_{E} (electronic excitation, i.e. 30% of the energy going in electronic excitation of air, supposed to be instantaneously released into gas heating), and P_{VT} (vibrational excitation, released into gas heating with a time constant τ_{VT}).

$P_{\mathrm{el-R}}$ and P_{E} are written as

$$P_{\mathrm{el-R}} = \eta_{\mathrm{el-R}} P_{\mathrm{elec}}, \quad P_{\mathrm{E}} = \xi \eta_{\mathrm{E}} P_{\mathrm{elec}}, \quad \text{with } P_{\mathrm{elec}} = \sigma_{\mathrm{e}} E^2, \tag{15}$$

where $\eta_{\mathrm{el-R}}$ is the fractional power deposited in elastic collision and rotational excitation of air molecules, η_{E} the fractional power deposited in electronic excitation of the nitrogen molecules and $\xi = 30\%$.

P_{VT} in equation (14) represents the power density corresponding to the conversion of vibrational energy into translational energy (V–T energy transfer) and is obtained as a solution of the phenomenological equation

$$\frac{\partial P_{\mathrm{VT}}}{\partial t} + \frac{1}{\tau_{\mathrm{VT}}} P_{\mathrm{VT}} = \frac{1}{\tau_{\mathrm{VT}}} \eta_{\mathrm{V}} P_{\mathrm{elec}}, \tag{16}$$

where η_{V} is the fractional electron power deposited in vibrational excitation of the air molecules.

Equation (16) above simply means that the energy stored in vibrational excitation is released into heating with a time delay equal to τ_{VT}.

$\eta_{\mathrm{el-R}}$, η_{E} and η_{V} have been calculated as a function of E/n using the BOLSIG+ software [21] and are plotted in figure 1.

The gas heating model described above is very simple and phenomenological but is sufficient for our purpose. A similar description of the release of the energy stored in the vibrational manifold into gas heating has been used by Naidis [27] and Benilov and Naidis [28] (except that we did not try to use a self-consistent, temperature dependent value of the vibrational relaxation time τ_{VT}, but we rather considered τ_{VT} as a parameter).

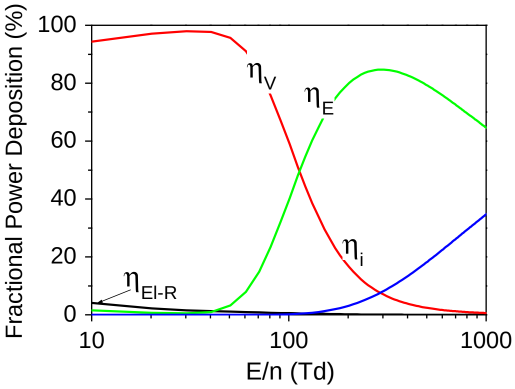

Figure 1. Fractional power dissipated by electrons in air as a function of E/n, into elastic collisions and rotational excitation, $\eta_{\mathrm{el-R}}$, electronic excitation, η_{E}, vibrational excitation, η_{V}, ionization, η_{I}.

3. Numerical approach

We describe here only the main features of our numerical approach. The details concerning the numerical techniques and discretization schemes that we used can be found in the references.

3.1. A multi-scale problem

Solving the equations described in the previous section in real conditions is a challenge because the physical problem is multi-scale in nature, both in time and space. The SDBD leads to the formation of surface streamers [11–15] with plasma densities up to $10^{20}\,\mathrm{m}^{-3}$ or larger. The Maxwell relaxation time, $\tau_{\mathrm{M}} = (\varepsilon_0/\sigma_{\mathrm{e}})$, is smaller than 10^{-12} s for these plasma densities, which means that for explicit time integration of the Poisson-transport equations, the integration time step dt must be less than τ_{M} (explicit time integration of the Poisson-transport system of equations means that Poisson's equation and charged particle transport equations are solved successively and that the electric field calculated at time t^k is supposed to be constant during the integration of the charged particle transport equation between times t^k and $t^{k+1} = t^k + \mathrm{d}t$). Another constraint if the continuity equation is solved explicitly (i.e. density at time t^{k+1} is expressed explicitly as a function of density at time t^k) is that the integration time step of the electron transport equations must be less than the Courant–Friedrich–Levy (CFL) time, $\tau_{\mathrm{CFL}} = (\Delta x/v_{\mathrm{e}})_{\mathrm{min}}$ (Δx is the grid size and v_{e} the electron mean velocity), which is also smaller than 10^{-12} s in our conditions. The gas motion involves much longer timescales.

We want to study the phenomena over tens or hundreds of microseconds, i.e. more than 10^7 times the smaller time step. The grid spacing must be small enough to resolve the space charge sheath at the head of the streamer or next to the exposed electrode tip when this electrode plays the role of a cathode. The sheath can be smaller than 10 μm under atmospheric pressure conditions. On the other hand, the streamer channel length can reach 1 cm or more, and we want to follow the gas perturbation induced by the discharge over lengths of several centimetres, i.e. more than 1000 times the sheath length.

The multi-scale nature of this problem in space and the fact that only small regions (e.g. streamer head or cathode sheath) need a very fine grid impose the use of an adaptative mesh refinement technique.

The CFL and Maxwell relaxation time constraints could be overcome by solving implicitly or semi-implicitly charged particle transport equations and the plasma-field coupling (Poisson's equation).

In previous papers [11–15] we performed implicit time integration of the charged particle transport equations using the Scharfetter–Gummel discretization scheme, associated with a semi-implicit integration of Poisson's equation (i.e. when solving Poisson's equation at time t^k, the charged particle densities on the right hand side of Poisson's equation are estimated at time t^{k+1}). This allows integration time steps much larger than the CFL and Maxwell relaxation times. However, the accuracy of this approach is sufficient only for small enough grid spacing. For large grid spacing errors due to numerical diffusion become important.

In order to get a good compromise between accuracy and computation time on large simulation domains we have developed an asynchronous time integration method associated with an adaptative mesh refinement technique, the AAMR method described below.

3.2. *Strong plasma/aerodynamic coupling using AAMR*

As said above and because of the multi-scale nature of the problem, it is necessary to use an adaptative mesh refinement technique to allow large grid spacing in regions of the simulation domain that are less active. To prevent excessive numerical diffusion due to large grid spacing the transport equations must be solved explicitly and with a second order scheme. On the other hand, the CFL time constraint imposes a time integration step Δt smaller than the minimum CFL time $\tau_{\mathrm{CFL}} = (\Delta x/v_{\mathrm{e}})_{\min}$, which can be extremely small.

The local CFL time, $\tau_{\mathrm{CFL,local}} = (\Delta x/v_{\mathrm{e}})$, can be very different in different regions of the simulation domain. For example, the local CFL time is very small in the streamer head where the grid spacing must be on the order of a few micrometres and the electron velocity can be larger than $10^6\,\mathrm{m\,s^{-1}}$, but the local CFL time is much larger in the less active region of the discharge. In order to save computation time, it is therefore tempting to perform time integration of the transport equations with different time steps at different locations of the grid. This is the principle of the asynchronous method described by Unfer *et al* [19].

The numerical scheme used for the integration of the charged particle transport equations is the classical MUSCL scheme [29]. The MUSCL method is based on a linear piecewise reconstruction of the interface states based on the cell-centred values giving second order space accuracy. To avoid oscillations the reconstructed slopes are limited by using a minmod limiter. The constraint on the time step for this numerical scheme is actually half the CFL value above.

As shown in [19], a factor of 10 (or more, depending on the geometry) in computation time can be gained when using asynchronous time integration of the discharge equations with a MUSCL scheme, compared with a standard MUSCL scheme with synchronous time integration.

The method has also been extended to solve the 2D laminar compressible unsteady Navier–Stokes equations. The asynchronous integration formalism that we have developed allows to use directly the HLLE Riemann solver [30] with a MUSCL scheme for the reconstruction of the interface states and a classical viscous flux discretization.

The asynchronous time integration method has been recently extended to cope with an adaptative mesh refinement technique, and we call this method AAMR [20]. Thanks to the AAMR technique, strongly coupled calculations can be performed using the same mesh for plasma and aerodynamics. This enables to control without any interpolation the momentum and energy transfer from the plasma to the neutral gas. Different classes of time steps are used, for electrons, ions and neutral species. The electron time steps are also used to compute the source terms of the seven conservation equations. From a Navier–Stokes point of view this means that momentum and energy can be accumulated into a cell without being transported immediately.

The adaptive meshing relies on two criteria. The first criterion is based on a pseudo-Debye length for the plasma: $\hat{\delta} = \sqrt{\frac{2\varepsilon_0 k_{\mathrm{B}} T_{\mathrm{e}}}{e^2(n_{\mathrm{e}}+n_{\mathrm{p}}+n_{\mathrm{n}})}}$ (see [20]). The second criterion relies on velocity jumps for the Navier–Stokes equations. In practice if any component of the neutral gas velocity differs by more than $1\,\mathrm{mm\,s^{-1}}$, the cell is refined. A cell is merged if the velocity components differ less than $0.1\,\mathrm{mm\,s^{-1}}$. If any of the refinement criteria are met, the cell is refined and the cells are merged only when both fusion criteria are met. In order to keep the total cell number under control, different minimal cell size are used for each criterion. The minimal cell size for the plasma is smaller than for the Navier–Stokes equations. However, the Navier–Stokes fusion criterion has to be met even for the cells which are smaller than the minimal Navier–Stokes cell size. This is mandatory to prevent that the gradients created by the plasma in the Navier–Stokes equations become averaged out when the plasma decays.

The combination of the asynchronous time integration and adaptative mesh refinement (AAMR) leads to much faster calculations (a factor of 100 or more). The algorithms and the coding must, however, be carefully optimized to obtain full benefit from the AAMR method.

4. Simulation results

4.1. *Computational domain and initial mesh*

The dimensions of the simulation domain used in the rest of this paper are 0.0768×0.0768 m (see figure 2). The dielectric layer is 300 μm thick. The upper electrode starts at 0.03 m and ends at 0.0351 m (5.1 mm long). The lower electrode starts at 0.0351 m and ends at 0.0399 m (4.8 mm long). The electrode thickness is 37.5 μm. Unless otherwise mentioned, the minimal cell size used is 18.75 μm for the plasma criterion

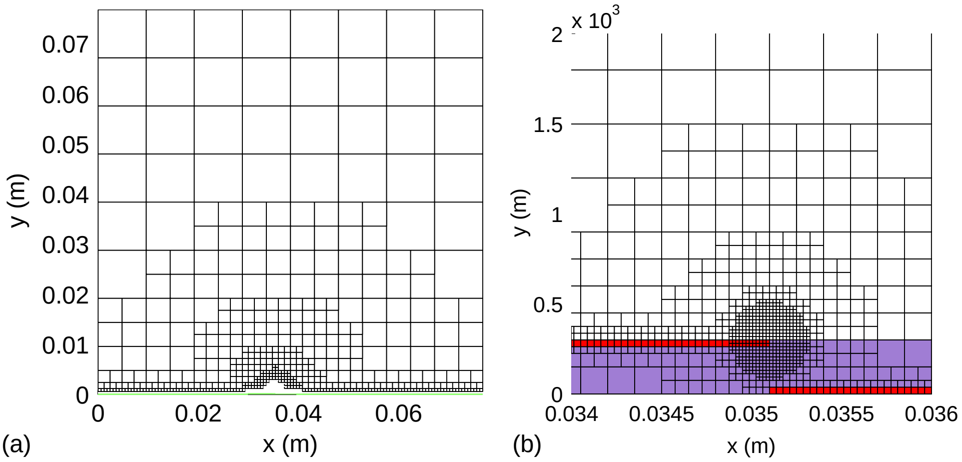

Figure 2. Simulation domain and initial mesh: (*a*) whole domain (the fine mesh around the tip of the top electrode is not shown), (*b*) zoom of the region close to the tip of the top electrode, where the discharge is initiated.

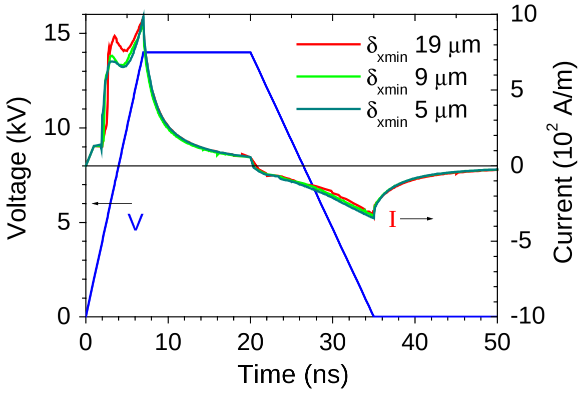

Figure 3. Applied voltage pulse and calculated current for three different values of the minimum cell size.

and 0.15 mm for the Navier–Stokes criterion. Smaller minimal cell size for the plasma has also been used for comparison. Figure 2 shows the initial mesh, with small cell sizes in the large electric field region next to the tip of the electrode above the dielectric layer.

The initial charged particle densities (electron and positive ions) are supposed to be uniform and equal to 10^{10} m^{-3} in the whole simulation domain.

The results presented below have been obtained for an applied voltage pulse of total duration 35 ns, with linear rise and decay times (7 ns and 15 ns, respectively) and a 14 kV plateau of 13 ns. The applied voltage pulse is shown in figure 3, together with the calculated current.

4.2. Plasma dynamics for a 35 ns voltage pulse at 14 kV

The calculated current of figure 3 is composed of two pulses. The first current pulse starts during the voltage rise, passes through a first maximum at about 5 ns, slightly decays (due to the charging of the surface), and increases again (because of the continuous increase in the applied voltage) and reaches a second maximum, on the order of 10^3 A m^{-1}, at the end of the voltage rise. During the voltage plateau, the current decays because of the charging of the dielectric surface. During the first current pulse the top electrode plays the role of an anode and a positive ion sheath (streamer head) develop along the surface, charging positively the dielectric layer surface. When the applied voltage starts to decay, the current decreases faster, changes sign and a second (negative) current pulse occurs. The second current pulse is due to a breakdown between the top electrode, whose voltage rapidly decreases to zero (in 15 ns), and the dielectric surface, which has been positively charged by the first pulse. Even though the top electrode voltage does not become negative, its potential quickly becomes less than the potential of the dielectric surface and a negative current is collected. We will see below that the plasma due to the first pulse is still present when the second current pulse takes place. The second current pulse is therefore due to collection of charges generated by the previous pulse plus charges created by the strong multiplication associated with the increasing potential drop between the dielectric surface and the top electrode during the decay of the applied voltage. The top electrode plays the role of a cathode during this phase. Note that the charge collected during the first current pulse (integral of the current between 0 and ∼20 ns) is larger than the charge collected during the second pulse, i.e. the total charge on the dielectric surface at the end of the discharge is still positive. This means that if a sequence of similar voltage pulses is applied between the electrodes, the discharge pulses will evolve so that the charges transferred by each successive positive and negative current pulses are identical and the average charge on the dielectric surface is positive.

The current displayed in figure 3 is plotted for three different values of the minimum cell size (19, 9 and 5 μm). Although slight differences can be observed, the agreement is satisfactory.

Figures 4 and 5 show the time evolution of the electron density and potential at three times of the first and second current pulses, respectively.

During the first pulse (figure 4(*a*)), the plasma filament (streamer) propagates along the dielectric surface with a velocity on the order of 5×10^7 cm s^{-1} (3 mm in 6 ns). This can be compared with the experimental results of Starikovskii

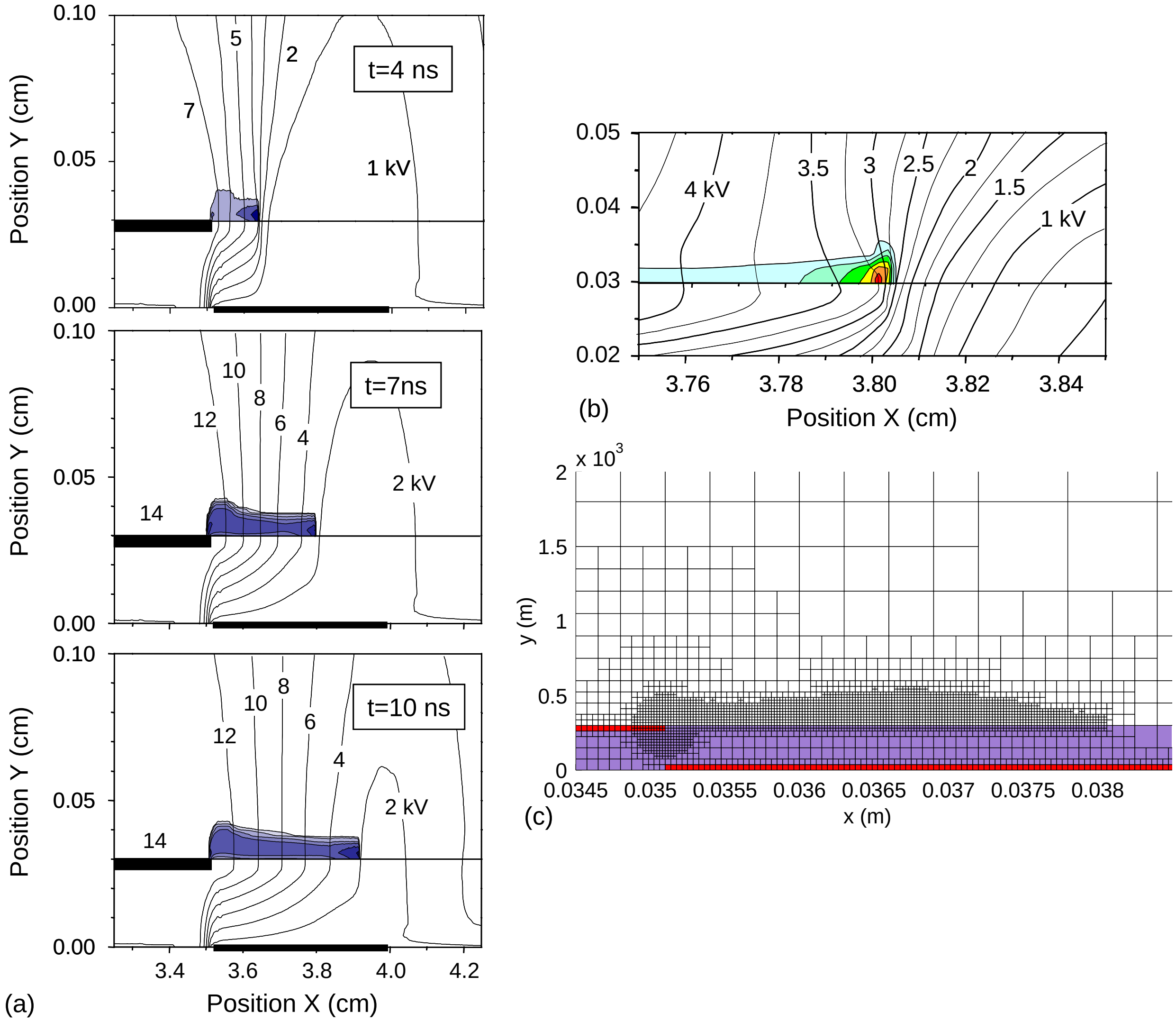

Figure 4. (*a*) Electron density (grey scale) and potential distribution (contours) at three different times of the first current pulse. The plotted contour levels are, in units of 10^{21} m^{-3}, 0.1, 0.5, 1 for $t = 4$ ns (maximum 2×10^{21} m^{-3}), 0.01, 0.02, 0.05, 0.1, 0.2, … for $t = 7$ ns (maximum 1.1×10^{21} m^{-3}) and for $t = 10$ ns (maximum 0.7×10^{21} m^{-3}). The electric potential contour levels are indicated in kV in the figure. (*b*) Space charge density distribution ($n_i - n_e - n_n$) and potential contours in the region of the streamer sheath at time $t = 7$ ns under the conditions of (*a*). The represented contours of the space charge density are 2, 4, 6, 8, 10, 12 $\times 10^{19}$ m^{-3}. (*c*) Computational mesh at $t = 7$ ns.

et al [18] who measured a velocity of 10^8 cm s^{-1} under similar conditions. This shows that realistic simulation results can be obtained even though photoionization or photoemission are not included in the model. The fast propagation of the surface streamer in the simulation is due to the presence of initial charges in the discharge volume and to secondary electron emission by ion impact (ions generated in the streamer head close to the surface can cross a 10 μm sheath on a nanosecond timescale). The thickness of the streamer channel is on the order of 100 μm.

The potential along the dielectric surface increases during the first pulse because of the charging of the dielectric by positive ions. At $t = 10$ ns (figure 4(*a*)), the average field E along the surface is on the order of 28 kV cm^{-1} (14 kV over 5 mm), and E/p is about 37 V cm^{-1} Torr^{-1}; i.e. slightly over the critical field for which ionization and attachment frequencies are equal, in air. As soon as the applied voltage stops increasing, the field over the dielectric surface drops below the critical field because of the charging of the surface by positive ions and the plasmas decays (current decay after $t = 10$ ns in figure 3).

The streamer head cannot be clearly seen in figure 4(*a*) because of its small size. Figure 4(*b*) shows a close view of the streamer head region and displays the net charge density distribution ($n_i - n_e - n_n$) and potential contours at time $t = 7$ ns. We can see the large potential drop over a few tens of micrometres at the tip of the filament. This region corresponds to the streamer head and the net charge density (positive ion sheath) in that region is on the order of 10^{20} m^{-3}.

Figure 4(*c*) illustrates the adaptive mesh refinement method and displays the mesh used in the simulation at time $t = 7$ ns.

During the decrease in the applied voltage (i.e. after $t = 20$ ns), the potential on part of the dielectric surface becomes higher than the top electrode voltage. This can be seen in figure 5 where a maximum of the dielectric surface

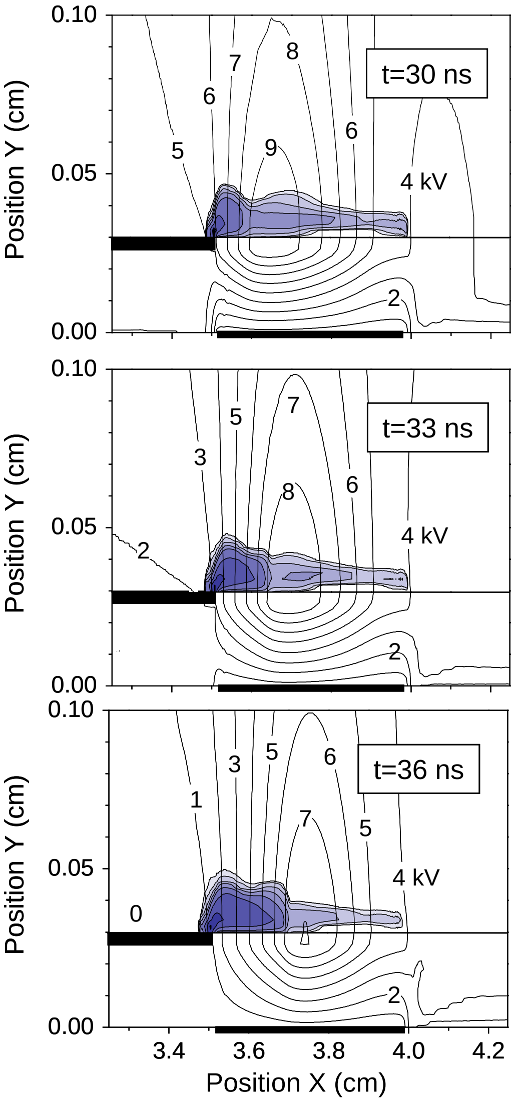

Figure 5. Electron density (grey scale) and potential distribution (contours) at three different times of the first current pulse. The plotted contour levels are 0.01, 0.02, 0.05, 0.1, 0.2, . . . , $\times 10^{20}$ m^{-3}, with a maximum value of 1.2×10^{20} m^{-3} for $t = 30$ ns, 2.4×10^{20} m^{-3} for $t = 33$ ns and 2.2×10^{20} m^{-3} for $t = 36$ ns. The electric potential contour levels are indicated in kV in the figure.

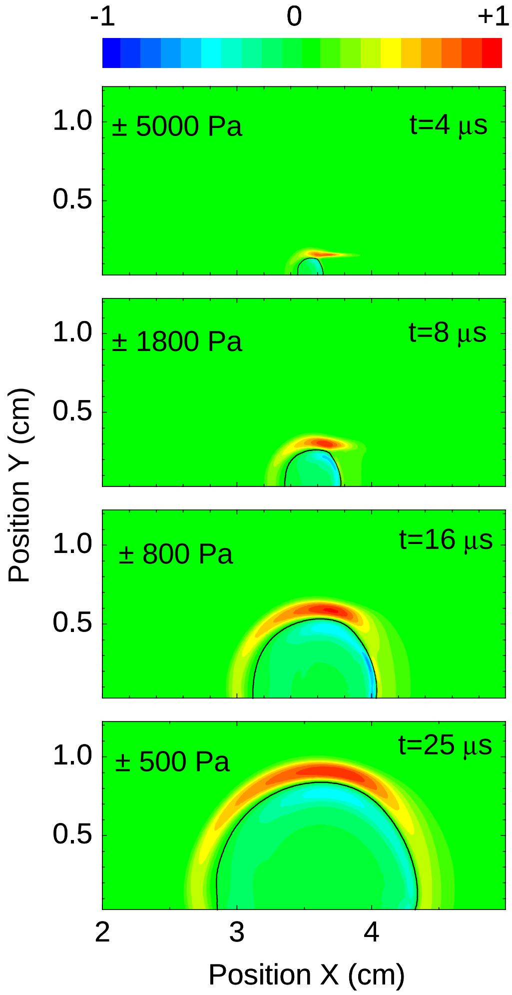

Figure 6. Spatial distribution of the gas pressure perturbation ΔP (with respect to atmospheric pressure) in the micro shock wave generated by the discharge of figures 3–5 at four different times. The pressure range of the plot is indicated in each figure. The contour line ($\Delta P = 0$) separates the region of positive and negative ΔP. Gas heating from elastic collisions, rotational to translational energy transfer and electronic excitation (30% of electronic excitation instantaneously transferred into translational energy) is included.

potential appears at a position $x \sim 3.7$ cm. Because of this potential distribution with a potential maximum at $x \sim 3.7$ cm, the electron current during the second pulse flows to this point on the dielectric surface from both sides, i.e. from the left side (current flowing from the top electrode which plays the role of a cathode) and from the right side (where a smaller, residual plasma density from the first pulse is still present).

We see in figure 5 the propagation of an intense filament along the dielectric surface from the top electrode (cathode) to the point of maximum electric potential at $x \sim 3.7$ mm. The positive ion density (not shown here) shows the presence of an ion sheath on the tip of the top electrode. As said above, electrons also flow to the point of maximum potential at $x \sim 3.7$ mm, from the right side of this point. The dielectric surface in this region also plays the role of a cathode and we can see a depletion of the electron density close to the surface, due to the presence of an ion sheath. The filament on the right side of the potential maximum is much less intense than the one on the top electrode side.

4.3. *Gas dynamics and shock wave initiated by the discharge*

The Navier–Stokes equations are solved together with the plasma equations, during and after the discharge pulses. The effect of the discharge on the gas dynamics can be seen on the plots of the pressure variations induced by the discharge at different times. Figure 6 shows the space distribution of the pressure perturbation ΔP induced by the discharge at four different times (4, 8, 16 and 25 μs). The perturbation propagates like a micro shock wave generated in a region around the tip of the top electrode. We see that ΔP is about 1000 Pa when the perturbation front is 5 mm away from the discharge region where it has been generated. The results of figure 6 have been obtained assuming that the contributions

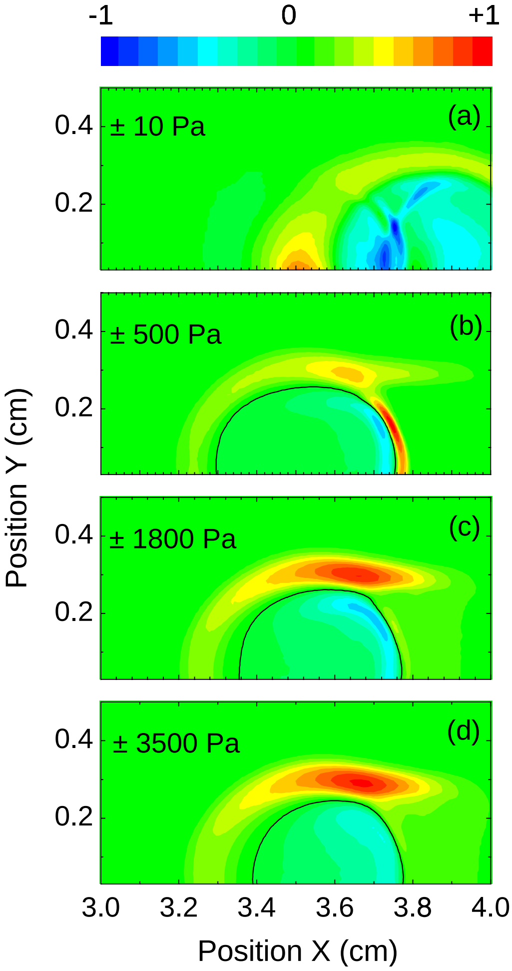

Figure 7. Spatial distribution of the gas pressure perturbation at time $t = 8\,\mu$s, in the micro shock wave generated by the discharge under the conditions of figures 3–5, and with different assumptions on gas heating: (*a*) no gas heating, (*b*) only heating by ions is included, (*c*) ions, electron elastic and rotational excitation and electronic excitation (30% instantaneously converted into gas heating) and (*d*) same as (*c*) with vibrational excitation included, with a relaxation time for V–T collisions $\tau_{VT} = 1\,\mu$s. The pressure range of the plot is indicated in each figure.

to the gas heating term P_{th} are ion heating, elastic collisions and rotational excitation, and 30% of the power deposited in electronic excitation, i.e. $P_{th} = (P_{el-R} + P_E) + P_{ions}$ (vibrational to translational energy transfer is not included).

Figure 7 compares the pressure wave calculated at time $t = 8\,\mu$s, for four different assumptions on the gas heating mechanisms: no gas heating i.e. the only effect of the plasma on the flow is the EHD force ($P_{th} \equiv 0$), ion contribution only ($P_{th} \equiv P_{ions}$), contribution of ions, elastic collisions and rotational excitation, and quenching of the excited states ($P_{th} = (P_{el-R} + P_E) + P_{ions}$), and same plus contribution of vibrational to translational (V–T) energy transfer ($P_{th} = (P_{el-R} + P_E + P_{VT}) + P_{ions}$), with $\tau_{VT} = 1\,\mu$s. We see in this figure that the amplitude and the shape of the micro shock wave are significantly different when one or the other of these four assumptions is made. The micro shock wave is practically absent in the first case (figure 7(*a*)) where gas heating is not included. The small effect that can be observed in figure 7(*a*) is due to the EHD force. The amplitude of the pressure wave increases by a factor of about 4 when the contribution of quenching of the excited states is included, and by another factor of 2 when V–T energy transfer is taken into account.

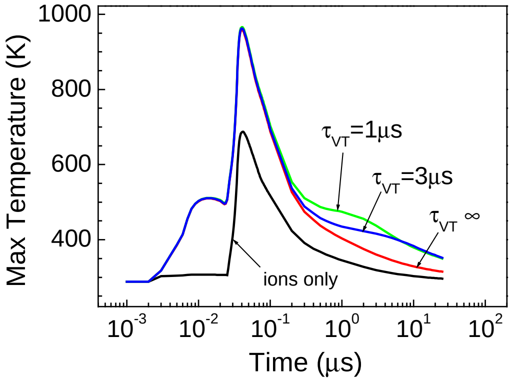

Figure 8. Maximum gas temperature as a function of time for different assumptions on gas heating.

The cylindrical part of the pressure perturbation that can be observed in figures 6 and 7 is due to the fact that a large part of the energy is released at the tip of the top electrode during the second pulse, i.e. in the cathode region of the discharge where large ion heating and electron excitation take place. The more complex shape around the overall cylindrical shape is due to the fact that a large part of the energy is also released during the filament propagation along the surface (in the streamer head during the first pulse, and in the plasma channel). This is the reason why the pressure perturbation of figures 6 and 7 has a large component parallel to the surface.

The propagation velocity of the shock wave can be deduced from the pressure distribution at different times. We find that, in the conditions of figure 6, the propagation velocity of the micro shock wave is 450 m s^{-1} during the first 100 ns, and quickly decreases to about 350 m s^{-1}, close to the sound velocity. This is in good agreement with the experimental results of Starikovskii *et al* [18] except that the decay of the velocity occurs at later times (on the order of 1 μs) in the experiments.

The micro shock wave generation is due to the very fast energy release into gas heating. We performed similar calculations for sinusoidal voltages in the 1–10 kHz range. The streamers that form under these conditions are less energetic (because of the slower voltage rise, the overvoltage is not as important and the streamer forms at a lower voltage, closer to the breakdown value) and the current pulse duration is longer. A smaller energy is deposited on a longer timescale and therefore no significant shock wave is observed in the simulation under these conditions.

Figure 8 shows the time evolution of the calculated maximum gas temperature for different assumptions on the heating term. We see that the maximum gas temperature can be as large as 1000 K at the end of the discharge pulses, under these conditions. The gas temperature comes back to ambient temperature on a microsecond timescale. As expected, because of the time delay in the V–T energy transfer,

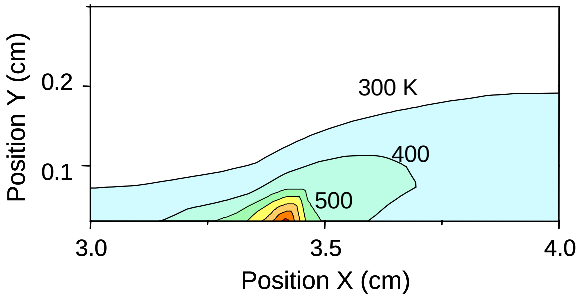

Figure 9. Distribution of the gas temperature after the end of the discharge (time $t = 40$ ns), under the conditions of figures 3–5.

the maximum temperature is not (but the temperature decay is) affected by the V–T transfer.

The space distribution of the gas temperature at time $t = 40$ ns, just after the discharge pulse is shown in figure 9. We clearly see a hot spot in the region close to the tip of the top electrode, where a cathode sheath forms during the second current pulse. The power density deposited in gas heating in this cathode sheath region is quite large and leads to fast heating. The energy deposited during the first current pulse is also large (even larger than during the second current pulse, see below), but is distributed over a larger volume, during the streamer propagation along the surface. This is the reason why the gas temperature above the electrode above the dielectric layer ($x > 3.5$ cm) is smaller, on the order of 400–500 K, but the temperature increase takes place in a larger volume.

Calculations of the maximum gas temperature have also been performed for different values of the minimum cell size. The results show that the calculated maximum temperature can be significantly larger than 1000 K when the minimum cell size is 5 μm instead of 19 μm. This difference is due to the poor resolution of the cathode sheath when the mesh is too large. The local power density is significantly larger for the smallest mesh, but the total energy deposition is only 10–20% larger when the minimum cell size is changed from 19 to 5 μm. The calculated pressure wave amplitude at $t = 8\,\mu$s is about twice as large for the smallest mesh. Note that it is difficult to get a very accurate estimation of the maximum local power deposition not only because this needs a very fine resolution of the cathode or streamer sheath but also because the physical model is limited by the local field approximation (i.e. the electron energy deposition by electrons in the sheath actually takes place over a larger region because of non-local effects; these effects tend to lower the maximum power deposition).

The energy deposition through different channels is represented in figure 10 as a function of time. More energy is deposited during the first pulse, since, as we mentioned earlier, the second pulse transfers a smaller charge than the first one in this simulation. We see that the energy release from electronic excitation is significantly larger than the energy deposited by ions. The largest contribution to gas heating is stored in vibrational excitation but is released on a longer timescale.

Figure 10 also shows that the total energy deposited by the discharge is on the order of 0.5 mJ cm^{-1}. This is close to the experimental value given by Starikovskii *et al* [16, 18] for a similar voltage pulse.

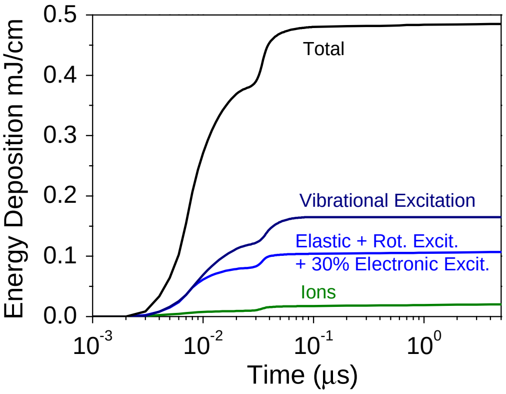

Figure 10. Calculated energy deposition as a function of time: contribution of ions to gas heating, contribution of electron elastic and rotational excitation and electronic excitation (30% supposed to be converted into heating), energy stored in the vibration molecules and total energy deposited by the discharge in the gas.

5. Conclusion

We have developed a model to describe plasma–flow interaction under conditions of fast energy deposition by a surface discharge plasma (nanosecond voltage pulse in a SDBD), leading to shock wave formation and propagation. The model solves fluid discharge equations coupled with the compressible form of Navier–Stokes equations.

The numerical model is based on an original asynchronous time integration method combined with an adaptative mesh refinement technique. This asynchronous time integration uses a local CFL constraint, so less computation time is needed in less active regions where the particle velocity is smaller or the grid spacing is larger. Because of the adaptative mesh refinement, the AAMR method also allows to cope with large simulation domains. The method has proven to be very efficient (the speed of the simulation can be increased by a factor of 100 with respect to standard methods), provided that care is taken in the coding and in the algorithms for asynchronous time integration and adaptative mesh refinement (the details are not described here).

The simulations have been performed for a 14 kV voltage pulse of rise time 7 ns, duration (plateau) 13 ns and decay 15 ns, and for a discharge over a 300 μm thick dielectric layer and with 5 mm long electrodes in a standard SDBD geometry. The gas dynamics induced by gas heating is followed for several microseconds after the end of the voltage pulse.

The following conclusions can be drawn:

- A first current pulse takes place during the voltage rise, when the top electrode plays the role of an anode. During this pulse a streamer discharge forms and spreads along the dielectric surface. The streamer head propagates along the dielectric surface at a velocity of around 5×10^7 cm s^{-1}. The density in the streamer channel is on the order of 10^{20} m^3. During the fast decay of the applied voltage, the potential difference between the charged dielectric surface and the top electrode quickly increases to values over the breakdown voltage and a second current pulse is initiated. During this pulse the exposed electrode plays the role of a cathode and a cathode sheath forms over it.

- The fast energy deposition under the considered conditions of a nanosecond voltage pulse leads to a fast increase in the gas temperature in the discharge volume, with a very localized maximum of about 1000 K next to the tip of the exposed electrode, at the end of the discharge pulse. The location of this maximum coincides with the cathode sheath region of the second discharge pulse. This high gas temperature is associated with a very large pressure increase in a small volume.
- The local pressure increase due to fast gas heating leads to the generation and propagation of a micro shock wave with a pressure increase of a few 1000 Pa when the size of the perturbation is in the millimetre range. The magnitude of the pressure increase depends on the detailed mechanisms of energy transfer from electron to the gas molecules. A small effect is seen when only instantaneous ion heating is considered. This effect is multiplied by 4 when 30% of the energy deposited in electronic excitation by electrons is supposed to be instantaneously converted into gas heating, and by a factor of 8 when the contribution of V–T energy transfer is included, with a V–T relaxation time of 1 μs.

Although the gas heating model used in this paper is approximate, the presented results are consistent with the experiments of Starikovskii *et al* if a large part of the energy absorbed by the electrons is supposed to be quickly released into gas heating. The numerical results confirm that in contrast with the sinusoidal regime of DBDs where momentum gained by ions from the field is transferred to the gas (ion wind effect), the aerodynamics effects in a nanosecond discharge are associated with the fast gas heating in the boundary layer. Whether the observed effects on the flow are due to the gas dynamics induced by the nanosecond discharge or to changes in the viscosity due to gas heating will be the subject of further investigations.

Acknowledgments

The material in this article is based on the work supported by EOARD (European Office of Aerospace Research and Development), under contract no FA8655-06-C-4004. Support from the EADS Foundation is also acknowledged. The authors would like to thank A Starikovskii and S Panchesnyi for communication of their papers prior to publication.

References

[1] Léger L, Moreau E and Touchard G G 2002 Effect of a DC corona electrical discharge on the airflow along a flat plate *IEEE Trans. Ind. Appl.* **38** 1478–85

[2] Roth J R, Sherman D M and Wilkinson S P 2000 *AIAA J.* **38** 1166

[3] Roth J R 2003 Aerodynamic flow acceleration using paraelectric and peristaltic electrohydrodynamic effects of a one atmosphere uniform glow discharge plasma *Phys. Plasmas* **10** 2117–26

[4] Enloe C L, McLaughlin T E, VanDyken R D, Kachner K D, Jumper E J, Corke T C, Post M and Haddad O 2004 Mechanisms and responses of a single dielectric barrier plasma actuator: geometric effects *AIAA J.* **42** 595–604

[5] Enloe C L, McHarg M G and McLaughlin T E 2008 Time-correlated force production measurements of the dielectric barrier discharge plasma aerodynamic actuator *J. Appl. Phys.* **103** 073302

[6] Moreau E 2007 Airflow control by non-thermal plasma actuators *J. Phys. D: Appl. Phys.* **40** 605

[7] Opaits D F, Likhanskii A V, Neretti G, Zaidi S, Shneider M N, Miles R B and Macheret S O 2008 Experimental investigation of dielectric barrier discharge plasma actuators driven by repetitive high-voltage nanosecond pulses with dc or low frequency sinusoidal bias *J. Appl. Phys.* **104** 043304

[8] Likhanskii A V, Shneider M N, Macheret S O and Miles R B 2008 Modeling of dielectric barrier discharge plasma actuator in air *J. Appl. Phys.* **103** 053305

[9] Jayaraman B, Cho Y C and Shyy W 2008 Modeling of dielectric barrier discharge plasma actuator *J. Appl. Phys.* **103** 053304

[10] Singh P and Roy S 2005 Simulation of an asymmetric single dielectric barrier plasma actuator *J. Appl. Phys.* **98** 083303

[11] Boeuf J P and Pitchford L C 2005 Electrohydrodynamic force and aerodynamic flow acceleration in surface dielectric barrier discharge *J. Appl. Phys.* **97** 103307

[12] Boeuf J P, Lagmich Y, Callegari T and Pitchford L C 2007 Electrohydrodynamic force in dielectric barrier discharge plasma actuators *J. Phys. D: Appl. Phys.* **40** 652

[13] Lagmich, Callegari T, Unfer T, Pitchford L C and Boeuf J P 2007 Electrohydrodynamic force and scaling laws in surface dielectric barrier discharges *Appl. Phys. Lett.* **90** 051502

[14] Lagmich Y, Callegari T, Pitchford L C and Boeuf J P 2008 Model description of surface dielectric barrier discharges for flow control *J. Phys. D: Appl. Phys.* **41** 095205

[15] Boeuf J P, Lagmich Y, Pitchford L C 2009 Contribution of positive and negative ions to the electrohydrodynamic force in a dielectric barrier discharge plasma actuator operating in air *J. Appl.Phys.* at press

[16] Roupassov D, Nudnova M, Nikipelov A and Starikovskii A 2008 Flow separation by plasma actuator with nanosecond pulse periodic discharge *46th AIAA Aerospace Science Meeting and Exhibit (Reno, NV, 7–10 January 2008)* paper AIAA-2008-1367

[17] Roupassov D and Starikovskii A 2008 Development of nanosecond surface discharge in 'actuator' geometry *IEEE Trans. Plasma Sci.* **36** 1312

[18] Starikovskii A, Roupassov D, Nikipelov A and Nudnova M 2009 SDBD plasma actuator with nanosecond pulse periodic discharge *Plasma Sources Sci. Technol.* **18** 034015

[19] Unfer T, Boeuf J P, Rogier F and Thivet F 2007 An asynchronous scheme with local time stepping for multi-scale transport problems: application to gas discharges *J. Comput. Phys.* **227** 898

[20] Unfer T, Boeuf J P, Rogier F and Thivet F 2009 Multi-scale gas discharge simulations using asynchronous adaptive mesh refinement *Comput. Phys. Commun.* at press

[21] Hagelaar G J M and Pitchford L C 2005 Solving the Boltzmann equation to obtain electron transport coefficients and rate coefficients for fluid models *Plasma Sources Sci. Technol.* **14** 722

[22] Montjin C, Hundsdorfer W and Ebert U 2006 An adaptive grid refinement strategy for the simulation of negative streamers *J. Comput. Phys.* **219** 801

[23] Pancheshnyi S, Segur P, Capeillere J and Bourdon A 2008 Numerical simulation of filamentary discharges with parallel adaptive mesh refinement *J. Comput. Phys.* **227** 6574

[24] Popov N A 2001 Investigation of the mechanism for rapid heating of nitrogen and air in gas discharges *Plasma Phys. Rep.* **27** 886

[25] Guerra V, Sa P A and Loureiro J 2004 Kinetic modeling of low-pressure nitrogen discharges and post-discharges *Eur. J. Appl. Phys.* **28** 125

[26] Flitti A and Pancheshnyi S 2009 Gas heating in fast pulsed discharges in N_2O_2 mixtures *Eur. Phys. J. Appl. Phys.* **45** 21001

[27] Naidis G V 1999 Simulation of streamer to spark transition in short non-uniform air gaps *J. Phys. D: Appl. Phys.* **32** 2649

[28] Benilov N S and Naidis G V 2005 Modeling of discharges in a flow of preheated air *Plasma Sources Sci. Technol.* **14** 129

[29] Van Leer B 1979 Towards the ultimate conservative difference scheme: V. A second order sequel to Godunov's method *J. Comput. Phys.* **32** 101–36

[30] Einfeldt B 1988 On Godunov-type methods for gas-dynamics *SIAM J. Numer. Anal.* **25** 357–93